Solid Electrolytes for High-Temperature Stable Batteries and Supercapacitors

Vignesh Kumaravel,* John Bartlett, and Suresh C. Pillai*

Reports of recent fire accidents in the electronics and electric vehicles (EVs) industries show that thermal runaway (TR) reactions are a key consideration for the industry. Utilization of solid electrolytes (SEs) could be an important solution in to the TR issues connected to exothermic electrochemical reactions. Data on the thermal stability of modern SEs, ionic transport mechanisms, kinetics, thermal models, recent advances, challenges, and future prospects are presented in this review. Ceramic polymer nanocomposites are the most appropriate SEs for high-temperature stable batteries (in the range of 80–200 °C). Hydrogels and ionogels can be employed as stable, flexible, and mechanically durable SEs for antifreeze (up to –50 °C) and high-temperature (up to 200 °C) applications in supercapacitors. Besides the thermal safety features, SEs can also prolong the lifecycle of energy storage devices in next-generation EVs, space devices, aviation gadgets, defense tools, and mobile electronics.

1. Introduction

Thermal runaway (TR)-related explosions are the most common causes of fire accidents in batteries in the recent years.[1–3] TR normally occurs through uncontrolled or continuous exothermic reactions, and the increase of device temperature above 80 °C.[4] One well-publicized event of TR in electronic devices was the fire explosion issues of the Samsung Galaxy Note 7 in 2016. This resulted in severe economic losses for the Samsung company.[5,6] Batteries and supercapacitors are the most prominent electrochemical devices with distinct charge storage prop-

erties for various applications.[7–11] They are mostly fabricated using an anode, cathode, separator, and electrolyte. The schematic and mechanism of a battery (**Figure 1**a) and supercapacitor (Figure 1b) are displayed in Figure 1. Lithium (Li)-ion batteries are generally used in mobile phones, laptops, electric vehicles (EVs), etc.[12–14] Supercapacitors are employed in portable electronic devices, military tools, space devices, next-generation EVs, etc.[15–18] In any kind of electrochemical device, electrolyte is one of the most significant components to facilitate the ionic transport between the positive and negative electrodes.[19–22]

Liquid electrolytes (LEs) are preferred in traditional electrochemical devices to ease the ionic transport and wetting of the electrode surface.[23–25] Most LEs are made up of flammable organic solvents, such as ethylene carbonate (EC),[26] ethyl methyl carbonate (EMC),[27] and diethyl carbonate (DEC).[28] The failure of an electrochemical device under certain conditions could release flammable gases and this might trigger a fire hazard with the device at extreme temperatures.[29] Thermal decomposition of a battery or supercapacitor relies on its components, especially the electrolyte.[30,31] The characteristics of an electrolyte are more critical for high-temperature applications, compared to the electrodes or separators. The utilization of solid electrolytes (SEs) is an excellent choice to control the TR of an electrochemical device. SEs such as polymer electrolytes (PEs),[32,33] ceramic electrolyte (CE),[34,35] and ceramic–polymer electrolyte (CPE)[36,37] have been widely investigated in recent years. At high temperatures, the ionic conductivity and voltage safety window of SEs are superior when compared to LEs.[38] The important characteristics of the LE, PE, CE, and CPE are shown in **Figure 2**.[39] The flexibility, thermal stability, mechanical durability, electrochemical performance, ionic conductivity, interfacial contact, and Li dendrite suppression capability of CPE are superior, compared to LE, PE, and CE.

Generally, the CPE is composed of a polymer (e.g., polyvinylidene fluoride (PVDF),[40] polyvinyl chloride,[41] poly(ethylene oxide) (PEO)[42] poly(methyl methacrylate), etc.),[43] Li salt (e.g., lithium bis(trifluoromethanesulfonyl)imide (LiTFSI),[44] lithium bis(fluorosulfonyl)imide (LiFSI),[45] lithium perchlorate (LiClO$_4$),[46] etc.), and a ceramic filler (e.g., aluminum oxide (Al$_2$O$_3$),[47,48] silicon dioxide (SiO$_2$),[49] metal–organic frameworks (MOFs),[50] Li$_{6.75}$La$_3$Zr$_{1.75}$Nb$_{0.25}$O$_{12}$ (LLZNO),[51] Li$_7$La$_3$Zr$_2$O$_{12}$ (LLZTO),[52] etc.). The ceramic filler could be used in various dimensions such as 1D, 2D, and 3D (**Figure 3**).[39] The ionic conductivities of 2D and 3D materials are higher than that of 0D and 1D ceramic fillers.[39]

Dr. V. Kumaravel, Dr. J. Bartlett, Prof. S. C. Pillai
Nanotechnology and Bio-Engineering Research Group
Department of Environmental Science
School of Science
Institute of Technology Sligo
Ash Lane, Sligo F91 YW50, Ireland
E-mail: kumaravel.vignesh@itsligo.ie; pillai.suresh@itsligo.ie
Dr. V. Kumaravel, Dr. J. Bartlett, Prof. S. C. Pillai
Centre for Precision Engineering
Materials and Manufacturing Research (PEM)
Institute of Technology Sligo
Ash Lane, Sligo F91 YW50, Ireland

2002869 (1 of 42)

ADVANCED
SCIENCE NEWS
www.advancedsciencenews.com

ADVANCED
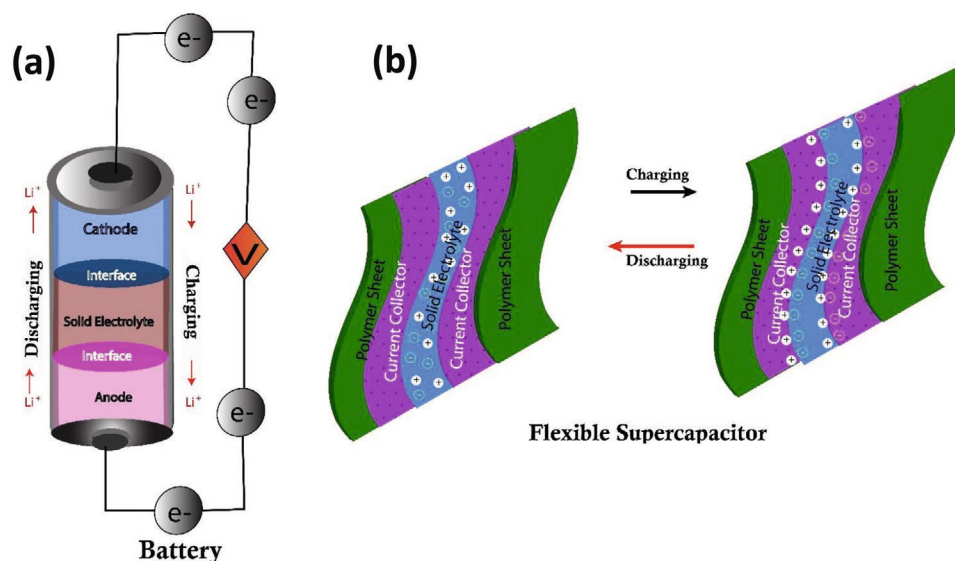ENERGY
MATERIALS
www.advenergymat.de

Figure 1. Schematic and mechanism of a) battery and b) supercapacitor.

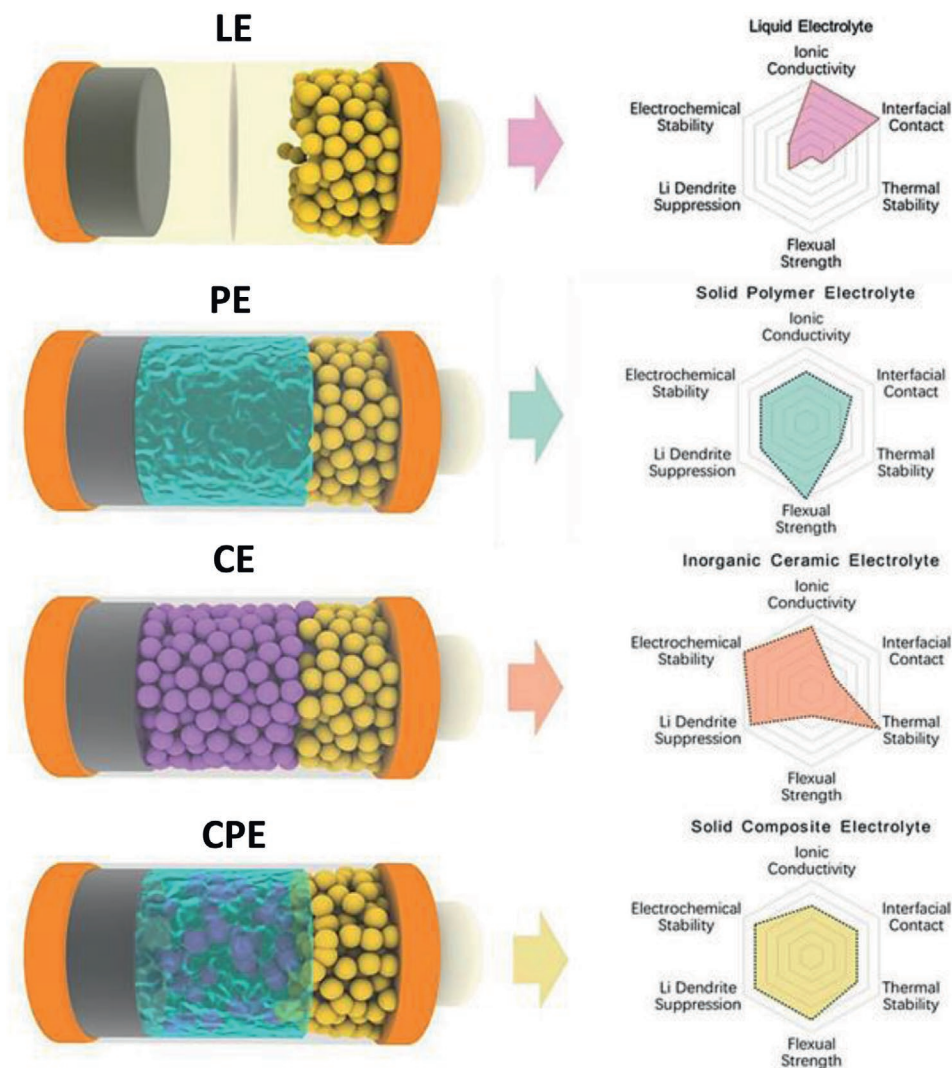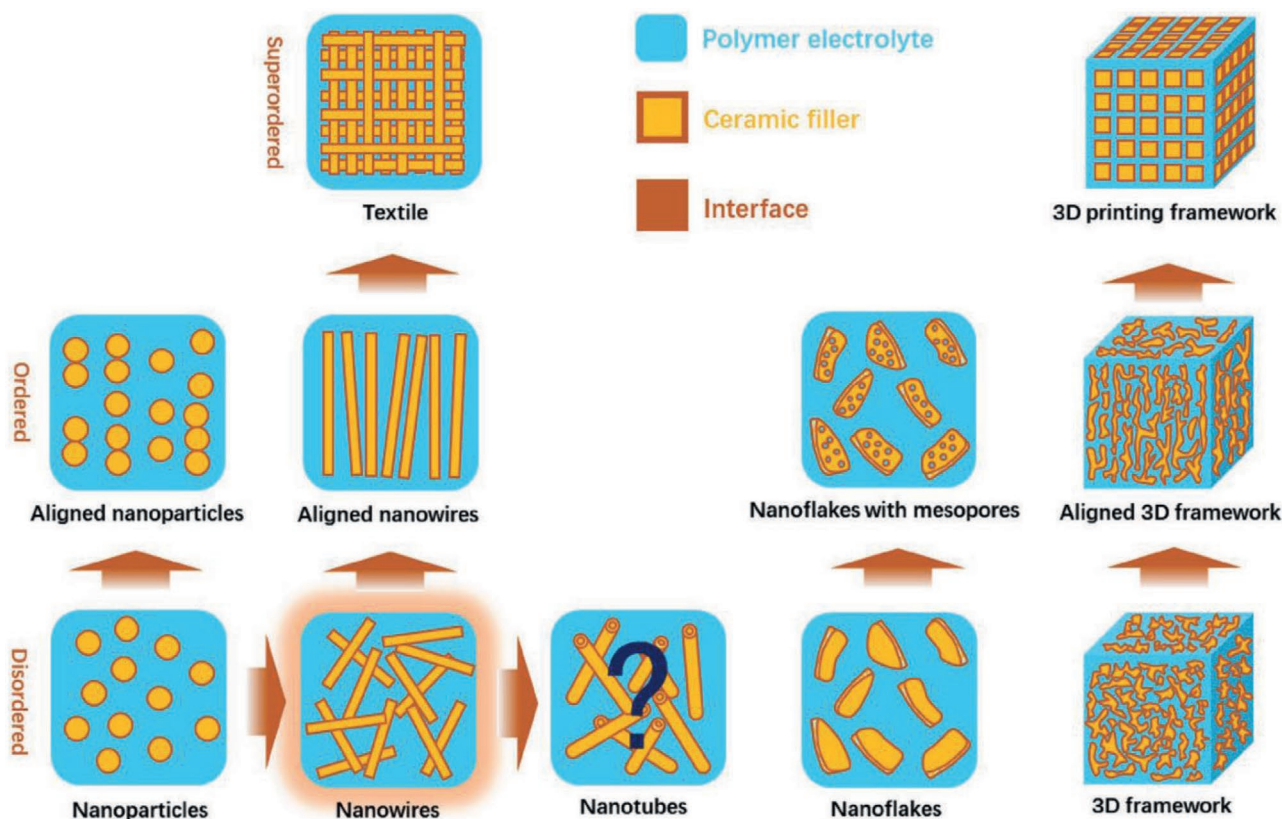**Figure 2.** The important characteristics of the LE, PE, CE, and CPE.[39] Reproduced with permission.[39] Copyright 2020, Wiley-VCH.

**ADVANCED
SCIENCE NEWS**

www.advancedsciencenews.com

**ADVANCED
ENERGY
MATERIALS**

www.advenergymat.de

Figure 3. The morphology of various ceramic fillers such as nanoparticles, nanowires, nanotubes, nanoflakes or nanosheets, and 3D materials in CPE.[39] Reproduced with permission.[39] Copyright 2020, Wiley-VCH.

SEs are much safer under short-circuit conditions compared to the flammable organic LEs.[23] The ionic conductivity and the electrochemical stability of SEs are superior to that of traditional LEs. SEs could also be used for high-performance metal anode and high-voltage cathodes. Moreover, SEs are mechanically durable and thermally stable with affordable cost.[53] The solid-state materials could act as an electrolyte as well as separator. The degradation of electrodes and the shuttling effect of polysulfides in Li–oxygen and Li–sulfur batteries could be rectified through SEs.[54] The lifetimes of electrochemical devices with SEs or solid-state cells are much longer, for example, a solid-state micro-battery could operate more than 10 000 cycles.[55] The ionic conductivity of SEs is generally not much decreased with respect to the temperature.[56] SEs could be utilized in the temperature range of –50 to 200 °C, while the traditional LEs would freeze or catch fire at extreme low and high temperature.[57] Consequently, the utilization of SEs in batteries and supercapacitors is an excellent choice for applications under harsh weather conditions.

TR prevention is of significant interest to several industries, such as automobile, electronics, military, aviation, oil drilling, and space research, to expand the safety features of electrochemical devices at extreme temperatures and weather (**Figure 4**).[2,31,58] In recent years, the significance of electrolytes was investigated and reviewed in various aspects such as electrode/electrolyte interfaces for sodium ion batteries;[59–62] interfaces and interphases of SEs in solid-state battery;[63] char-

acteristics of ionic liquid (IL)-incorporated polymer/inorganic hybrid electrolytes;[64] design/recent advances of SEs;[53,65–77] features of PEs (e.g., PEO, plastic crystals, polycarbonates, polyesters, polysiloxane, polyacrylates, etc.);[78–91] novel concepts of electrolytes;[23] ion transport mechanism of inorganic SEs;[38] fundamentals of inorganic SEs;[57] SEs for solid-state Li batteries;[54] explosion features of carbonate LEs;[29] perspectives of CPEs (e.g., lithium phosphorus oxynitride, sodium superionic conductors (NASICON)), Li-ion conductors, perovskites (LaTiO$_3$, SrTiO$_3$, Li$_3$La$_{2/3x}$TiO$_3$, etc.), sulfides (e.g., Li$_{10}$GeP$_2$S$_{12}$, Li$_3$P$_7$S$_{11}$, Li$_{3.25}$Ge$_{0.25}$P$_{0.75}$S$_4$, Na$_{2.88}$Sb$_{0.88}$W$_{0.12}$S$_4$, etc.), and garnet-type materials (e.g., Li$_{6.5}$La$_3$Zr$_{1.5}$Ta$_{0.5}$O$_{12}$, Li$_{6.4}$La$_3$Zr$_{1.4}$Ta$_{0.6}$O$_{12}$, Li$_7$La$_3$Zr$_2$O$_{12}$, etc.);[39,48] prospects of hydroborate electrolytes;[92] thermal/chemical expansion of CEs;[93] computational surveys of electrode/electrolyte interface;[94] electrolytes for organic material-based energy storage;[95] NASICON-type SEs;[96] electrolytes for Ca-based batteries;[97] configuration of electrolytes for fast charging Li batteries;[98] high-voltage electrolytes for aqueous energy storage;[99] modeling of ILEs;[100] electrolytes for magnesium–sulfur batteries[101]/magnesium batteries;[102] electrolytes for Li–sulfur batteries;[103] sulfide materials;[104,105] ionogels (immobilization of ILs in a solid matrix (e.g., ZrO$_2$, SiO$_2$, multi-walled carbon nanotubes (MWCNTs), MOFs, COFs);[106] nanohybrid electrolytes;[107] vanadium electrolytes;[108] low-temperature solid oxide;[109] hydrogels (e.g., polyacrylamides (PAMs), polyacrylic acid (PAA), polyvinyl alcohol (PVA), chitosan, carboxymethylcellulose, etc.);[110] salt-concentrated battery
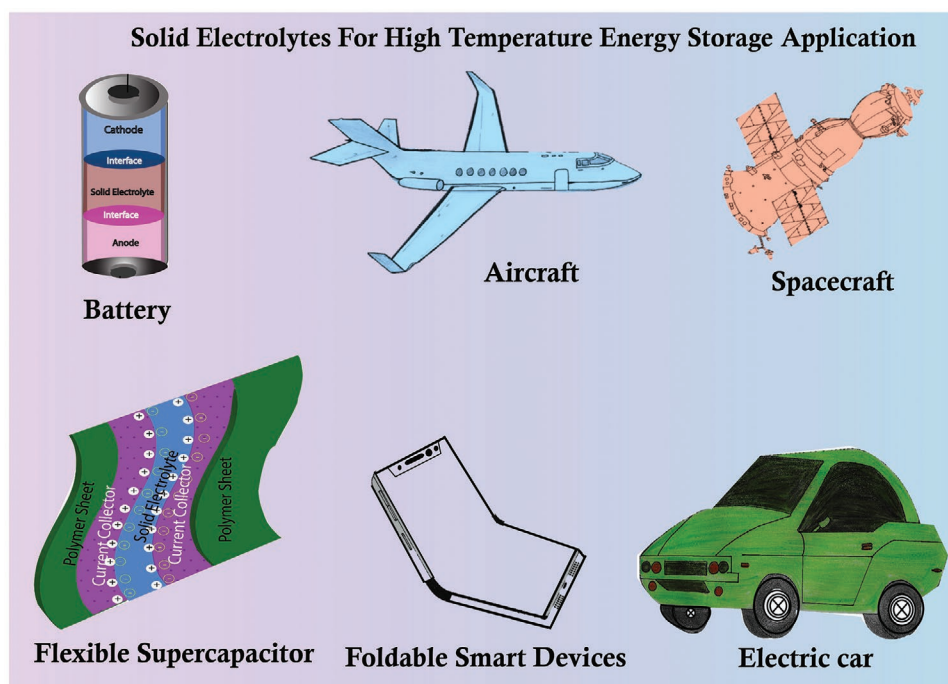
Figure 4. Applications of SEs for high-temperature stable energy storage devices (batteries and supercapacitors).

electrolytes;[111] and electrolytes for high-temperature ammonia production.[112] Most of the existing reviews for SEs are mainly focused on the type of solid materials, unique features, and their recent advances. There are no comprehensive reports on the high-temperature stability of SEs for batteries and supercapacitors. In particular, the materials and challenges for the high-temperature electric energy storage was reviewed by Lin et al.[113] The importance of IL, carbonate solvents, PEs, and CEs were discussed for the high-temperature applications. Very recently, Xidong et al. have reviewed the high-temperature applications of SEs and LEs for the rechargeable batteries. The computational studies on ion diffusion, electrochemical stability, continuum model, and artificial intelligence to engineer the electrolytes have also been discussed.[114] Nevertheless, there was no extensive discussion on the TR mechanism, thermal models, kinetics, and the insights of modern CPEs. Herein, the recent progresses in the engineering of key SEs such as CPEs, PEs, ionogels, and hydrogels for batteries and supercapacitors in the range of 80–200 °C are comprehensively reviewed. Most of the existing electronic devices could be destroyed by the ISC at sub-zero and elevated temperatures. Therefore, temperature tolerance is one of the most significant features for the safety of modern electronic devices. The high-temperature stability of SEs is crucial to mitigate the risk of fire explosions of electrochemical devices at extreme weathers. TR mechanism, ionic transport phenomena, kinetics, and thermal models of batteries and supercapacitors are also reviewed in detail.
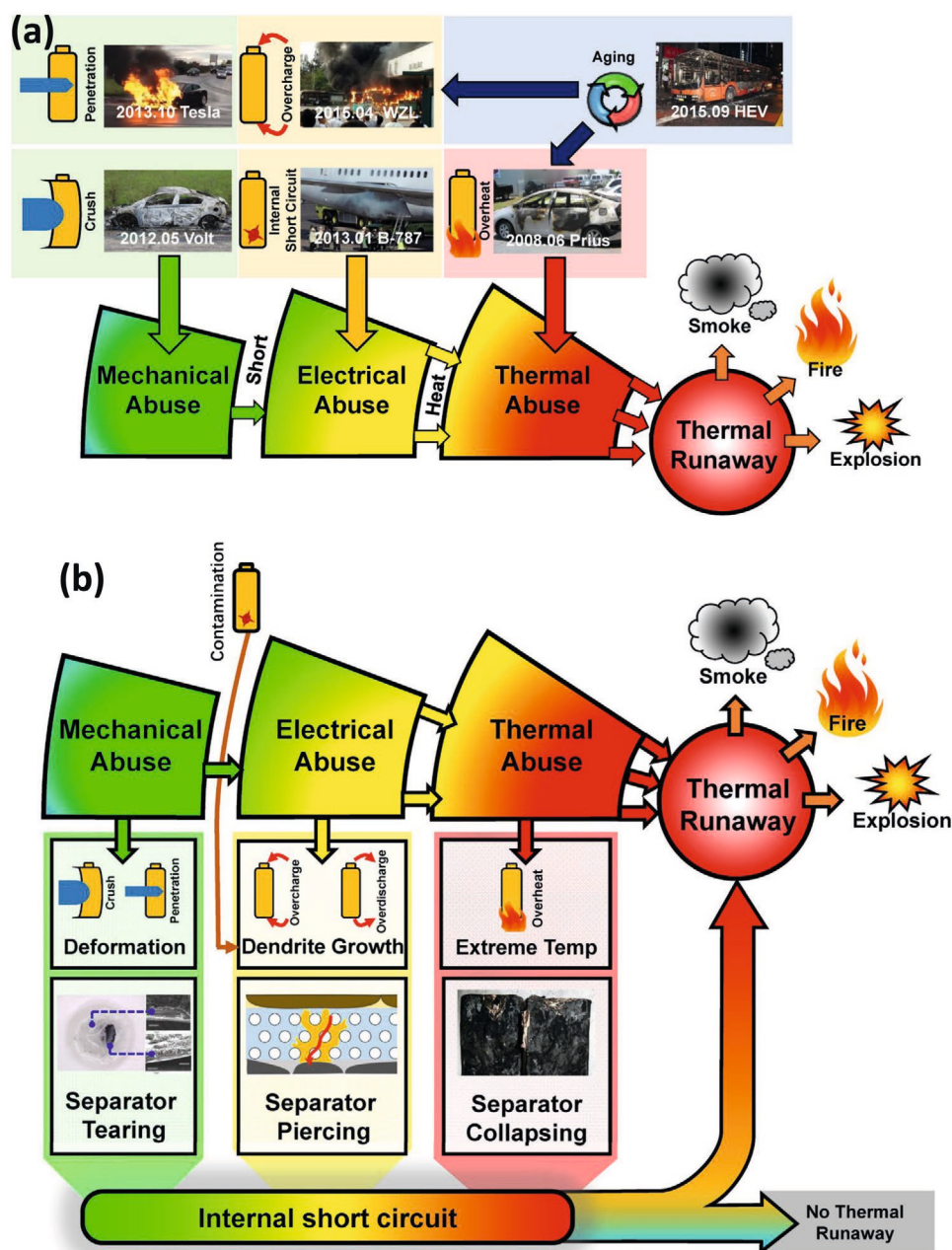
2. Mechanism of TR

The failure of a battery TR could be triggered through three predominant abuse conditions: mechanical (e.g., excessive pres-sure, collision, crush, and penetration of the battery), thermal (e.g., local overheat or operating the device above the safety temperature limit), and electrical (e.g., operating the device above the safety voltage limit, external short circuit, overcharge, or overdischarge).[1] The various conditions such as mechanical, electrical, and thermal abuse of Li-ion battery TR during the fire accidents of EVs for the past 10 years are displayed in **Figure 5**a. Mechanical and electrical abuse conditions could cause the cell connector to be loosened, causing subsequent local overheat. As compared to the mechanical and electrical abuse, thermal abuse is the direct source of a battery TR. All three abuse conditions of TR are commonly triggered via the internal short circuit (ISC). Figure 5b shows that the ISC is the common cause of TR and fire explosion.

ISC occurs through the separator damage during the mechanical (separator tearing via nail penetration or crush), electrical (separator piercing by dendrite growth at overcharge or overdischarge), and thermal abuse (separator shrinkage and collapse) conditions. As the separator is damaged, the two electrode materials are in contact with each other and cause ISC. The heat energy release rate relies on the degree of separator damage. In situ experiments in a recent study demonstrated that the chemical crossover between the electrodes was the foremost mechanism for TR.[115] During the TR process, oxygen released from the cathode was consumed by the lithiated anode, causing a fire and explosion in a Li-ion battery.

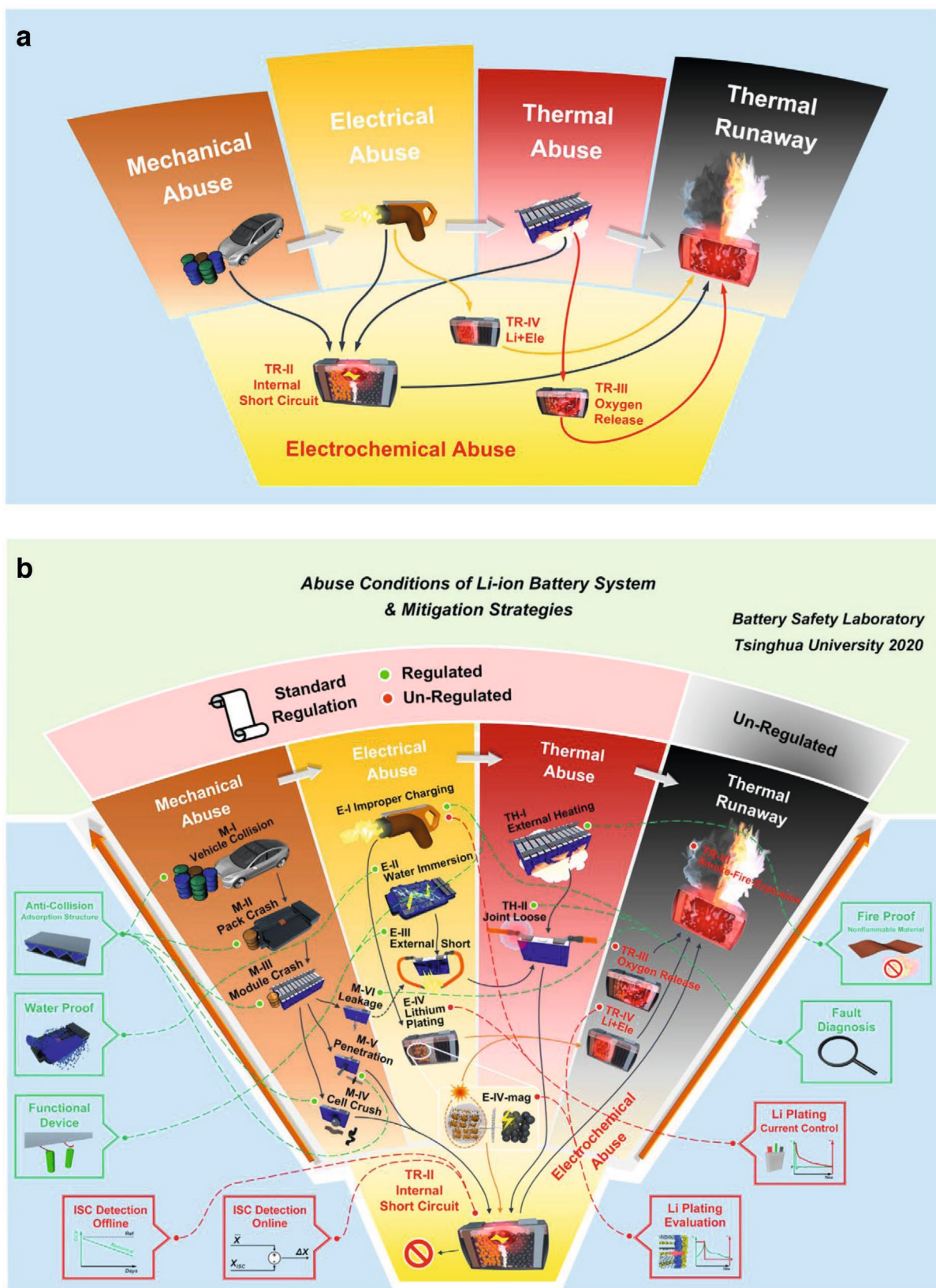A recent study reveals that another abuse condition should be considered where the batteries are working above their capability (e.g., extreme fast or slow charging, ultrahigh operation temperature).[2] This is known as electrochemical abuse (**Figure 6**a). It occurs when the electrochemical device is forced to function beyond its capacity in electrochemical power outputs. The possibilities of electrochemical abuse are highest

ADVANCED
SCIENCE NEWS

www.advancedsciencenews.com

ADVANCED
ENERGY
MATERIALS

www.advenergymat.de

Figure 5. a) Photographs of the fire accidents in EVs and schematic of different abuse conditions and b) schematic of correlation between ISC and abuse conditions.[1] Reproduced with permission.[1] Copyright 2008, Elsevier.

for batteries with new chemistry and narrow voltage window. An electrochemical abuse condition could be controlled through comprehensive knowledge on the safe working window of the battery components. The reactions and mitigation strategies of a battery TR during the abuse conditions at material, cell, pack, module, and vehicle levels are displayed in Figure 6b. The abuse conditions and states (e.g., system, material, cell, etc.) may move from one to another until the TR occurs. All the abuse conditions may finally transfer into thermal abuse to heat the battery at extremely high temperatures. As the state of transfer is higher, the TR could be easily

triggered by the mechanical and electrical abuse conditions. All the abuse conditions including the ISC could be able to trigger the TR. The mitigation plans corresponding to the specific abuse conditions are indicated as dotted lines in Figure 6b. The strategies such as anti-collision, waterproof, functional device, fault diagnosis, and fireproof have already been considered in the existing standard test regulations. ISC detection online/offline, Li plating evaluation, and Li plating current control have not been accounted in the standard test regulations. ISC detection is one of most challenging tests to diagnose the TR. The fire accident of Samsung Galaxy Note 7 demonstrated that

ADVANCED
SCIENCE NEWS

www.advancedsciencenews.com

ADVANCED
ENERGY
MATERIALS

www.advenergymat.de

Figure 6. a) Schematic of connection between the various abuse conditions for a battery TR and (b) the reactions and mitigation strategies of a battery TR during the abuse conditions at material, cell, pack, module, and vehicle levels (E, electrical abuse; M, mechanical abuse; TH, thermal abuse).[2] Reproduced with permission.[2] Copyright 2020, Elsevier.

the possibility of ISC was higher for the materials in a limited cell volume.[116] National Aeronautics and Space Administration (NASA) and the National Renewable Energy Laboratory (NREL) signified that ISC testing could be applied in the worst-case failure situations.[117,118] To ensure the overall safety of electrochemical devices with new chemistries, the standard test reports must include all kind of abuse conditions.

The most important temperatures for the battery TR are onset temperature of abnormal heat production (T1), triggering temperature of battery TR (T2), maximum temperature (T3), and the maximum heat release rate during TR ($\max(\mathrm{d}T/\mathrm{d}t)$) (**Figure 7**). T1 denotes the overall thermal stability of a device. T2 is the peak point that distinct the steady temperature rise from the sharp temperature rise. Xuning et al. suggested that the TR mitigation strategy of a battery was to raise the T1 and T2, and reduce the T3 and $\max(\mathrm{d}T/\mathrm{d}t)$.[2] Accelerating rate calorimetry (ARC) is an accurate technique to analyze the significant temperatures of TR as compared to other methods. ARC mainly focuses on the heat generation and it excludes the impact

of heat dissipation to the environment. The experimental procedures and common features of an ARC experiment are displayed in Figure 7.[2]

At first, the device was heated to the point of TR inside the ARC chamber. A standard method called "heat–wait–seek mode" was applied during the heating process. ARC signal was recorded by monitoring the fluctuations in temperature, voltage, and temperature rate of the device. Once a significant heat generation was detected from the device, the ARC system could track the temperature to provide an adiabatic test environment. The mitigation of a battery TR entirely relies on the comprehensive information of the development of T1, T2, and T3.

The time-dependent TR mechanisms of batteries could be analyzed through the time sequence map (TSM) approach.[119] The specific chemical and/or physical TR process occur inside and outside the battery could be classified by TSM approach. The mitigation strategies and TR states of Li-ion battery with LE are shown in **Figure 8**. In-path and out-path mechanisms showed the sequence of reactions occurs inside and outside the battery
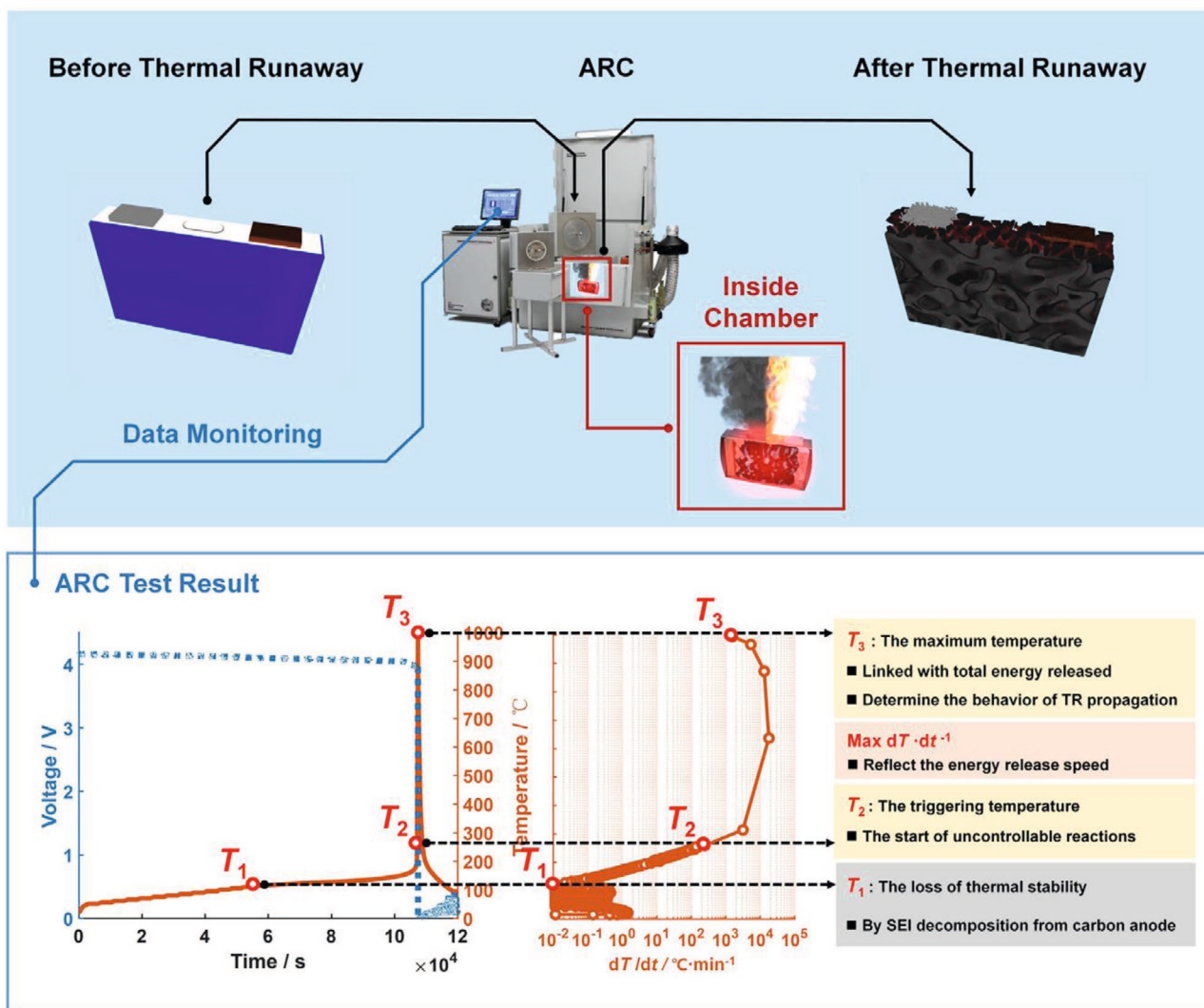
Figure 7. The experimental procedure and common features of an ARC experiment during the TR of battery.[2] Reproduced with permission.[2] Copyright 2020, Elsevier.

ADVANCED
SCIENCE NEWS
www.advancedsciencenews.com

ADVANCED
ENERGY
MATERIALS
www.advenergymat.de
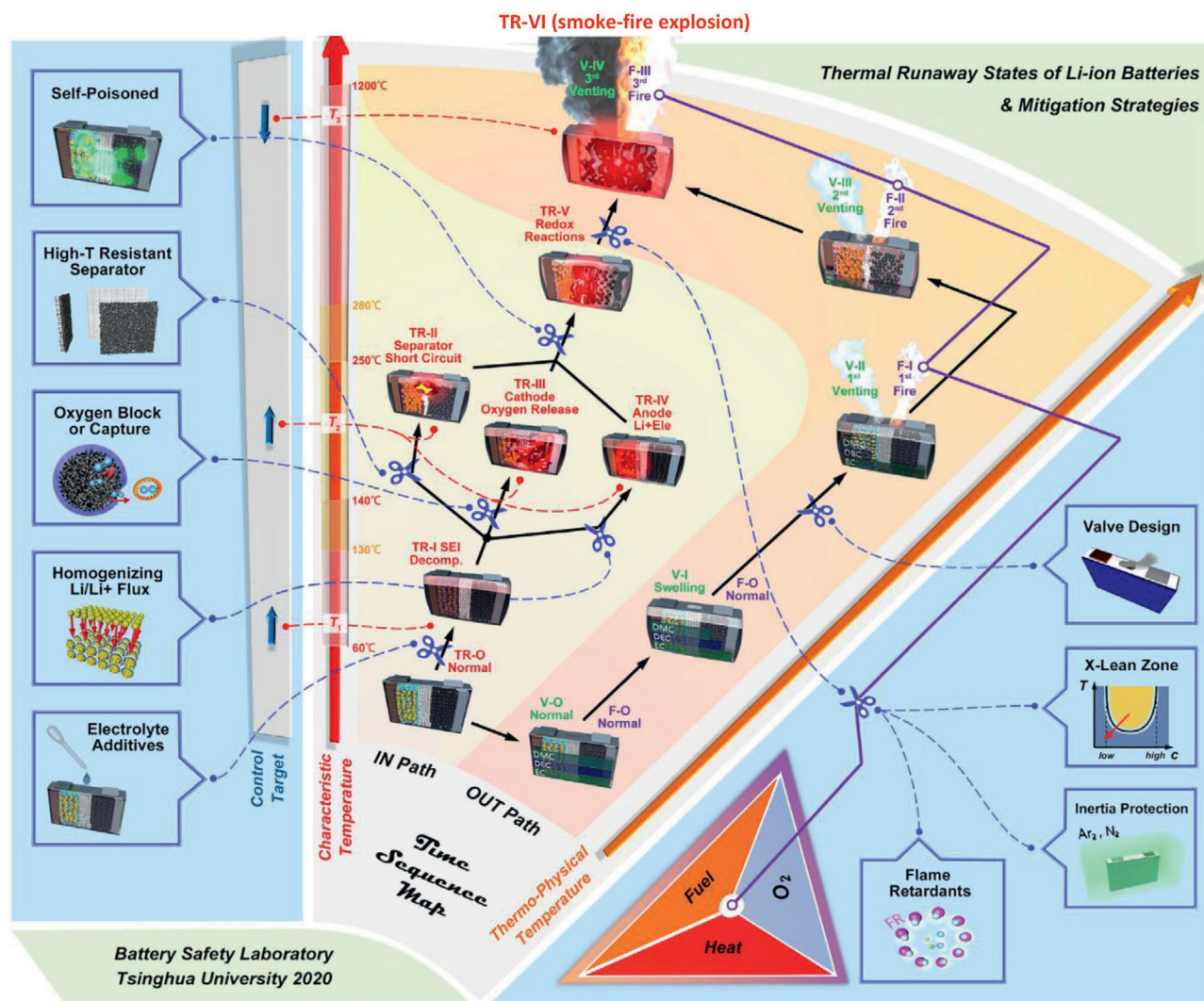
Figure 8. TSM approach: schematic for the classification of specific chemical and/or physical TR process at in-path/out-path. Mitigation strategies for the in-path: electrolyte additives, homogenizing Li/Li⁺ flux, O_2 block or capture, high-temperature-resistant separator, and self-poisoned (e.g., utilization of high-temperature stable or thermoresponsive materials, structural modifications of current collector, etc.). Mitigation strategies for the out-path: fire retardants or SEs, inertia protection, X-lean zone, and valve design.[2] Reproduced with permission.[2] Copyright 2020, Elsevier.

with respect to the temperature. The reactions at the electrodes and the ISC were described by the in-path. Besides, the formation mechanisms of T1, T2, and T3 were determined by the in-path. The vent, smoke, and fire or explosion outside the battery is elucidated by the out-path. T1 was formed at the starting point of solid-electrolyte interphase (SEI) decomposition. T1 was further increased into T2 during the decomposition of SEI in a Li-ion battery with graphite anode. The heat release states at the in-path were classified as TR-I (staring of SEI decomposition), TR-II (ISC from the disintegration of separator), TR-III (reactive O_2 release from the cathode), TR-IV (massive Li plating at the anode during fast charging), TR-V (redox reactions between the cathode and anode), and TR-VI (smoke–fire explosion). TR-V was the main state for the release of excess heat.

The vent states at the out-path were classified as V-0 (normal), V-I (swelling), V-II (first venting), V-III (second venting), and V-IV (third venting). The fire states were classified

as F-0 (normal), F-I (first fire), F-II (second fire), and F-III (third fire). The cell rupture was the most critical step for out-path. This was ascribed to the increase of internal pressure through the gasification of carbonated LEs (major source of gas before reaching the T2) and the side reactions (dominate the gas after reaching T2) at high temperatures. The high-speed vent could easily ignite the flammable gases. The important factors (high-speed vent, flammable gases, and reactive O_2 release) for the excess of heat generation are illustrated in the fire triangle (Figure 8). The boiling points of typical carbonate LEs are closer to the T2, and it could cause the leakage of flammable gases to trigger the TR. Therefore, the utilization of thermally stable SEs is one of the ideal choices for the in-path and out-path to avoid the TR. Moreover, the thermally stable SEs could establish a stable SEI and avoid the redox reactions between the electrodes.

Feng et al. proposed that there were three levels of ISC on the basis of heat generation: level I (slow voltage drop, no obvious
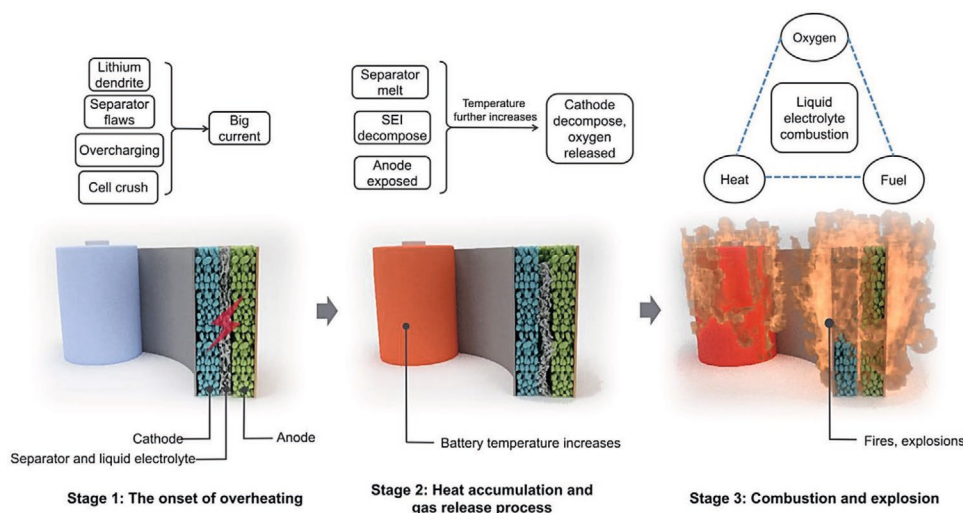
Figure 9. Schematic of three stages of TR in a battery.[4] Reproduced with permission.[4] Copyright 2018, American Association for the Department of Science.

heat), level II (fast voltage drop, obvious heat), and level III (no voltage, vigorous heat and non-stoppable).[1] The key reactions involved in the three stages of TR in a battery are schematically explained in **Figure 9**.[4] The important chain reactions for the TR mechanism are degradation of SEI, reaction between anode and electrolyte, decomposition of polymer/ceramic/electrolyte/cathode, ISC, and electrolyte firing.[120]

A recent study demonstrated that the temperature-tolerant LEs (LiFSI and lithium nitrate salts dissolved in a mixture of fluoroethylene carbonate and tetraethylene glycol dimethyl ether) could minimize the possibility of TR and Li dendrite formation in rechargeable batteries (Li|LiFePO$_4$).[121] The formation mechanism of SEI and Li plating/stripping characteristics was investigated using a Li metal anode at 90 °C. The results revealed that the capacity of Li metal anode was well retained (≈91.5%) in the temperature-tolerant LE during 100 cycles. The cyclic performance of Li metal anode in the temperature-tolerant LE was superior as compared to the conventional carbonate LEs (lithium hexafluorophosphate (LiPF$_6$) in EC/DC). It was also suggested that the operation of Li metal anode in LE at 90 °C leads to the development of a high-resistant SEI. Nevertheless, the applications of SEs would be the ideal options to completely avoid the TR issues in the electrochemical devices.

3. Ionic Conductivity Mechanism of Solid-State Electrolytes

The ionic conductivity mechanism of an electrolyte is governed by the chemical and electrochemical potential gradient of the system. According to the Nernst–Plank equation, the conductivity of a SE (σ) is described as follows[53]

$$\sigma = -\frac{j}{\nabla\varphi} = F^2 \sum_i \mu_i c_i \tag{1}$$

here, j, $\nabla\varphi$, F, μ_i, and c_i are the current density, electrical potential gradient, Faraday constant, mobility of charged species 'i',

and concentration of dissociated ion pairs, respectively. Therefore, an appropriate SE should enable the ion-pair dissociation to increase the ionic mobility and conductivity

$$\mu_i = \frac{D_i}{RT} \tag{2}$$

where, D_i, R, and T represent the diffusion coefficient, gas constant, and temperature, respectively. D_i can be demonstrated as a function of free energy of migration (ΔG_{mig})

$$D_i = \gamma a^2 f_o \exp\left(\frac{-\Delta G_{mig}}{RT}\right) \tag{3}$$

here, γ, a, and f_o are the constant of geometrical effect, hopping distance, and attempt frequency of ion hopping, respectively

$$\sigma_i = \frac{F^2}{RT} c_i \gamma a^2 f_o \exp\left(\frac{-\Delta G_{mig}}{RT}\right) \tag{4}$$

$$\sigma_i = \frac{F^2}{RT} c_i \gamma a^2 f_o \exp\left(\frac{\Delta S_{mig}}{R}\right) \exp\left(\frac{-\Delta H_{mig}}{RT}\right) \tag{5}$$

ΔS_{mig} and ΔH_{mig} are the entropy and enthalpy of migration. c_i could be correlated to the formation enthalpy (ΔH_f) as the ion-pair dissociation is activated by temperature

$$c_i = c_o \exp\left(\frac{-\Delta H_f}{RT}\right) \tag{6}$$

The overall activation energy for the formation and migration of mobile ions (E_a)

$$E_a = \Delta H_f + \Delta H_{mig} \tag{7}$$

Consequently, the ionic conductivity equation could be further simplified using the Arrhenius concept

$$\sigma_i = \frac{\sigma_o}{T} \exp\left(\frac{-E_a}{RT}\right) \tag{8}$$

As the temperature is below the glass transition temperature (T_g) of electrolyte material, the ion transport mechanism follows

the Arrhenius equation. At temperatures above the T_g, the ion transport follows the Vogel–Fulcher–Tammann (VFT) equation. At high temperatures, the ionic mobility is related to the structural motion and viscosity of the electrolyte material. Owing to the strong coupling of structural units, the ionic mobility of PE usually proceeds through the VFT equation

$$\sigma_i = \frac{\sigma_o}{T} \exp\left(-\frac{E_a}{R(T-T_o)}\right) \tag{9}$$

here, T_o indicates the temperature that is below the T_g.

The ion transport mechanism of the electrolytes is significantly influenced by the structural and physiochemical properties. In CPEs, the intrinsic interfaces (e.g., grains, vacancies, and junction) are highly accountable for the ionic conductivity compared to extrinsic interfaces (e.g., solid–solid contact).[56] There are two crucial phenomena involved in the ionic conductivity such within the bulk and across the interfaces.

3.1. Ionic Conductivity Mechanism within the Bulk

In the case of CEs, the lattice defects such as vacancies and interstices could facilitate the rapid ionic transport mechanism. The topology, coordination of crystal framework, and ion binding sites are the dominant factors of ionic transport phenomenon in crystalline superionic materials. The ionic transport mechanism in PEs usually proceeds through the amorphous and crystalline phases. The segmental motion of polymer chains in high molecular weight amorphous materials is governed via the intersegmental hopping. The ionic conductivity ensues through the diffusion in the solvated form for the amorphous polymers with low molecular weight. The early studies on ionic conductivity of polymers suggested that the ionic conductivity of crystalline domains was higher than that of amorphous phase.[122] Nevertheless, later theoretical and experimental investigations revealed that the ionic conductivity of PE could be improved by the reduction of its crystallinity.[123,124] Block copolymers and nanofillers have been shown to increase the ionic conductivity and mechanical stability of PEs.[125,126] However, the ionic conductivity of such PEs is affected at high temperatures, and this could be rectified through the cross-linking of polymer chains at their functional groups.[53] Cross-linking technique could prevent the interchain crystallization of polymer chains, suppress the Li dendrite growth, and facilitate the electrochemical properties of PE without influencing the other unique features of polymer.[53,127,128]
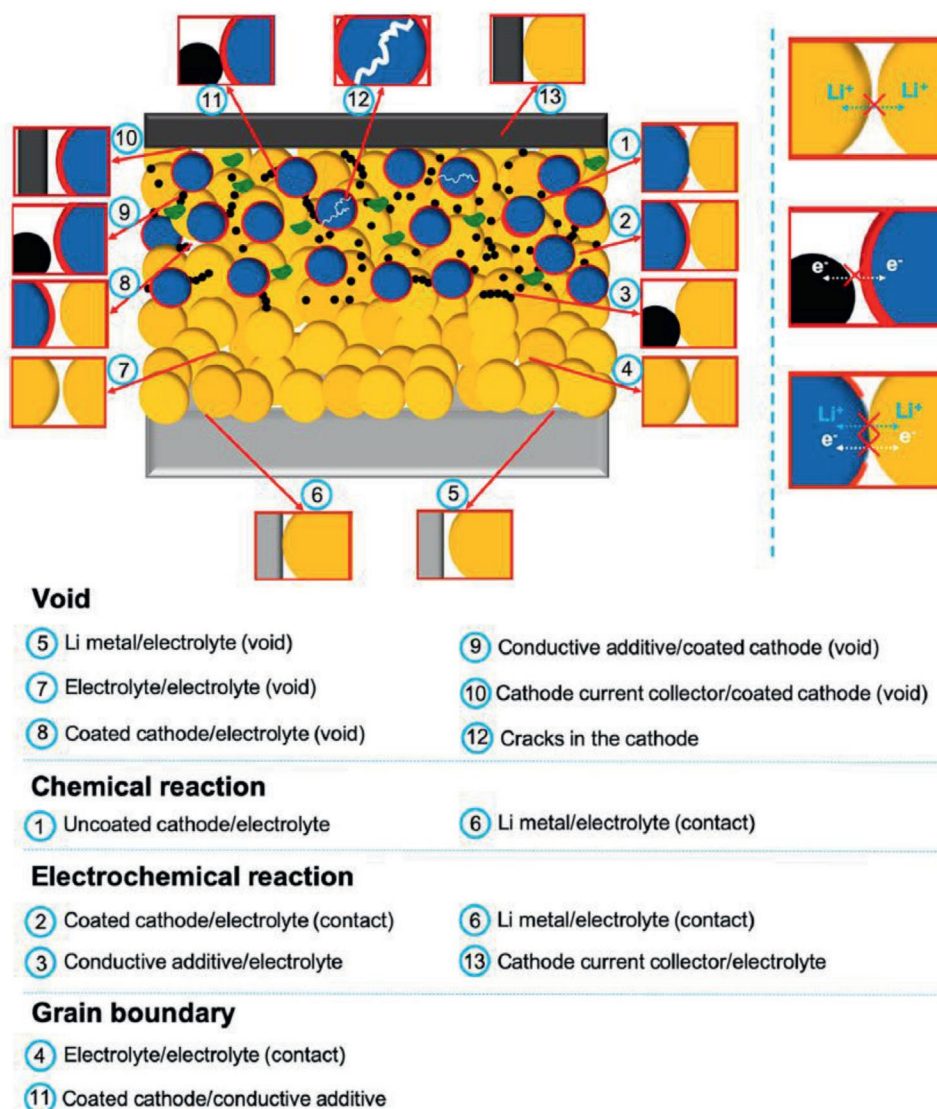
3.2. Ionic Conductivity Mechanism across the Interfaces

Various homogeneous and heterogeneous interfaces exist between the electrode and electrolyte. In a recent study, it was proposed that there were 13 interfacial phenomena that existed in the solid-state batteries with SEs with respect to the voids, grain boundaries, and chemical/electrochemical reactions (**Figure 10**).[63] These interfaces could directly or indirectly influence the ionic conductivity of SEs. As compared to other features, the grain boundaries could considerably suppress the ionic conductivity of SEs through the formation of Li deficient space-charge layer at the interface.[63]

Grain boundaries are the homogeneous interfaces that enable the ionic conductivity in most of the SEs.[129] Molecular dynamics[130] and impendence spectroscopy[131] studies demonstrated that the ionic conductivity of SEs was influenced by the grain boundaries. The activation energy of ionic mobility at the grain boundaries was higher than that in the bulk for antiperovskite crystals.[130] A space charge layer is formed at the heterogeneous interface due to the migration or depletion of ions at one side and the accumulation of mobile carriers at another side of the interface.[132,133] The ionic mobility and overall conductivity are influenced by the space-charge layers. The electrolyte establishes a smooth interface with anode (favorable for ion transport), and it creates a rough interface with porous cathode (difficult for ion transport). The inclusion of a buffer layer between the cathode and electrolyte could suppress the development of space charge layer, and facilitate the ion migration through additional routes.[134]

The interfaces such as anode–CPE, cathode–CPE, and ceramic–polymer should be considered to improve the performance of an electrochemical device with CPEs.[39] The poor interface between the anode and CPE is usually responsible for the Li dendrite growth in batteries. This could be rectified through the usage of thin and mechanically durable electrolyte materials.[39] A stable solid–solid interface between cathode and CPE for high-voltage applications could be engineered by widening the electrochemical window of CPE. In most of the cases, the electrochemical window of PE was below 5 V, while that of CE was ≥9 V versus Li/Li+.[135,136] Consequently, the loading of high ceramic content in CPE could extend the electrochemical window and enhance the electrochemical stability. This was attributed to the following reasons: dipole–dipole interaction of polymer–ceramic,[137] acidic surface sites of the electrolyte,[138] and removal of impurities from the interface.[139] Besides, the long-term stability of the battery could be improved via the establishment of stable ion conducting network inside the cathode material.[140] Layer-by-layer assembly and integrated designs could optimize the interfacial contact between the cathode and CPE to improve the ionic conductivity. The interfacial contact between the electrodes (both anode and cathode) and CPE could be progressed through the design of multilayer CPEs, using of 3D scaffolds, and the addition of small amount of LE or IL to wet the surface.[39,53,65] The uniform dispersion of ceramic particles in CPE could optimize the interface between polymers and ceramics, this could also facilitate the creation of rapid Li-ion conducting channels.[141] The interface between the polymers and ceramics is also influenced by the shape, size, dimension, and organization of ceramic particles in CPE.

Ion dynamics of CEs could be studied through the time-domain nuclear magnetic resonance (NMR) and AC conductivity spectroscopy.[142] The schematic of a solid-state battery with CE is displayed in **Figure 11**a. The influence of ionic transport by grain boundaries and the changes in activation energy (E_A) with respect to temperature (T) are displayed in Figure 11b. NMR accounts a crucial role on the changes of Li spin interactions with external and internal magnetic fields. The bulk ion dynamics could be probed through the sensing of dipolar–magnetic or quadrupolar–electric interactions as a function of temperature. The long-range and short-range ionic transport mechanisms are studied through the NMR relaxometry. This

Void
- (5) Li metal/electrolyte (void)
- (7) Electrolyte/electrolyte (void)
- (8) Coated cathode/electrolyte (void)
- (9) Conductive additive/coated cathode (void)
- (10) Cathode current collector/coated cathode (void)
- (12) Cracks in the cathode

Chemical reaction
- (1) Uncoated cathode/electrolyte
- (6) Li metal/electrolyte (contact)

Electrochemical reaction
- (2) Coated cathode/electrolyte (contact)
- (3) Conductive additive/electrolyte
- (6) Li metal/electrolyte (contact)
- (13) Cathode current collector/electrolyte

Grain boundary
- (4) Electrolyte/electrolyte (contact)
- (11) Coated cathode/conductive additive

Figure 10. Schematic of 13 interfacial phenomena in solid-state batteries with SEs.[63] Reproduced with permission.[63] Copyright 2020, American Chemical Society.
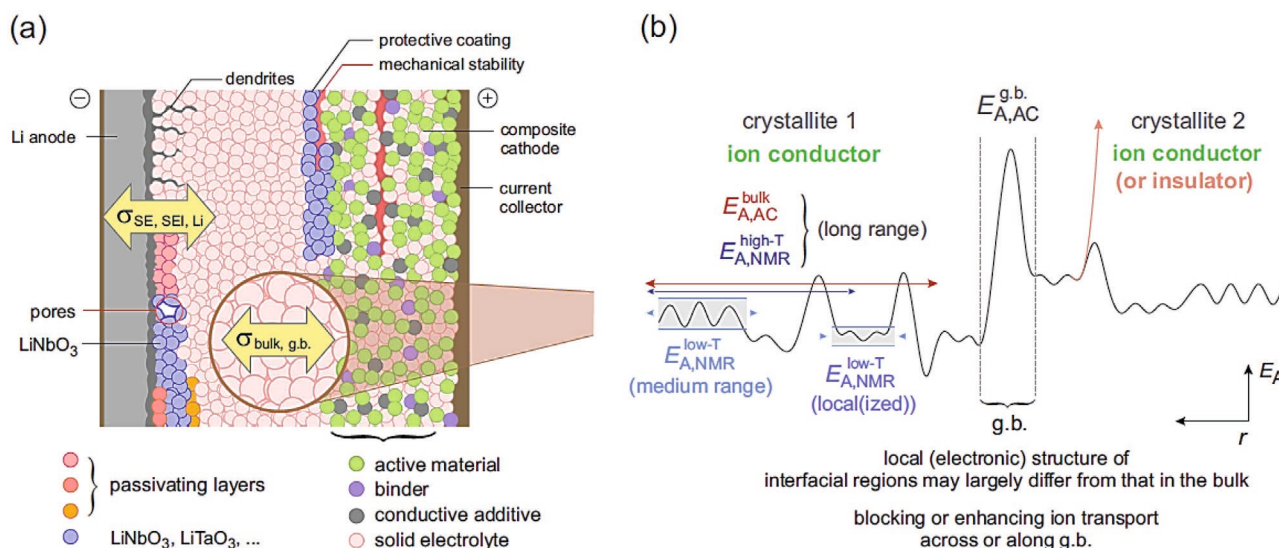
relies on the temperature and the effective resonance frequency of magnetization. The charge transfer across the macroscopic interfaces on different length scales and the formation of SEI are investigated via AC conductivity spectroscopy. The activation energies ($E_{A, Nmr}$ and $E_{A,AC}$) are distinct with respect to the time-scale and length-scale. The electronic structure of interfacial region of CE could block or enhance the ionic transport across the grain boundaries.

4. Kinetics

4.1. Batteries

Kinetic studies are very limited for the TR of an electrochemical device with SEs. An accurate thermal model is essential for the industrial applications of batteries and supercapacitors to

ensure the safety at high temperatures. TR of electrochemical devices with LEs was studied through various kinetic models with the help of Arrhenius equation. Differential scanning calorimetry (DSC) and ARC results were applied to elucidate the TR mechanism.[120,143,144] Significant features such as heat release condition,[145,146] ISC,[147,148] vent[149]/over charge[150]/TR propagation behavior,[151,152] and nail penetration[153] were investigated in detail by the TR kinetic models. Most of the models were explored with respect to the number of exothermic reactions considered in the battery. In a recent study, a TR model was proposed by considering the chemical kinetics of six dominant exothermic reactions in a fully charged battery.[154] The kinetic parameters of the exothermic reactions were established by the DSC results at different heating rates (5, 10, 15, and 20 °C min^{-1}) using the Kissinger's and nonlinear fitting technique. The kinetic model fitted well with the adiabatic TR and oven test (at 130 and 150 °C with a heating rate of 4 °C min^{-1})

**ADVANCED
SCIENCE NEWS**
www.advancedsciencenews.com

**ADVANCED
ENERGY
MATERIALS**
www.advenergymat.de

Figure 11. Ion dynamics: a) schematic of solid-state battery with a CE, b) influence of ionic transport by grain boundaries (g.b.), and the changes in activation energy (E_A) with respect to temperature (T).[142] Reproduced with permission.[142] Copyright 2017, Springer Nature.

experiments of a 24 Ah Li-ion battery. $Li(Ni_{1/3}Co_{1/3}Mn_{1/3})O_2$ and graphite were used as the cathode and anode, respectively. 1 M $LiPF_6$ in 1:1:1 ratio of dimethyl carbonate (DMC)/EMC/EC solvent mixture was used as electrolyte. DSC studies were carried out from room temperature to 600 °C under nitrogen atmosphere for two dominant exothermic reaction pairs such as anode+electrolyte (An+Ele) and cathode+anode (Cat+An). Adiabatic TR was tested by the extended volume-ARC (EV-ARC) under the heat–wait–seek mode (start at 40 °C, wait time 30 min, and seek time 20 min).[154] The reactions such as disintegration of SEI (Q_{SEI}), degradation of cathode material (Q_{Cat}), and the reaction of anode material and electrolyte (Q_{An-E}) or binder (Q_{An-B}) could occur at high temperatures.[154]

The rate of a chemical reaction (κ_x) was expressed as follows

$$\kappa_x = A_x \exp\left(-\frac{E_{a,x}}{RT}\right) f_x(c_x) \tag{10}$$

$$c_x = 1 - \int \kappa_x \, dt \tag{11}$$

here, c_x is the normalized concentration of reactant "x", A_x is the pre-exponential factor, $f_x(c_x)$ is the mechanism function, and $E_{a,x}$ is the activation energy. $f_x(c_x)$ could be expressed in terms of reaction order (n_x)

$$f_x(c_x) = c_x^{n_x} \tag{12}$$

The heat generation of the reaction (Q_x) could be elucidated from the mass of the reactant (m_x), κ_x, and enthalpy (ΔH_x)

$$Q_x = m_x \, \Delta H_x \, \kappa_x \tag{13}$$

Kissinger's equation was used to measure the activation energy and pre-exponential factor from the DSC results

$$\ln\left(\frac{\beta_i}{T_{p,i}^2}\right) = \ln\left(\frac{A_x R}{E_{a,x}}\right) - \frac{E_{a,x}}{R T_{p,i}}, \quad (i = 1, 2, 3, \ldots u) \tag{14}$$

here, β_i, $T_{p,i}$, and u are the heating rate, peak temperature, and the number of variant heating rates. A plot of $\ln\left(\frac{\beta}{T_p^2}\right)$ versus $\left(\frac{1}{T_p}\right)$

would give a straight line. Therefore, the activation energy and the pre-exponential factor could be determined from the slope and intercept, respectively. The other kinetic parameters were calculated through the nonlinear fitting method

$$Q_{sum} = Q_{SEI} + Q_{An-E} + Q_{An-B} \tag{15}$$

The root mean squared error (RMSE) between the kinetic model and experimental data could be calculated as follows

$$RMSE = \sqrt{\frac{\sum_{i=1}^{4} \sum_{j=1}^{l_i} \left(Q_{sum}(T_{i,j}) - Q_{exp}(T_{i,j})\right)^2}{\sum_{i=1}^{4} l_i}} \tag{16}$$

where, l_i and $T_{i,j}$ represent the total temperature points and the recorded temperature point, respectively. The calculated kinetic parameters for the reactions An+Ele and Cat+An agreed well with the model predictions. The battery temperature was determined from the energy balance equation[154]

$$\frac{dT_{Bat}}{dt} = \frac{Q_{gen} + Q_{diss}}{MC_p} \tag{17}$$

$$T_{Bat}(t) = T_{Bat,0} + \int \frac{dT_{Bat}}{dt} \, dt \tag{18}$$

here, $T_{Bat,0}$, Q_{gen}, Q_{diss}, M, and C_p are the initial battery temperature, rate of total heat generation, rate of total heat dissipation, mass of the battery, and specific heat capacity, respectively

$$Q_{gen} = Q_{SEI} + Q_{An-E} + Q_{An-B} + Q_{Cat-An} + Q_{Cat-B} + Q_{Cat} \tag{19}$$

$$Q_{diss} = hA(T_{ARC} - T_{Bat}) \tag{20}$$

where, h, A, and T_{ARC} denote heat exchange coefficient, area of the battery, and temperature of EV-ARC, respectively. As shown in **Figure 12**, an EV-ARC model was established for simulating the variation of T_{ARC} under different conditions such as heat, wait, seek, exothermic, and cool. EV-ARC model could be used

to investigate the safety features, exothermic reactions, and TR mechanism of battery components. The experimental values of onset TR temperature (T_{TR}), and the maximum temperature of TR process (T_{max}) for the adiabatic and oven tests agreed well with the kinetic model. Nevertheless, some minor deviations were also noticed between the model prediction and test results. A decrease in the battery temperature was observed around 115 °C and this was mainly attributed to the vaporization of electrolyte solvent.[149] After the TR process, the battery temperature rate was intensely amplified to ≥2000 °C min^{-1}, which was higher than the model prediction rates. This was ascribed to the ISC and other vigorous reactions inside the battery in a short time.

In another study, the effect of temperature on the SEI layer growth of a Li-ion battery was examined using a 1D thermal–electrochemical model.[155] SEI layer growth on the anode was focused in this study. Lithiated graphite and EC were used as the anode and electrolyte, respectively. The important equations of the 1D cell model are given as follows

$$a_s i_{loc} = \frac{\partial i_2}{\partial x} - a_s C \frac{\partial(\phi_1 - \phi_2 - U - R_{SEI} i_{loc})}{\partial t} \tag{21}$$

$$i_2 = -\sigma_2^{eff} \frac{\partial \phi_2}{\partial x} + \frac{2RT\sigma_2^{eff}}{F}\left(1 + \frac{d \ln f_\pm}{d \ln c_2}\right)\left(1 - t_+^0\right)\frac{\partial \ln c_2}{\partial x} \tag{22}$$

$$a_s i_{loc} = \frac{\partial}{\partial x}\left(\sigma_1^{eff} \frac{\partial \phi_1}{\partial x}\right) \tag{23}$$

$$i_1 = -\sigma_1^{eff} \frac{\partial \phi_1}{\partial x} \tag{24}$$

$$R_{SEI}(t) = \frac{\delta(t)}{\sigma_{SEI}} \tag{25}$$

$$\sigma_1^{eff} = \sigma_1 (\varepsilon_1)^p \tag{26}$$

$$\sigma_2^{eff} = \sigma_2 (\varepsilon_2)^p \tag{27}$$

here, i_{loc}, i_1, and i_2 represent the current densities of local, solid phase, and electrolyte phase, respectively. The terms a_s, C, U, R, T, t, σ, δ, ε, p, F, and $f_\pm$ denote active surface area of electrode, double-layer capacitance, open circuit potential, resistance, temperature, time, ionic conductivity, thickness of SEI layer, volume fraction, Bruggeman porosity exponent, Faraday's constant, and activity coefficient of the salt in the electrolyte, respectively. ϕ_1 and ϕ_2 are the electric potentials of the solid and electrolyte phases, respectively. c_2 and t_+^0 are the concentration and transference number of Li ions in the electrolyte, respectively. The thermal energy conversion could be represented as follows

$$\frac{\partial(\rho C_p T)}{\partial t} = \nabla \lambda \nabla T + q \tag{28}$$

$$-\lambda \nabla T = h(T - T_0) \tag{29}$$

Heat generation rate per unit volume (q)

$$q = a_s i_{loc}\left(\phi_1 - \phi_2 - U - R_{SEI} i_{loc} + T\frac{\partial U}{\partial T}\right) + \sigma_1^{eff}(\nabla\phi_1)^2 + \sigma_2^{eff}(\nabla\phi_2) + \sigma_{2D}^{eff}\nabla \ln c_2 \nabla\phi_2 \tag{30}$$

here C_p, λ, and ρ illustrate the heat capacity, thermal conductivity, and mass density of the electrochemical device, respectively. h and T_0 signify the heat transfer coefficient and room temperature, respectively.

Effective solution-phase diffusional conductivity σ_{2D}^{eff}

$$\sigma_{2D}^{eff} = \frac{2RT\sigma_2^{eff}}{F}\left(1 - t_+^0\right)\left(1 + \frac{d \ln f_\pm}{d \ln c_2}\right) \tag{31}$$

Arrhenius equation was used to describe all temperature-responsive physicochemical properties (Φ) such as conductivity of electrolyte, diffusion coefficient of a species, and exchange current density of an electrode reaction

$$\Phi = \Phi_{ref} \exp\left[\frac{E_{act,\Phi}}{R}\left(\frac{1}{T_{ref}} - \frac{1}{T}\right)\right] \tag{32}$$

A multiscale and multiphysics model was established using the COMSOL Multiphysics software 4.2a. The integration of various kinetic models is schematically shown in **Figure 13**. 1D porous electrode model comprised an anode, separator, and cathode regions. SEI growth was accomplished in the pseudo-2D model and then the resistance of the layer was estimated in the 1D model.

The results showed that the difference in SEI growth rate during charging and discharging was attributed to the variation of temperature. SEI growth was faster during charging because the temperature of charging was slightly higher than discharging. Internal resistance increase, capacity loss, and ohmic loss were observed at high temperatures. This was ascribed to the increase of SEI layer thickness with respect to temperature. The cell average temperature at different boundary conditions was not remarkably affected by the increase of heat transfer coefficient. Nevertheless, the cell average temperature was considerably increased during the cooling process.

In another recent study, an energy release diagram of TR was proposed by linking the chemical kinetics of around 50 recent investigations (**Figure 14**). The total energy release of significant chemical reactions was plotted against temperature. The heat energy released (ΔH) by the ISC and combustion of electrochemical devices were also illustrated in the diagram. ISC occurred in the range of 130–170 for polymers, and ≥200 ceramics. ΔH was determined for the cells with 100% state of charge.

The degradation of SEI was modeled by the Arrhenius equation.[1] SEI degradation (SEI^d) occurred in the range of 80–120 °C, and the SEI regeneration (SEI^g) occurred in the range of 120–250 °C

$$\frac{dc_{SEI}^d}{dt} = A_{SEI} c_{SEI} \exp\left(-\frac{E_{a,SEI}}{RT}\right), (T > T_{onset,SEI}) \tag{33}$$

The net decreasing rate of SEI

$$\frac{dc_{SEI}}{dt} = \frac{dc_{SEI}^d}{dt} - \frac{dc_{SEI}^g}{dt} \tag{34}$$

The rate of SEI^g was assessed from the rate of reaction between the intercalated Li anode and electrolyte

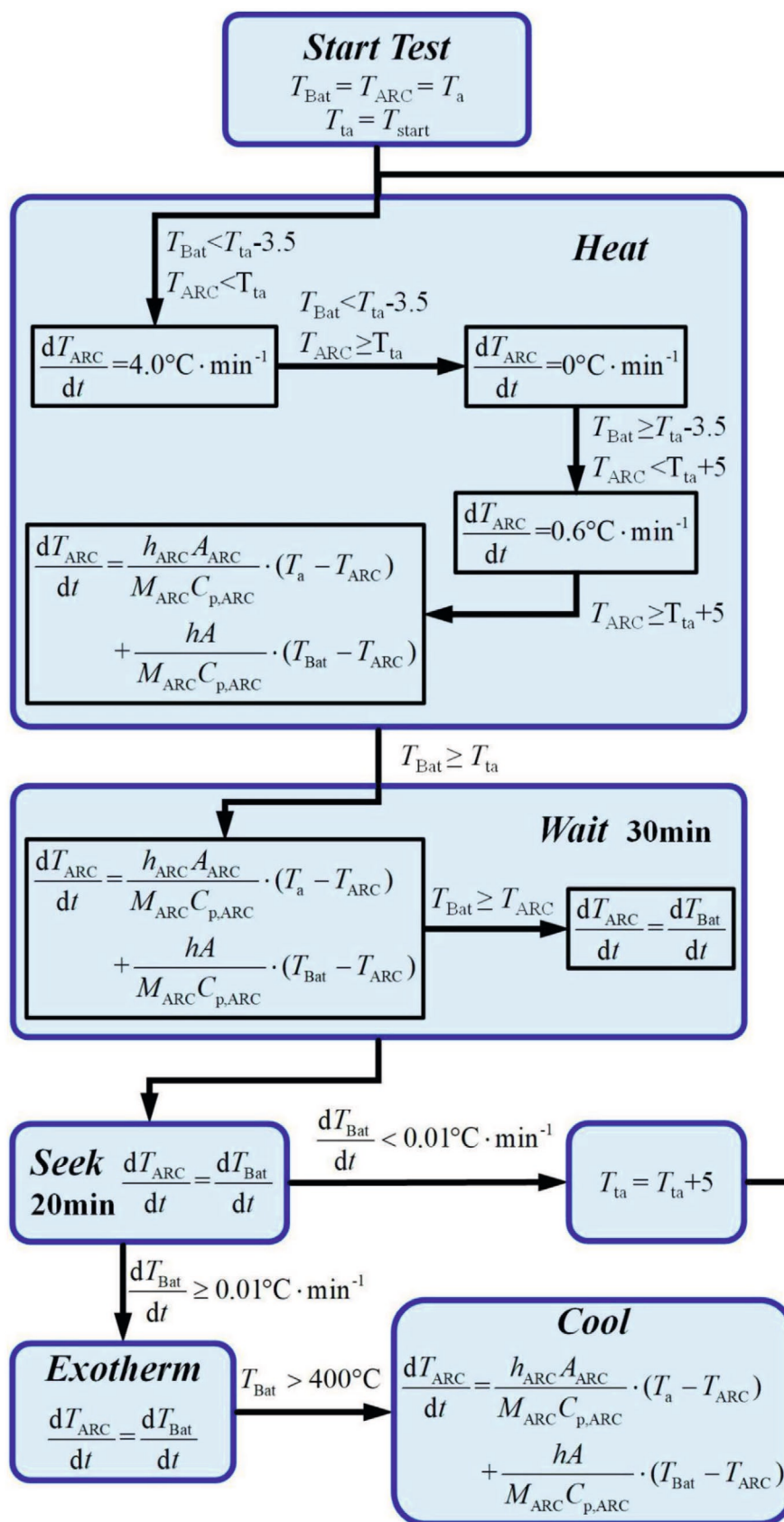$$\frac{dc_{SEI}^g}{dt} = K_{SEI}^g \frac{dc_{Li+Ele}}{dt} \tag{35}$$

**ADVANCED
SCIENCE NEWS**

www.advancedsciencenews.com

**ADVANCED
ENERGY
MATERIALS**

www.advenergymat.de

Start Test
$$T_{Bat} = T_{ARC} = T_a$$
$$T_{ta} = T_{start}$$

Heat

$$T_{Bat} < T_{ta} - 3.5$$
$$T_{ARC} < T_{ta}$$

$$\frac{dT_{ARC}}{dt} = 4.0°C \cdot min^{-1}$$

$$T_{Bat} < T_{ta} - 3.5$$
$$T_{ARC} \geq T_{ta}$$

$$\frac{dT_{ARC}}{dt} = 0°C \cdot min^{-1}$$

$$T_{Bat} \geq T_{ta} - 3.5$$
$$T_{ARC} < T_{ta} + 5$$

$$\frac{dT_{ARC}}{dt} = 0.6°C \cdot min^{-1}$$

$$\frac{dT_{ARC}}{dt} = \frac{h_{ARC} A_{ARC}}{M_{ARC} C_{p,ARC}} \cdot (T_a - T_{ARC}) + \frac{hA}{M_{ARC} C_{p,ARC}} \cdot (T_{Bat} - T_{ARC})$$

$$T_{ARC} \geq T_{ta} + 5$$

$$T_{Bat} \geq T_{ta}$$

Wait 30min

$$\frac{dT_{ARC}}{dt} = \frac{h_{ARC} A_{ARC}}{M_{ARC} C_{p,ARC}} \cdot (T_a - T_{ARC}) + \frac{hA}{M_{ARC} C_{p,ARC}} \cdot (T_{Bat} - T_{ARC})$$

$$T_{Bat} \geq T_{ARC}$$

$$\frac{dT_{ARC}}{dt} = \frac{dT_{Bat}}{dt}$$

Seek $\frac{dT_{ARC}}{dt} = \frac{dT_{Bat}}{dt}$
20min

$$\frac{dT_{Bat}}{dt} < 0.01°C \cdot min^{-1}$$

$$T_{ta} = T_{ta} + 5$$

$$\frac{dT_{Bat}}{dt} \geq 0.01°C \cdot min^{-1}$$

Exotherm

$$\frac{dT_{ARC}}{dt} = \frac{dT_{Bat}}{dt}$$

$$T_{Bat} > 400°C$$

Cool

$$\frac{dT_{ARC}}{dt} = \frac{h_{ARC} A_{ARC}}{M_{ARC} C_{p,ARC}} \cdot (T_a - T_{ARC}) + \frac{hA}{M_{ARC} C_{p,ARC}} \cdot (T_{Bat} - T_{ARC})$$

Figure 12. Schematic of EV-ARC model for battery TR mechanism.[154] Reproduced with permission.[154] Copyright 2018, Elsevier.
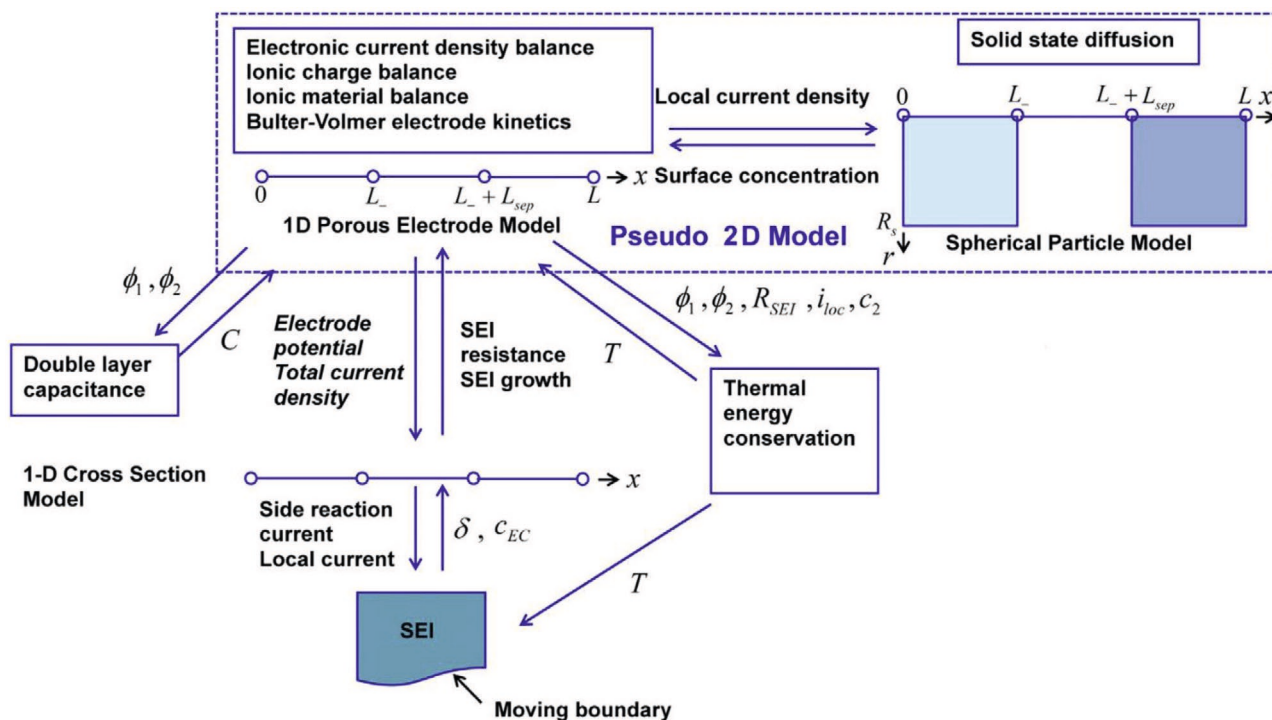
Figure 13. Schematic for the integration of various kinetic models of SEI growth.[155] Reproduced with permission.[155] Copyright 2014, Elsevier.

The rate of reaction between the intercalated Li anode and electrolyte was expressed in terms of the thickness (t_{SEI}) and concentration of SEI layer (c_{SEI})

$$\frac{dc_{Li+Ele}}{dt} = A_{Li+Ele}\,\exp\left(-\frac{E_{a,\,Li+Ele}}{RT}\right)c_{Li+Ele}\,\exp\left(-\frac{t_{SEI}}{t_{SEI,\,Ref}}\right) \qquad (36)$$

4.2. Supercapacitors

There are no recent reports on the kinetic/thermal models for the TR of supercapacitors. The TR of batteries and supercapacitors does not follow the same kinetic/thermal model. The heat dissipation mechanism of the battery and supercapacitor is different.[156] The studies regarding the thermal models of supercapacitors are very limited.[156–160] The internal temperature rise is the most common cause of explosion in any kind of electrochemical device.[159] Large amounts of heat could be produced during the charging/discharging of supercapacitor at a high current rate. Hence, the thermal models are mandatory to design the proper cooling system for supercapacitors to avoid the fire explosion.[157] The findings of some significant studies are discussed in this section.

Guillemet et al. proposed four stages of thermal analysis such as finite element technique, shell network, homogenization method, and ultra-reduced order model to investigate the temperature inside an ultracapacitor.[157] According to the finite element method, the rate of heat generation (Q) and temperature ($T_{(M,t)}$) during the charging and discharging at any position of a supercapacitor was expressed by the heat diffusion equation[157]

$$\nabla\left(-\lambda_{(M)}\,\nabla\tilde{T}_{(M,t)}\right) + c\rho\,\frac{\partial\tilde{T}_{(M,t)}}{\partial t} = \tilde{Q}_v \qquad (37)$$

Steady-state heat transfer equation was used to determine the temperature at any point of the capacitor

$$-\lambda_i\,\nabla^2 T = Q_i \qquad (38)$$

Shell-network thermal model was employed to investigate the temperature in each layer of the capacitor. The important equations of the model are given as follows

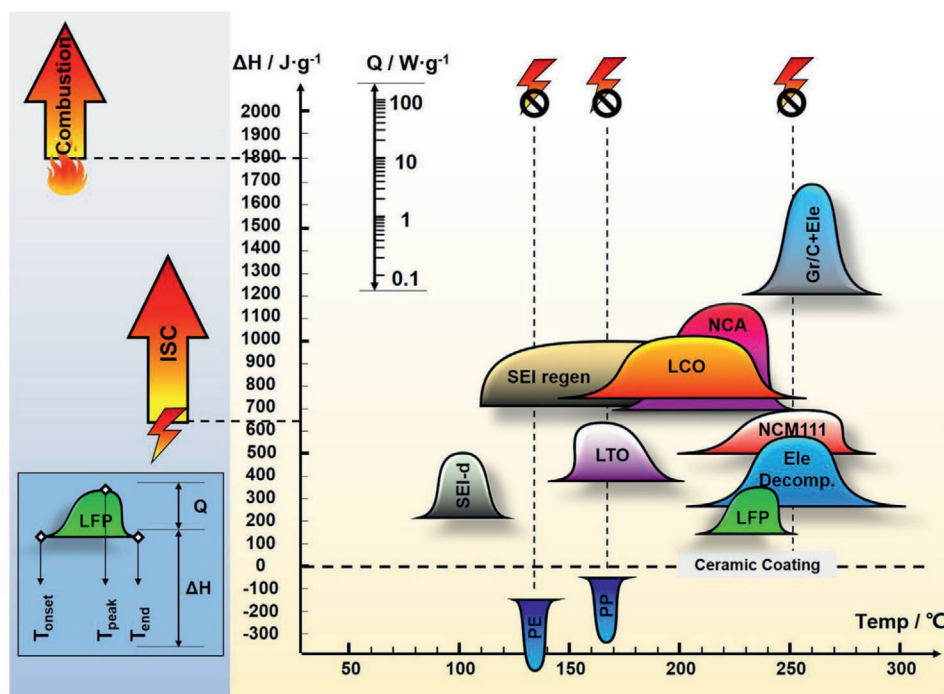$$\frac{d^2\left[T(y)\right]}{dy^2} - [G]\left[T(y)\right] = [Q] \qquad (39)$$

$$T(0) = T_{amb} \text{ and } \frac{dT(y)}{dy}\Big|_{y=L} = 0 \qquad (40)$$

$$T(L) = T_{amb} \text{ and } \frac{dT(y)}{dy}\Big|_{y=0} = 0 \qquad (41)$$

T_{amb} is the ambient temperature. Homogenization technique was utilized to analyze the temperature at any point of the capacitor. Thermal conductivity (λ) at the x-axis and y-axis of the collector is given as follows

$$\lambda_x^{-1} = \alpha\,\lambda_c^{-1} + (1-\alpha)\,\lambda_{es}^{-1} \qquad (42)$$

$$\lambda_y = \alpha\,\lambda_c + (1-\alpha)\,\lambda_{es} \qquad (43)$$

ADVANCED
SCIENCE NEWS
www.advancedsciencenews.com

ADVANCED
ENERGY
MATERIALS
www.advenergymat.de

Figure 14. Energy release diagram of TR proposed by linking the chemical kinetics of around 50 recent investigations.[1] Reproduced with permission.[1] Copyright 2018, Elsevier.

where, x and y are the directions of the device. α is the dimensionless coefficient and es is the electrode separator. c represents the specific heat. Ultrareduced model was commonly used for practical situation of an ultracapacitor, and the analytical calculations of this method were faster as compared to the other models. Thermal conductivity of the capacitor was calculated at various boundary conditions. Thermal analysis of 1D heat transfer in a homogeneous medium could be expressed by a matrix relation

$$\begin{pmatrix} T_{out} \\ \Phi_{out} \end{pmatrix} = \begin{pmatrix} 1 & -R \\ 0 & 1 \end{pmatrix} \begin{pmatrix} T_{in} \\ \Phi_{in} \end{pmatrix} + \begin{pmatrix} Q_{tot}\dfrac{R}{2} \\ Q_{tot} \end{pmatrix} \tag{44}$$

$$T_{out} = -Q_{tot}\frac{R}{2} - R\Phi_{in} + T_{in} \tag{45}$$

$$\Phi_{out} = Q_{tot} + \Phi_{in} \tag{46}$$

$$\Phi_{in} = \frac{T_{in} - T_0}{\dfrac{R}{2}} \tag{47}$$

Thermal analysis of 2D heat transfer could be expressed as follows by considering the x- and y-axes of the device

$$Q_{tot} - 4\left(\frac{T_{max} - T_{x0}}{\dfrac{R_x}{2}}\right) - 4\left(\frac{T_{max} - T_{y0}}{\dfrac{R_y}{2}}\right) = 0 \tag{48}$$

here, T_{in}, T_{out}, Φ_{in}, and Φ_{out} represent the temperature and heat flux of the device inside and outside, respectively. In another study, a thermal model was developed to investigate the

temperature distribution of the supercapacitor as a function of time (t) and position.[159] The thermal model was designed by considering the reversible heat generation in the supercapacitor (activated carbon (AC) double-layer capacitor). This method could be used to study the heat conduction of the device in two or more dimensions. Maxwell BCAP350 F supercapacitor (33 mm diameter and 61.5 mm length) with four internal thermocouples (T_1, T_2, T_3, and T_4) was used in this study. According to this model, the energy equation for the transient heat conduction could be expressed as follows

$$\rho C \frac{\partial T}{\partial t} = \nabla(\lambda \nabla T) + \Phi \tag{49}$$

Experimental results demonstrated that the temperature was increased and decreased in all parts of the supercapacitor during charging and discharging, respectively. Reversible and irreversible heat variation was noted for the charging and discharging processes, respectively. The variation between inside and outside temperatures of the supercapacitor was increased with respect to time. The radial thermal resistance was higher than the axial, and therefore the temperature inside the supercapacitor was more significant as compared to the external surface. The variation of entropy (ΔS) was expressed by considering the Helmholtz model[159]

$$\Delta S = \frac{2k_B}{e} C\Delta U \ln\left(\frac{V_H}{V_e}\right) \tag{50}$$

here, k_B, e, and ΔU denote the Boltzmann constant, electron charge, and voltage variation, respectively. V_H and V_e are the volume of Helmholtz layer and total electrolyte, respectively. ΔS

from an initial to final state for each reversible or charging process could be demonstrated as follows

$$\Delta S = \int_1^2 \frac{dQ}{T} \tag{51}$$

$$ds = C_{Heat} \int_1^2 \frac{dT}{T} \tag{52}$$

The predicted model agreed well with the experimental results for internal and external temperatures of the supercapacitor.

In a similar study, a thermal model was developed to examine the internal temperature of commercial supercapacitors (BCAP0010 and BCAP0350) for industrial applications.[160] The key parameters such as conduction heat transfer, thermal boundary conditions, and convection heat transfer coefficient were discussed in detail. The internal temperature distribution at transient and steady states was modeled through the finite differential method. The heat conduction equation was utilized to study the temperature distribution of the supercapacitor

$$\nabla^2 T + \frac{P}{\lambda} = \frac{\rho C_p}{\lambda} \frac{\partial T}{\partial t} \tag{53}$$

here, ∇^2 and P illustrate the Laplacian operator and local volumetric density, respectively. The model by considering the axial (z) and radial (r) directions of the cylindrical device for the temperature distribution could be expressed as follows

$$\rho C_p \frac{\partial T(r,z,t)}{\partial t} = \lambda_r \frac{\partial^2 T(r,z,t)}{\partial r^2} + \frac{\lambda_r}{r} \frac{\partial T(r,z,t)}{\partial r} + \lambda_z \frac{\partial^2 T(r,z,t)}{\partial z^2} + P \tag{54}$$

Thermal resistance (R) for each layer of the device could be expressed as follows

$$R_{th} = \frac{\ln\left(\frac{r_o}{r_i}\right)}{2\pi\lambda L} \tag{55}$$

where, L, r_o, and r_i represent the length, outside radius, and inside radius of the cylinder, respectively. In a 3D space, two intermediate temperatures such as T^* and T^{**} were considered to model the temperature distribution in various directions.

Radial direction

$$\frac{T^* - T(r,z,\varphi,t)}{\Delta t/2} = \frac{\partial^2 T^*}{\partial r^2} + \frac{1}{r}\frac{\partial T^*}{\partial r} + \frac{1}{r^2}\frac{\partial^2 T(r,z,\varphi,t)}{\partial \varphi^2} + \frac{\partial^2 T(r,z,\varphi,t)}{\partial z^2} \tag{56}$$

Angular direction

$$\frac{T^{**} - T(r,z,\varphi,t)}{\Delta t/2} = \frac{\partial^2 T^*}{\partial r^2} + \frac{1}{r}\frac{\partial T^*}{\partial r} + \frac{1}{r^2}\frac{\partial^2 T^{**}(r,z,\varphi,t)}{\partial \varphi^2} + \frac{\partial^2 T(r,z,\varphi,t)}{\partial z^2} \tag{57}$$

Axial direction

$$\frac{T(r,z,\varphi,t+\Delta t) - T(r,z,\varphi,t)}{\Delta t/2} = \frac{\partial^2 T^*}{\partial r^2} + \frac{1}{r}\frac{\partial T^*}{\partial r} + \frac{1}{r^2}\frac{\partial^2 T^{**}(r,z,\varphi,t)}{\partial \varphi^2} + \frac{\partial^2 T(r,z,\varphi,t+\Delta t)}{\partial z^2} \tag{58}$$

The calculated temperatures at the outside and inside radius of supercapacitor agreed with the numerical results. Thermal resistance of the supercapacitor was calculated from the internal steady-state temperature (T_{cap}), T_{amb}, and heat power loss (P_{loss})

$$R_{th} = \frac{T_{cap} - T_{amb}}{P_{loss}} \tag{59}$$

The assessment of internal temperature and thermal resistance could be utilized to design the proper cooling system of a supercapacitor. First principle calculations with Poisson–Nernst–Planck model could also be used to investigate the heat generation and thermal transport in supercapacitors during the constant current cycling.[158] The influence of diffusion and steric effects on irreversible and reversible Joule heat generation rates was studied by this model.

5. Recent Advances

In the recent years, the thermal stability of electrochemical devices was studied in the range of 80–200 °C. In most of the studies, the cross-sectional scanning electron microscopy (SEM), and transmission electron microscopy (TEM) or high-resolution TEM were used to analyze the morphology of SEs.[161] The microstructure alignment of SE was examined using X-ray computed tomography (XCT).[162] Thermal stability was studied in a hot air oven,[163] hot plate,[161,164] weathering chamber,[161] and thermogravimetric analysis (TGA)[165] at various temperatures. The EV-ARC was also applied to observe the TR of batteries.[166] In most of the studies, hot air oven or hot plate was used to evaluate the high-temperature applications of batteries and supercapacitors.

Batteries:[163] Thermally stable polytetrafluoroethylene (PTFE)-coated cables were used to extend the battery holders into the oven. The temperature inside the oven was regularly monitored using a thermometer. The cells were equilibrated at the required temperature for 1 h before starting the next measurement. Ionic conductivity was measured by holding the samples at a specific temperature and time in the oven. The shrinkage or fire resistance of SEs was tested by placing the samples under the direct flame for ≈1 s.[51]

Supercapacitors:[161,164] The thermal stability of SEs was also assessed on a hot plate for 5 min at different temperatures. The precise temperature of the hot plate was observed by a noncontact infrared thermometer. The shrinkage of SEs was examined after each temperature treatment by measuring the dimensions. Temperature-responsive electrochemical experiments were also executed in a weathering chamber with a k-type thermocouple. A thermal shock chamber was used to evaluate the thermal abuse in the range of 30–130 °C at a heating rate of 5 °C min^{-1}.[166]

DSC thermographs were analyzed at a heating rate of 10 °C min^{-1} after quenching the samples from elevated temperature to ensure the consistency of testing for all samples. TGA analysis was executed at heating rate of 10 °C min^{-1} under nitrogen atmosphere. SEs were placed between the stainless steel and the ionic conductivity was examined by the AC impedance spectroscopy at required frequency and temperature range.[165] Nanoindentation tests were carried out to analyze the

ADVANCED
SCIENCE NEWS
www.advancedsciencenews.com

ADVANCED
ENERGY
MATERIALS
www.advenergymat.de

mechanical properties of SEs under pressure control mode at nanoscale (Hysitron TI 950 TriboIndenter).[165] This is an efficient technique to mimic the punctuation of Li dendrites.

Polydimethylsiloxane was employed to encapsulate the supercapacitors for evaluating the temperature (in the range of −30 to 100 °C)-responsive electrochemical performance.[167] Octane and dry ice mixture was used to examine the anti-freezing applications of flexible supercapacitors.[168]

The significant findings of the recent high-temperature batteries and supercapacitors are highlighted in this section. CPEs were commonly used for the thermal stability of batteries. Ionogels and hydrogels were mostly utilized for high-temperature and sub-zero temperature applications of supercapacitors, respectively.

5.1. Batteries

5.1.1. Ceramic–Polymer Electrolyte

Phase inversion (PI) technology was utilized to design a porous, flexible, and thermally stable CPE membrane for the high-temperature Li-ion batteries.[161] Li iron phosphate ($LiFePO_4$) and lithium titanate ($Li_4Ti_5O_{12}$) composite were used as electrodes. CPE-PI membrane was infiltrated with LP40 electrolyte (1 M $LiPF_6$ in 1:1 ratio of EC/DEC) to evaluate the electrochemical performance. PVDF and Al_2O_3 were employed to produce the CPE. The porous surface features of the electrolyte were engineered through the PI technique with the mixture of N-methyl-2-pyrrolidone (95%) and glycerol (5%) solvent. The pore size, shrinkage, thermal stability, Li dendrite suppression, and wettability of the PE were controlled by incorporating a high weight percentage of Al_2O_3 nanoparticles (70 wt%) into the PVDF matrix. The impact of PI and ceramic filling on the PE was analyzed by the SEM. The cross-sectional SEM images and schematic illustration of PE-PI (**Figure 15**a–c), CPE (Figure 15d–f) and CPE-PI (Figure 15g–i) are shown in Figure 15.

Large voids (≈5 μm) with small pores were introduced on the PE by the PI technique (Figure 15a,b). In the case of CPE without PI, the surface was denser, the pores and voids were not observed (Figure 15d,e). A uniform porous microstructure morphology was perceived for CPE-PI (Figure 15g,h), and this was attributed to the strong interaction of Al_2O_3 nanoparticles with the solvent mixture (glycerol and N-methyl-2-pyrrolidone (95%)) during the PI.[169] Moreover, the voids between the nanoparticles were also retained for the potential Li^+ ion transport. BET surface areas of Al_2O_3, PVDF, CPE, and CPE-PI were 33, 3, 4, and 17 m^2 g^{-1}, respectively. This result confirmed that only 50% of Al_2O_3 surface was covered by the PVDF during the PI. The ionic conductivities of CPE and CPE-PI were 0.0080 and 0.82 mS cm^{-1}, respectively, demonstrating the increase of ionic conductivity via PI.

The thermal stability of CPE-PI was studied in the range of 100–200 °C on a hot plate for 5 min and the results were compared with the commercial Celgard 2325. The shrinkage of Celgard 2325 was started at 105 °C and it was continued with respect to the temperature (**Figure 16**a,b). The shrinkage percentage of Celgard 2325 was higher as compared to the melting point of its constituents (polyethylene (133 °C) and polypropylene (158 °C)).[170] Conversely, CPE-PI showed excellent
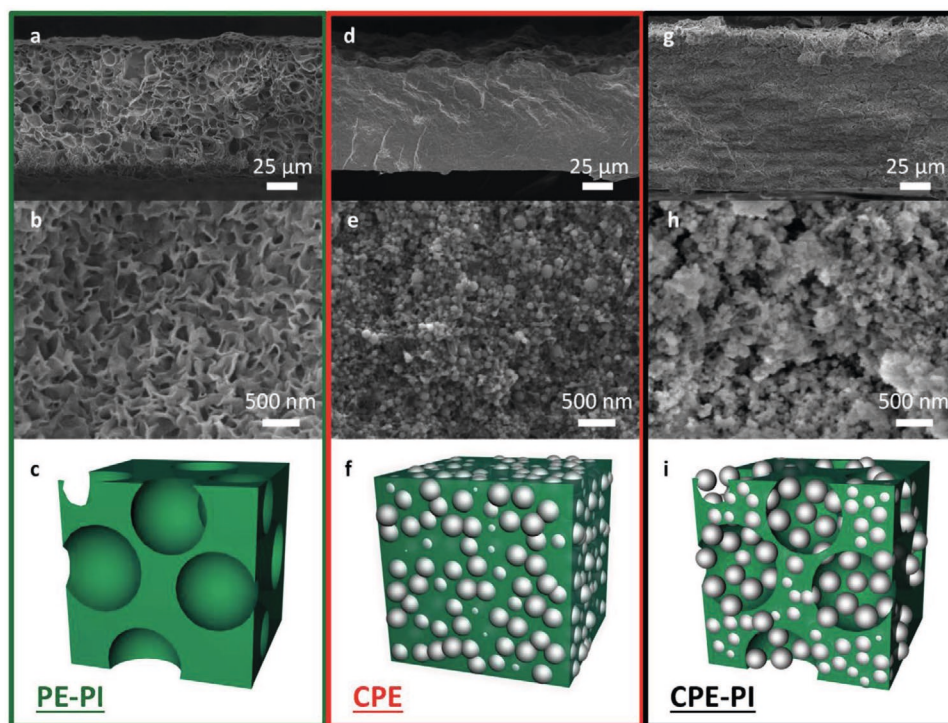

Figure 15. Cross-sectional SEM images and schematic illustration: a–c) PE-PI, d–f) CPE, and g–i) CPE-PI.[161] Reproduced with permission.[161] Copyright 2017, Wiley-VCH.

**ADVANCED
SCIENCE NEWS**

www.advancedsciencenews.com

**ADVANCED
ENERGY
MATERIALS**

www.advenergymat.de

thermal stability with only ≈5% dimensional shrinkage until 200 °C (Figure 16a,b) and the results were in the acceptable range of U.S. Advanced Battery Consortium's goal.[171] This was ascribed to the high weight percent of Al_2O_3 loading and the porosity percentage of CPE-PI (>50%). The electrochemical performance of battery with CPE-PI was also maintained well at 150 °C for 20 h. The ionic conductivities of PE, CPE, PE-PI, and CPE-PI are displayed in Figure 16c. The temperature-dependent ionic conductivities of CPE-PI and Celgard 2325 were analogous, indicating the similar ionic conduction mechanism. Moreover, the activation energy of CPE-PI (10.6 kJ mol^{-1}) was almost equal to that of Celgard 2325 (10.8 kJ mol^{-1}). CPE-PI was performed well in the Li-ion battery without any failure in activity for >4000 h, suggesting the suppression of Li dendrite formation. Conversely, the bare PE, CPE, and Celgard 2325 performance failed around 85, 500, and 3500 h, respectively. PI technique could also be utilized to fabricate the flexible SEs through the 3D printing.

In a similar study, a thermally stable CPE-PI (trademarked as Pyrolux) membrane was infiltrated with a high-temperature LE (1 M lithium bis(oxalato)borate (LiBOB) in 1:1 ratio of EC/propylene carbonate, and 5% vinylene carbonate) for high-temperature Li-ion batteries.[163] The efficiency of Pyrolux was compared to Celgard 2325 membrane infiltrated with LP40

electrolyte (1 M LiPF$_6$ in 1:1 ratio of EC/DEC). The schematic of synthesis (**Figure 17**a), flexibility (Figure 17d), and hierarchical nanoporosity (achieved around 45%) of Pyrolux membrane film (Figure 17e) are shown in Figure 17. The photographs of Pyrolux ink and the film prepared by the doctor blade method are shown in Figure 17b,c, respectively.

The unique features of Pyrolux could enhance the mechanical robustness, thermal stability, and electrochemical performance. The thermal stability of Pyrolux and Celgard 2325 was analyzed by the TGA and flame resistance test (**Figure 18**). A slight shrinkage was observed for Pyrolux, but the Celgard 2325 was completely shattered (Figure 18a–c) during the flame exposure. Moreover, the flame of resistance of Pyrolux was also sustained after the ingestion of LE (Figure 18d–f). TGA results showed that Pyrolux was thermally stable even at 800 °C (Figure 18g), and the shape of the polymer disc was also maintained well (inset of Figure 18g). Isothermal TGA at 200 °C demonstrated that Pyrolux was stable till 20 h, while the Celgard 2325 had lost around 20% of its weight within 2 h and ≈50% degradation was noted at 20 h (Figure 18h). For Celgard 2325, the ionic conductivity was increased with respect to temperature till 90 °C, and after that, it was decreased due to the poor permeability and shrinkage of the polymer. In the case of Pyrolux, ionic conductivity was increased to 5.76 mS cm^{-1} after
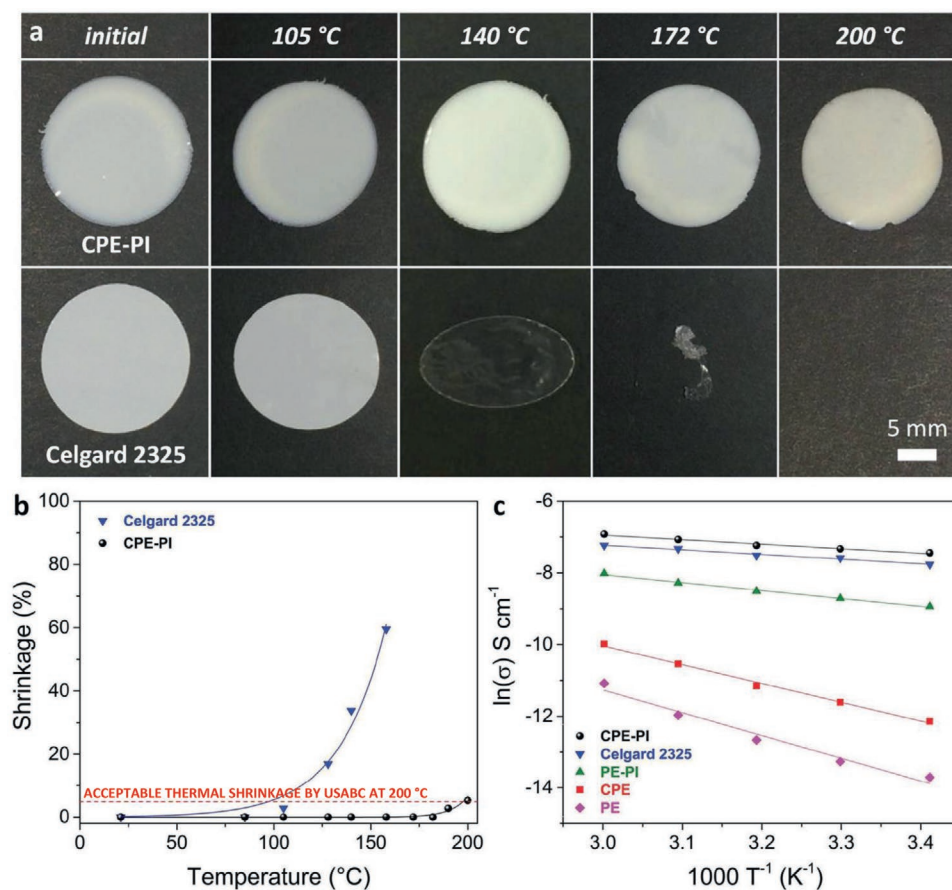
Figure 16. CPE-PI and Celgard 2325: a,b) photographs and the dimensional shrinkage percentage at various temperature and c) ionic conductivity with respect to temperature.[161] Reproduced with permission.[161] Copyright 2017, Wiley-VCH.
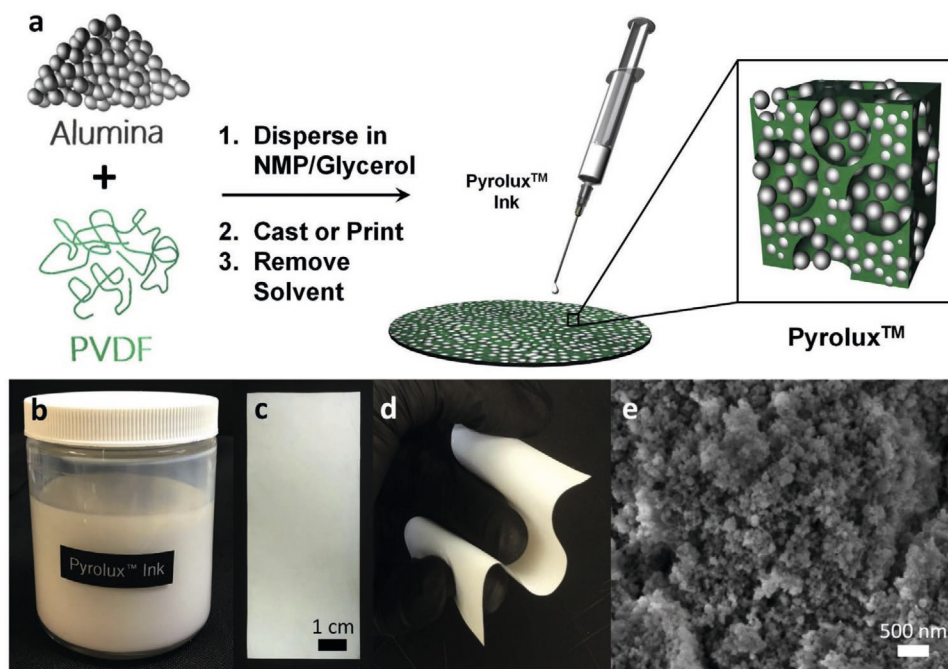
Figure 17. Pyrolux: a) schematic of synthesis, b) photograph of ink, c,d) photographs of film prepared by doctor blade method, and e) cross-sectional SEM image.[163] Reproduced with permission.[163] Copyright 2019, Elsevier.
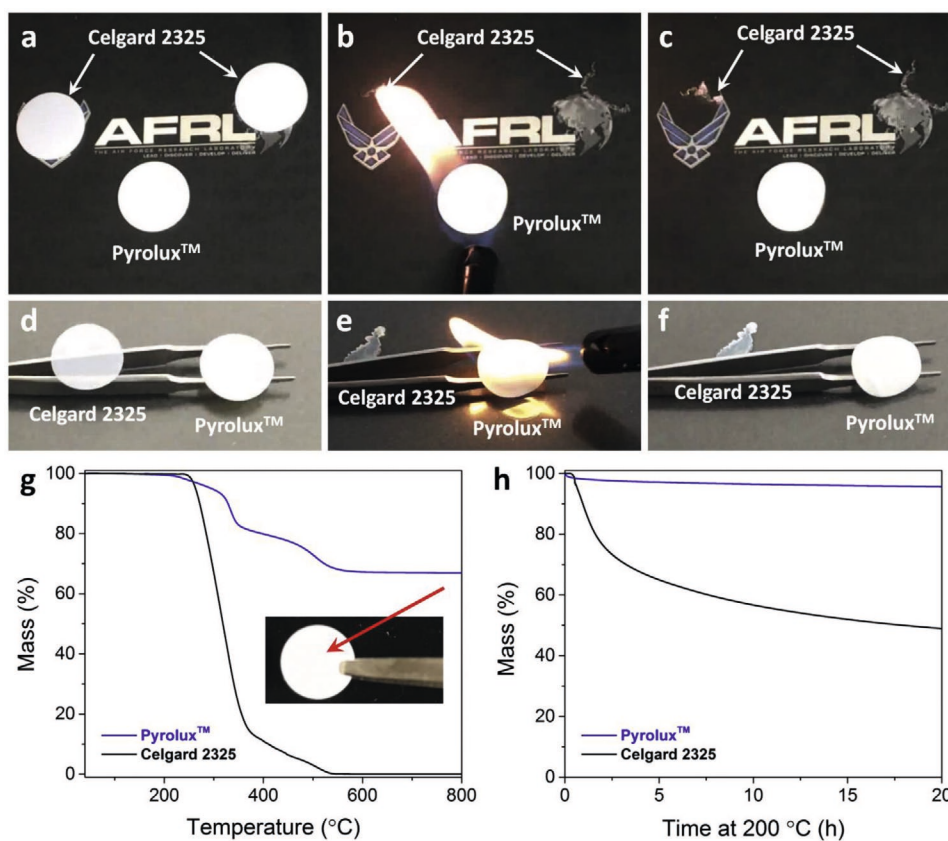
Figure 18. Pyrolux and Celgard 2325: flame resistance test before LE infiltration—a) before, b) during, and c) after; flame resistance test after the LE infiltration—d) before, e) during, and f) after; g) TGA thermograms with a constant heating rate of 10 °C min⁻¹ (inset shows the photograph of 0.95 cm Pyrolux disc after 800 °C); and f) isothermal TGA graphs at 200 °C for 20 h.[163] Reproduced with permission.[163] Copyright 2019, Elsevier.

**ADVANCED
SCIENCE NEWS**

www.advancedsciencenews.com

**ADVANCED
ENERGY
MATERIALS**

www.advenergymat.de

1 h at 120 °C and it was retained well even after 7 days duration at this same temperature, suggesting the high-temperature stability of the material.

At 120 °C, the reversible capacity of half-cells with Pyrolux was 340 and 155 mAh g^{-1} for Li//graphite and Li//LiFePO$_4$, respectively. Pyrolux was more stable in Li//graphite half-cells with a columbic efficiency of 99.4% over 100 cycles, suggesting the graphite exfoliation was prevented by the electrolyte at high temperature. The half-cells with Celgard 2325–electrolyte failed at this temperature range. The electrochemical performance of the membrane–electrolyte system was also evaluated in Li//graphite full cells at various temperatures such as 20, 60, 90, and 120 °C. The voltage profiles of Pyrolux were not influenced by the temperature, even at 120 °C and 50 cycles. Conversely, the specific capacity and CE of Celgard 2325 were severely affected at ≥90 °C. The durability of Pyrolux system at high temperatures and long-term exposures was attributed to the preservation of its surface morphology.
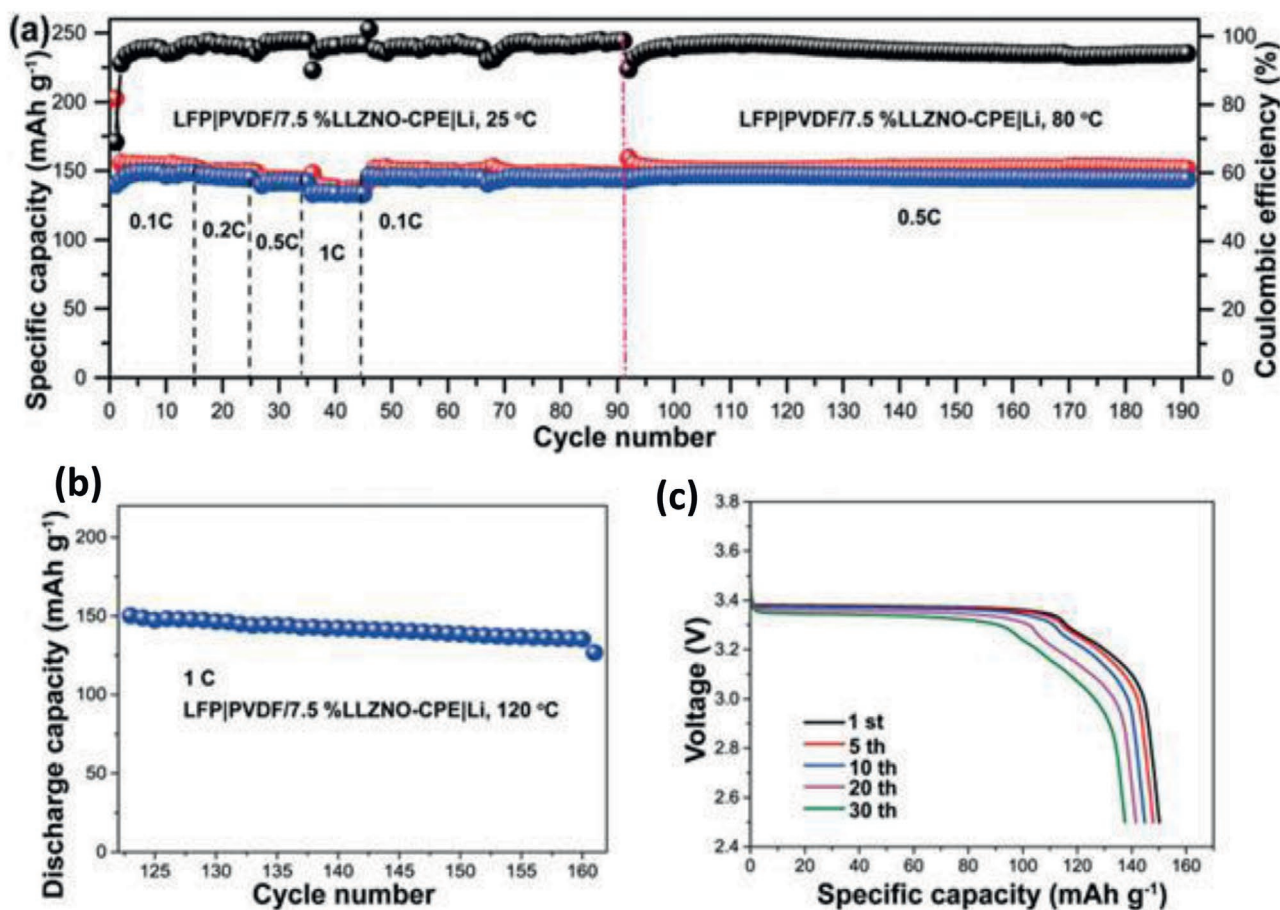
In a similar study, a flexible and thermally stable CPE was fabricated using PVDF, Li$_{6.75}$La$_3$Zr$_{1.75}$Nb$_{0.25}$O$_{12}$ (LLZNO), and LiClO$_4$.[51] CPE was fabricated via the direct casting technique using DMF solvent, and the electrochemical measurements were carried out in a coin cell with LiFePO$_4$ cathode and Li metal anode. The ceramic particles were uniformly dispersed on the smooth polymer surface. The tensile strength and elongation of CPE were decreased as the content of LLZNO increased and therefore the content of LLZNO in CPE was optimized as 7.5 wt%. The cross-linking structure of the polymer chain was broken at high LLZNO content. The ionic conductivity of CPE was 0.92×10^{-4} S cm^{-1} at 25 °C, and it was further improved to 1.5×10^{-3} S cm^{-1} after wetting with a nonflammable IL (LiTFSI, IL). TGA results revealed that pure PVDF was thermally stable until 400 °C. However, the CPE started to decompose after 100 °C, and this was accredited to the decomposition of Li salts at high temperatures. Thermal stability of CPE was investigated at various temperatures (in the range of 150–350 °C) in a muffle furnace for 10 min (**Figure 19**a). Thermal stability of the electrolytes was in the following order: CPE/IL > CPE > commercial polypropylene (PP). The flammability test was also carried out using an alcohol lamp and the results showed that the burning degree of CPE/IL was slightly weaker as compared to the CPE (Figure 19b). The electrochemical performance of LiFePO$_4$/CPE/Li cell was evaluated at 80 °C and 0.5 C current density. The discharge capacitance of the cell was retained well, even after 100 cycles, and it was not affected by the temperature (**Figure 20**a). The temperature was further increased to 120 °C and the cell performance was further tested at 1 C current density (Figure 20b,c). The specific discharge capacities were 150.1 and 137.5 mAh g^{-1} at 1st and 30th cycles, respectively. The cyclic stability of CPE/IL was compared with the commercial PP in Li|Li symmetric cells. The cell with CPE/IL exhibited a continuous potential polarization after cycling for 1200 h, and it was more stable, compared to PP, at a current density of 0.2 mA cm^{-2}, indicating the suppression of Li dendrites. CPE could also be utilized for high-voltage Li batteries because its electrochemical window was higher than 4.6 V.

In another study, 2D few layer vermiculite clay sheets (VS, layered magnesium aluminosilicate with ≈ 1.5 nm thickness)
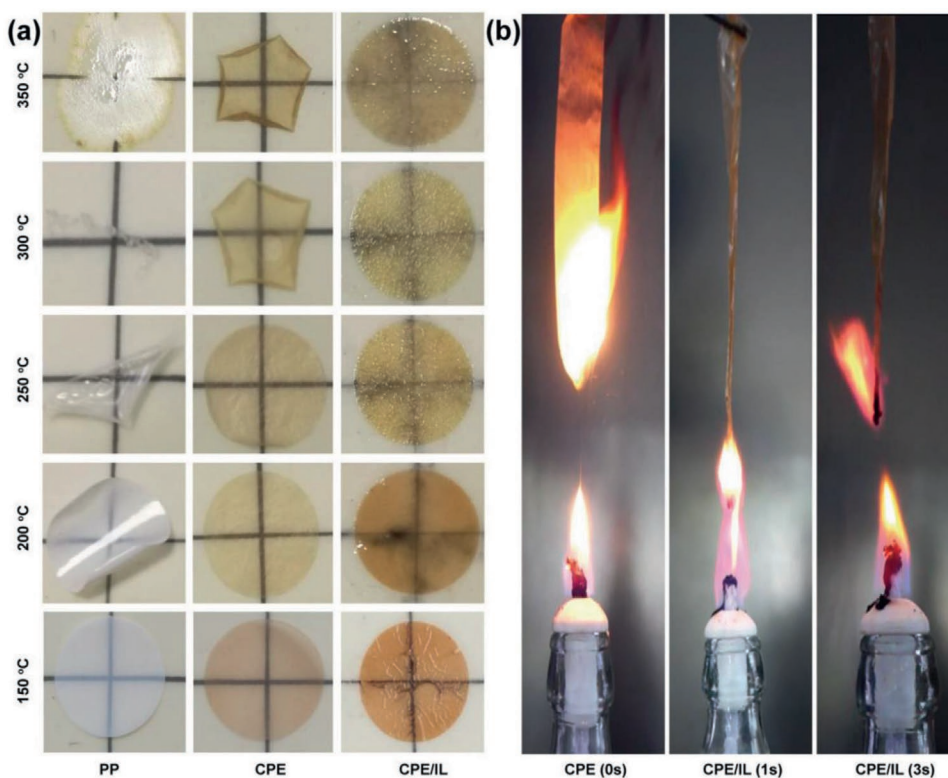
Figure 19. a) Thermal stability of PP, CPE, and CPE/IL at various temperatures for 10 min and b) photographs of flame test on CPE discs using alcohol lamp at 0, 1, and 3 s.[51] Reproduced with permission.[51] Copyright 2019, Wiley-VCH.
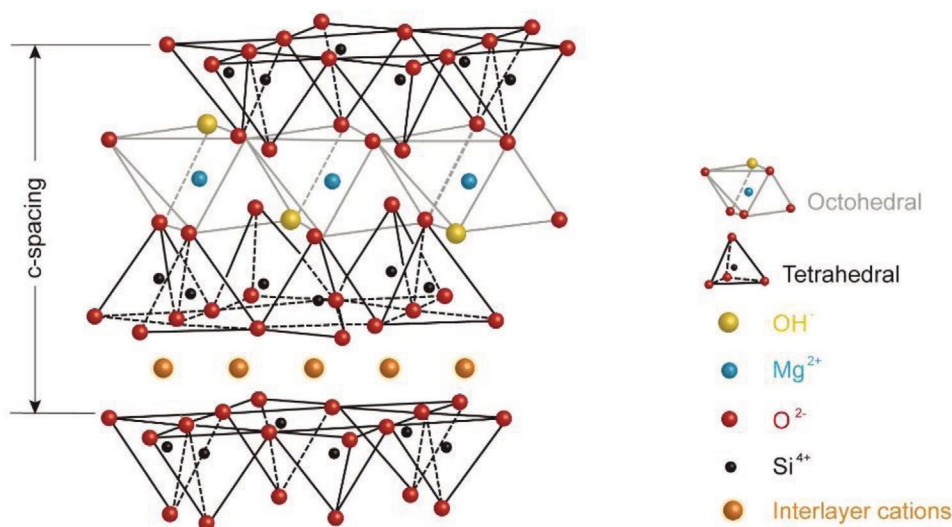
**ADVANCED
SCIENCE NEWS**

www.advancedsciencenews.com

**ADVANCED
ENERGY
MATERIALS**

www.advenergymat.de

Figure 20. Cycle performance of LiFePO$_4$/CPE/Li cell: a) 25 and 80 °C at 0.5 C current density for 100 cycles and b,c) 120 °C at 1 C current density.[51] Reproduced with permission.[51] Copyright 2019, Wiley-VCH.

were incorporated into the PEO to enhance the thermal stability, mechanical durability, and electrochemical stability.[165] The schematic of structural model and arrangement of atoms in the 2D layered vermiculite clay sheets are displayed in **Figure 21**. The flexible electrolyte was fabricated from PEO, VS, and LiTFSI through the solution-casting technique in acetonitrile at 50 °C. The melting point of PEO was decreased from 63 to 49 °C after the addition of LiTFSI and it was further reduced to 43.5 °C after adding 10 wt% VS, suggesting the decrease of crystallinity of the polymer.

The thermal and mechanical stability of PEO/LiTFSI and PEO/LiTFSI/10 wt% VS is shown in **Figure 22**. The results demonstrated that PEO/LiTFSI was not thermally stable at temperatures above 120 °C and the polymer disc was destroyed by catastrophic shrinkage (Figure 22a). By contrast, the dimensional stability of PEO/LiTFSI/10 wt% VS was maintained over 200 °C for 30 min, indicating the 2D clay sheets could restrict the catastrophic shrinkage of PEO. It was predicted that the Li dendrite growth was normally controlled by the separator/membrane with shear modulus higher than 6 GPa.[172] The Young's modulus of VS was higher than 175 GPa, which could easily hinder the Li dendrite growth through mechanical resistance.[173] Nanoindentation test demonstrated that the displacement for PEO/LiTFSI/10 wt% VS and PEO/LiTFSI were

161 nm/77.5 and 240 nm/137 nm after the loading/unloading of 2 µN, respectively (Figure 22b). The moduli of PEO/LiTFSI/10 wt% VS and PEO/LiTFSI were predicted as 35.4 and 23.5 MPa, respectively. The tensile strength of PEO/LiTFSI/10 wt% VS (0.8 MPa) was twofold higher than pure PEO/LITFSI (0.4 MPa) (Figure 22c). The high tensile strength could suppress the Li dendrite growth during the galvanostatic cycling in Li-ion cells. The unique mechanical and thermal characteristics of the electrolyte were accredited to the 2D morphology and effective interface of VS filler with the polymer matrix.

The impedance and ionic conductivity of the PE were measured at various temperatures (**Figure 23**a,b). The results showed that the ionic conductivity was increased with respect to temperature, indicating the interface between the PEO and VS was higher after heating. The polymer composite with 10 wt% of VS showed the highest ionic conductivity as compared to that of 5, 15, and 20 wt% (Figure 23c). At 25, 60, and 100 °C, the ionic conductivities of PEO/LiTFSI/10 wt% VS were 2.9×10^{-5}, 1.2×10^{-3}, and 3.1×10^{-3} S cm^{-1}, respectively, and these values were much higher as compared to the same electrolyte without VS. The mechanism for the superior ionic conductivity of PEO/LiTFSI/10 wt% VS is schematically shown in Figure 23d. The segment motion of the PE for Li$^+$ ion transport was endorsed by the high active interface between the

ADVANCED
SCIENCE NEWS
www.advancedsciencenews.com

ADVANCED
ENERGY
MATERIALS
www.advenergymat.de

Figure 21. Schematic of structural model and arrangement of atoms in the layered vermiculite clay sheets.[165] Reproduced with permission.[165] Copyright 2018, Wiley-VCH.

PEO and 2D VS. More conducting Li+ ions were produced by the electronegative silicate on the VS surface through the dissociation of LiTFSI. Consequently, the 2D VS could enhance the Li+ transference number (t_{Li+}) on the PE to enhance the ionic conductivity. At 90 °C, t_{Li+} values of PEO/LiTFSI/10 wt% VS and PEO/LiTFSI were 0.497 and 0.203, respectively. Linear sweep voltammetry results demonstrated that the steady-state voltages of Li-ion cells with PEO/LiTFSI/10wt% VS and PEO/LiTFSI at 100 °C were 5.0 and 4.5 V, respectively. Moreover, the voltage profiles of Li-ion cells with PEO/LiTFSI/10wt% VS were not significantly altered over 2 months of operation, suggesting the 2D VS could prevent the Li dendrite formation. Conversely, the cells without VS were short-circuited after 15 days during cycling.

In another study, the CPE was fabricated using PEO, LiTFSI, and garnet-type tantalum-doped $Li_7La_3Zr_2O_{12}$ (LLZTO) for high-temperature Li metal batteries with 3D Li anode (Li metal was confined in a 3D Ni foam[52]) and $LiFePO_4$ (LFP) cathode.[174] 3D Li metal anode could effectively prevent the Li dendrite growth and enhance the safety features of the device.[175,176] The materials were assembled in a 2032-type coin cell with a conductive carbon sponge. The thickness of polymer layer in CPE disk was ≈8 μm. All the electrochemical experiments were carried out by preheating the cells at 90 °C for 5 h. The schematics of interface layer formation and the electrochemical performance of CPE at 90 °C are shown in **Figure 24**. A molten or viscous polymer interface layer was formed in the CPE at 90 °C and this could endorse the solid–solid contact between the electrode
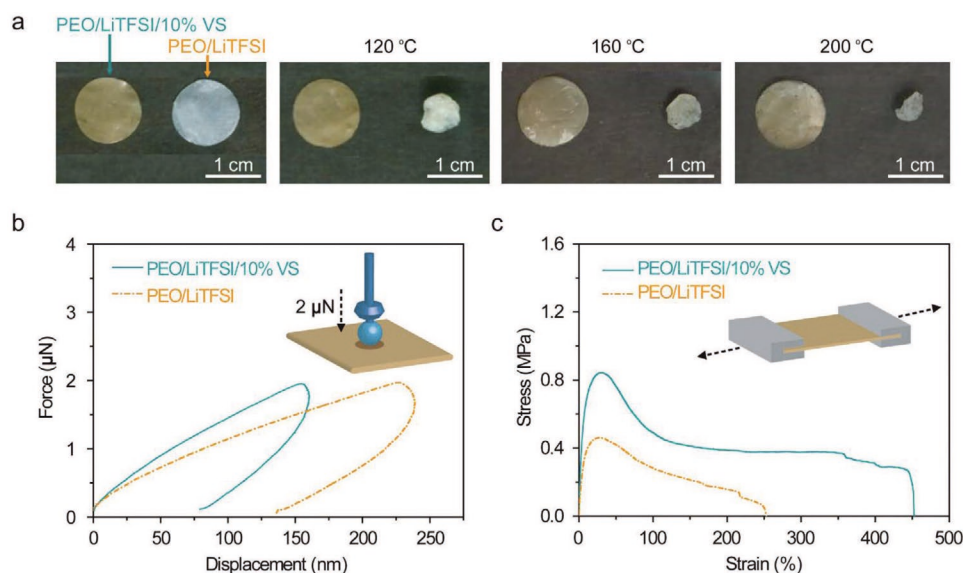

Figure 22. PEO/LiTFSI/10 wt% VS and PEO/LiTFSI: a) photographs of polymer discs at various heat treatment for 30 min, b) load–displacement graphs during the nanoindentation test, and c) stress–strain curves during the tensile test.[165] Reproduced with permission.[165] Copyright 2018, Wiley-VCH.
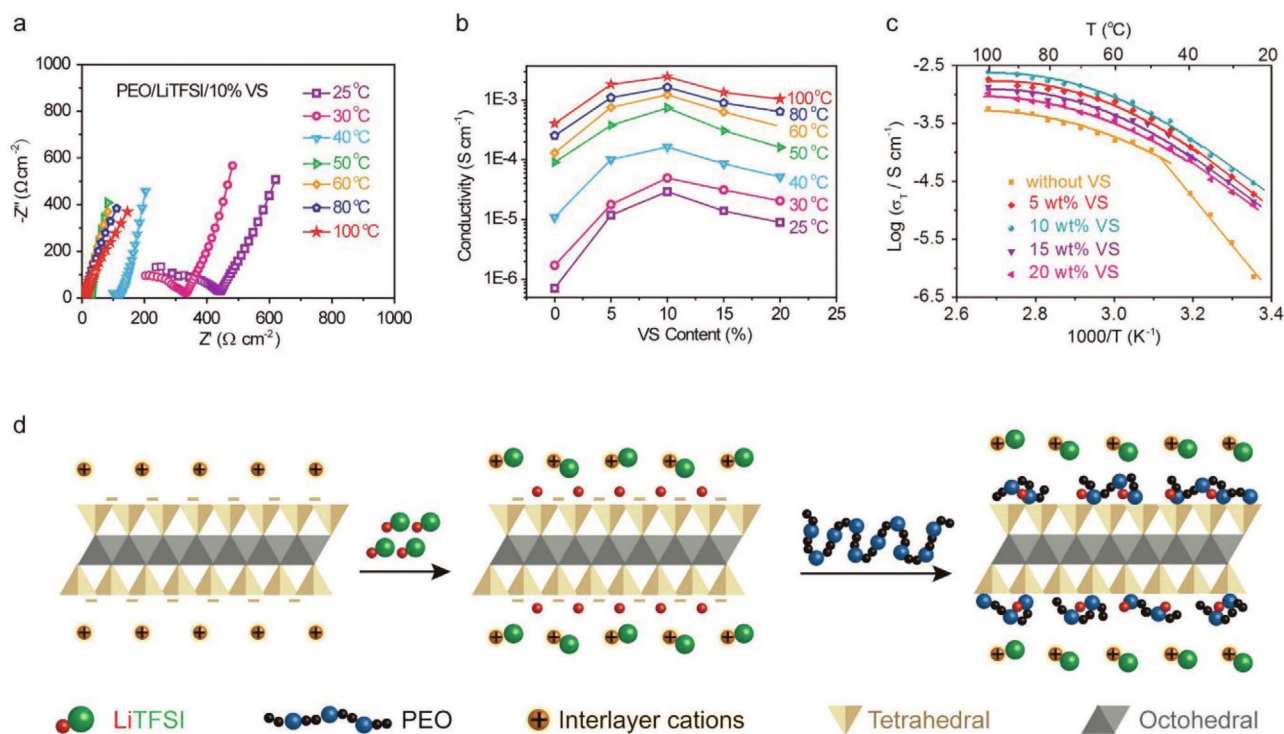
Figure 23. Temperature-responsive PEO/LiTFSI/10 wt% VS: a) impedance spectra, b) ionic conductivity, c) ionic conductivity at various VS content, and d) schematic of ionic conductivity mechanism.[165] Reproduced with permission.[165] Copyright 2018, Wiley-VCH.

and electrolyte. The solid state of the polymer layer was recovered at room temperature after the cycling experiments. The ionic conductivity of Li metal batteries was increased with respect to temperature from 15 to 90 °C, and this was ascribed to the diffusion of Li ions from LLZTO into the PE at high temperature. The electrochemical window of CPE was slightly more stable (4.6 V) as compared to pure PE (4.2 V) at 90 °C. The long-term stability of 3D Li metal batteries was compared to normal Li metal batteries with CPE for 700 h cycling at 90 °C and current density of 0.2 mA cm^{-2}. The voltage profile of 3D
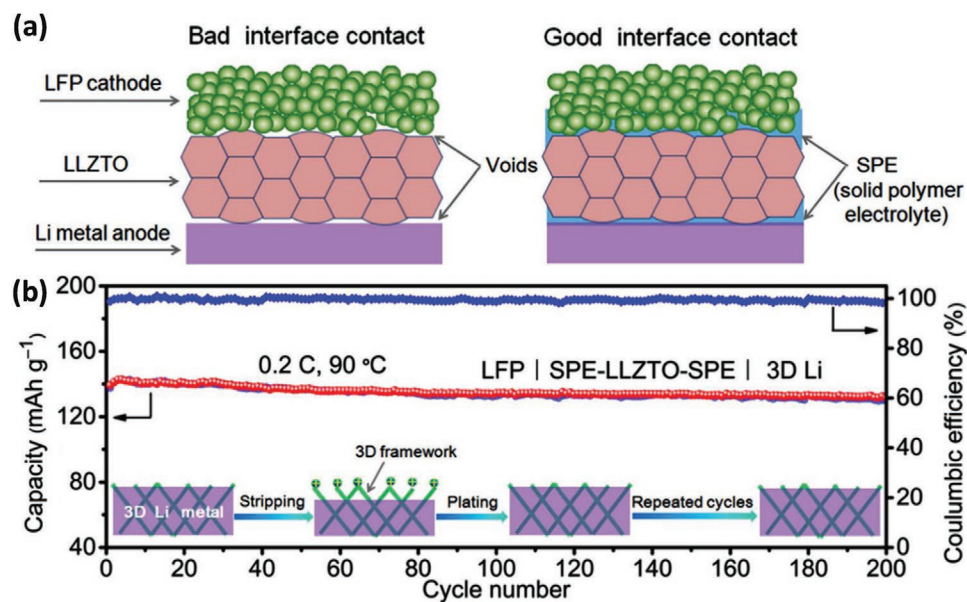
Figure 24. Li metal batteries with CPE electrolyte, 3D Li anode, and LFP cathode: a) schematic of interface layer formation in the presence and absence of polymer and b) electrochemical performance at 90 °C and 0.2 C for 200 cycles (inset: the uniform distribution of Li$^+$ in the 3D network to suppress the Li dendrite growth).[174] Reproduced with permission.[174] Copyright 2019, Elsevier.

**ADVANCED
SCIENCE NEWS**

www.advancedsciencenews.com

**ADVANCED
ENERGY
MATERIALS**

www.advenergymat.de

Li metal batteries was more stable even after 700 h. However, the voltage plateau of pure Li metal batteries was fluctuated and it was dropped into 0 around 140 h, suggesting more Li dendrite growth on pure Li metal batteries.[177] The interfacial resistance of the batteries with pure Li metal (≈2000 Ω) was also higher as compared to that of 3D Li metal (750 Ω) after 100 h cycling. The specific charge capacity and columbic efficiency of 3D Li metal batteries with CPE after 200 continuous cycles were 135 mA h g−1 and 99.6%, respectively.

5.1.2. Polymer Electrolyte

A temperature-responsive polymer electrolyte (PPE) was introduced for the safe operation of Li metal batteries at elevated temperatures.[166] PPE consisted of two polymers such as poly(ethylene glycol) methyl ether methacrylate (PEGMA) and 2,2,3,3,3-pentafluoropropyl acrylate (PFE). The temperature response behavior of PPE in Li metal batteries is schematically shown in **Figure 25**. Anionic and thermal free radical polymerizations were involved between PEGMA and PFE at ambient and elevated temperatures, respectively. A polymer protection layer was formed on the Li anode through anionic polymerization (Figure 25a), which could prevent the Li dendrites growth.

The electrolyte was heated from 20 to 130 °C at a rate of 5 °C min−1 and the sample was maintained at 130 °C for 30 min. The phase transformation of electrolyte through thermal free radical polymerization is shown in Figure 25b. At the thermal abuse condition, the liquid-state PE was transformed into the solid state. Around 90% of LE was transformed into polymer within 20 min at 130 °C. This was ascribed to the establishment of thermal polymerization at high temperature by 2-(1-cyano-1-methylethyl)azocarboxamide. The charge plateau of LiFePO4/PPE/Li pouch cell was 100% in the range of 30–280 °C, and a fully charged pouch cell was continued on a discharge state of 3.4 V without any explosion or short-circuit after 2 h of storage at 130 °C. At the same temperature, the pouch cell with commercial carbonate electrolyte was expanded and short-circuited within 10 min. TGA and differential scanning calorimeter (TGA–DSC) results revealed that the thermal polymerization temperature was around 128 °C. TGA results also showed that only 8 wt% of PPE was degraded before 220 °C and the complete thermal decomposition occurred at 350 °C. Most of the commercial LEs used in this study were degraded before 210 °C. The charge–discharge characteristics of the pouch cell were not much influenced after the thermal abuse. A fully charged LiFePO4/PPE/Li pouch cell could still light up a blue LED lamp between 30 and 150 °C for 1 h. The cell could deliver
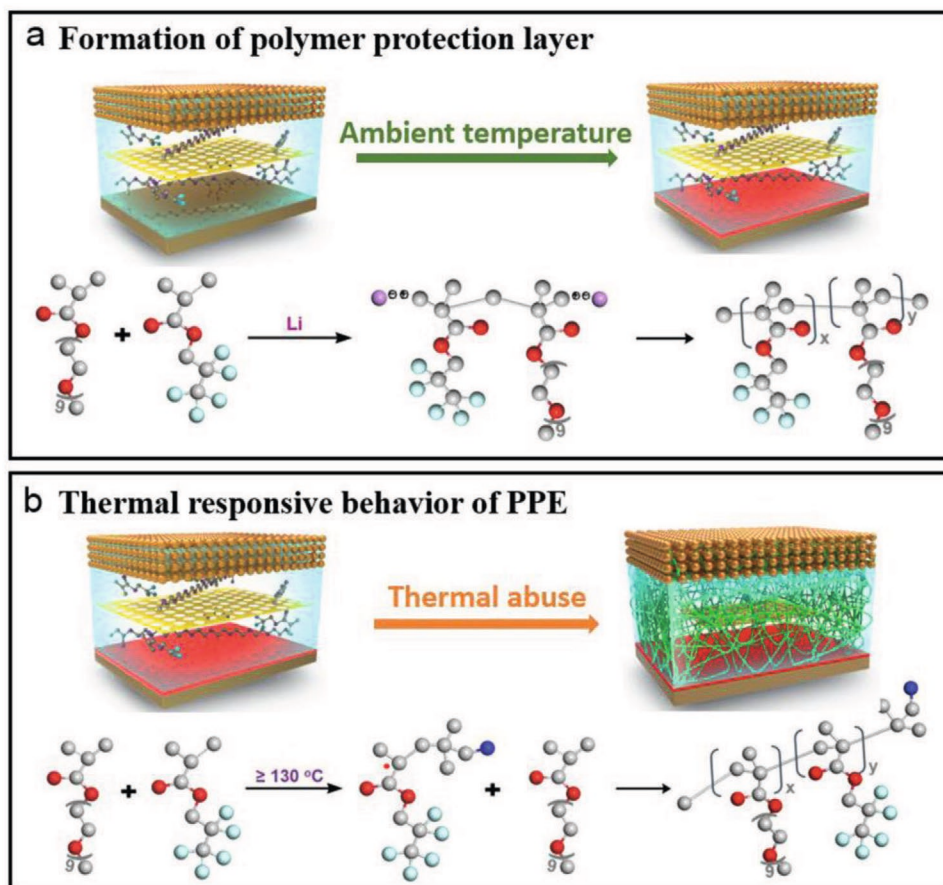
Figure 25. Schematic of polymer protection layer formation and the polymerization mechanism: a) anionic polymerization at ambient temperature and b) thermal free radical polymerization at ≥130 °C.[166] Reproduced with permission.[166] Copyright 2020, Wiley-VCH.

a discharge capacity of 145 mAh g^{-1} at 30 °C with 95% capacity retention for 200 cycles.

5.2. Supercapacitors

5.2.1. Ionogels

Ionogels are solid or quasi-SEs with significant mechanical and thermal properties.[178] Ionogel electrolytes could be used to design the flexible supercapacitors with a wide potential window with high ionic conductivity.[179] It is composed of an IL, polymer, and organic–inorganic hybrid material.[15] In a recent study, an aligned and porous ionogel SE was engineered through self-initiated cyropolymerization with solvent replacement and directional freezing technique for the high-temperature supercapacitors.[162] The porous and aligned ionogels were synthesized using the precursors such as titanium dioxide (TiO$_2$) nanoparticles, clay nanosheets, *N,N*-dimethylacrylamide,1-butyl-3-methyl imidazolium terafluoroborate (DBMIT), and water. For comparison, the porous nonaligned ionogel was also synthesized without the directional freezing technique. According to the mercury intrusion analysis, the open porosity percentage of aligned ionogel was higher (90%) than that of nonaligned ionogel (54%). The nature of open and closed ionogel pores was further investigated through the XCT technique (**Figure 26**).

Simulations such as "pore only" and "two-phase" were conducted to investigate the directional relative diffusivities of aligned and nonaligned ionogels. The aligned and nonaligned ionogels possessed anisotropic and isotropic transport properties. The relative diffusivities may vary with respect to the direction considered for the simulations. For aligned ionogels, direction 1 (through-plane direction) was highly favorable for the ionic transport. In direction 2, the ionic transport was almost similar in both ionogels, because the ionic transport of
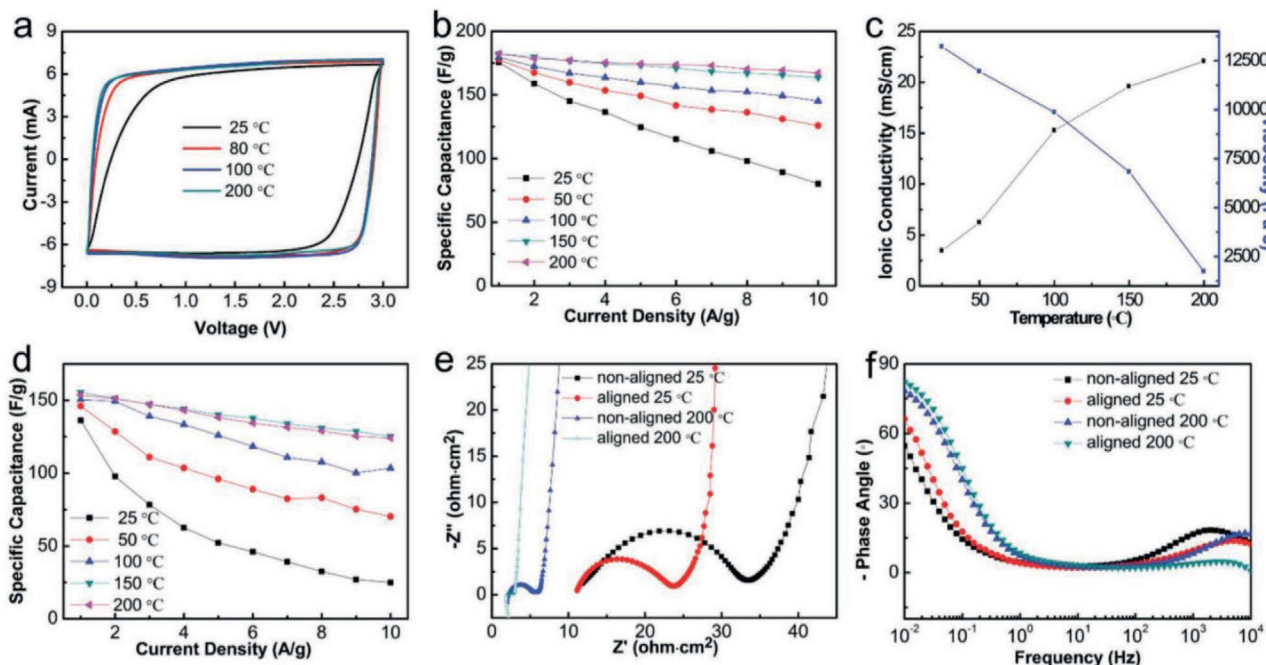
the aligned ionogels was hindered by the struts. TGA results showed that the aligned ionogels had higher thermal stability up to 400 °C. To evaluate the thermal stability, the aligned ionogels–supercapacitors were studied at various temperatures such as 25, 80, 100, and 200 °C. Temperature-dependent CV curves, specific capacitance, ionic conductivity, Nyquist plots, and Bode plots of the aligned ionogels–supercapacitors are displayed in **Figure 27**. The ionic conductivity (from 3.5 to 22.1 mS cm^{-1} (Figure 27a) and specific capacitance (from 80 to 167 F g^{-1} (Figure 27b) were increased as the temperature increased from 25 to 200 °C. By contrast, the viscosity was decreased from 13 216 to 1737 Pa s^{-1} (Figure 27c. The specific capacitance of nonaligned ionogels at various temperatures is shown in Figure 27d. The electrochemical performance of aligned ionogels–supercapacitors was superior as compared to that of nonaligned ionogels (Figure 27e). Moreover, the Bode plots (Figure 27f) showed that the high-temperature capacitive performance of aligned ionogels–supercapacitors was also maximum (phase angle –82.1° at 200 °C and 10 mHz), indicating the availability of more surface area.

In a similar study, a flexible and durable double-networked (DN) ionogel electrolyte was developed for the high-temperature supercapacitor.[179] The schematics of DN ionogel electrolyte synthesis for the first and second network are shown in **Figure 28**a,b, respectively. DN polymer matrix was fabricated through a two-step thermally initiated free radical polymerization using densely cross-linked PVA (C-PVA) and coarsely cross-linked poly(2-hydroxyethyl methacrylate) (HEMA). *N,N'*-methylene-bis-acrylamide (MBAA), potassium persulfate (K$_2$S$_2$O$_8$), and 1-ethyl-3-methylimidazolium tetrafluoroborate (EMIMBF$_4$) were used as the cross-linker, initiator, and IL, respectively. Physically interpenetrating network (PIN) ionogels were also synthesized for comparison using pure PVA and HEMA.

The tensile strength of DN ionogel was around six times higher (3.2 MPa) than that of PIN ionogels (0.5 MPa) at
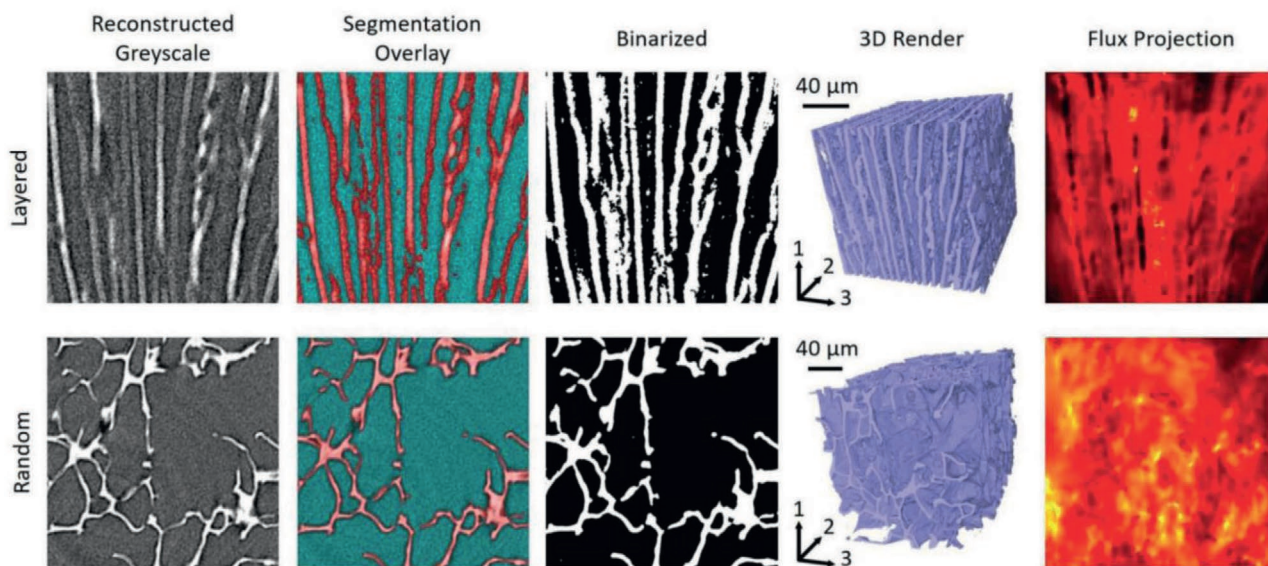
Figure 26. XCT: 3D microstructures of aligned (layered) and nonaligned (random) ionogels—reconstructed grayscale, segmentation overlay, binarized, 3D segmented, and projected flux density images.[162] Reproduced with permission.[162] Copyright 2019, Wiley-VCH.

ADVANCED
SCIENCE NEWS
www.advancedsciencenews.com

ADVANCED
ENERGY
MATERIALS
www.advenergymat.de

Figure 27. Temperature-dependent electrochemical performance of ionogel supercapacitors: a) CV curves of aligned, b) specific capacitance with respect to current density of aligned, c) ionic conductivity and viscosity of aligned, d) specific capacitance with respect to current density of nonaligned, e) Nyquist plots, and f) Bode plots.[162] Reproduced with permission.[162] Copyright 2019, Wiley-VCH.

30 °C. The toughness (dissipation energy 911 kJ m⁻³) and stretchability (250% strain) of DN ionogel were also higher as compared to PIN ionogels. The stretchability of DN ionogel was

increased from 250% to 400% as the temperature raised from 30 to 100 °C, while at the same time, the toughness and tensile strength were decreased. By contrast, the PIN ionogels started
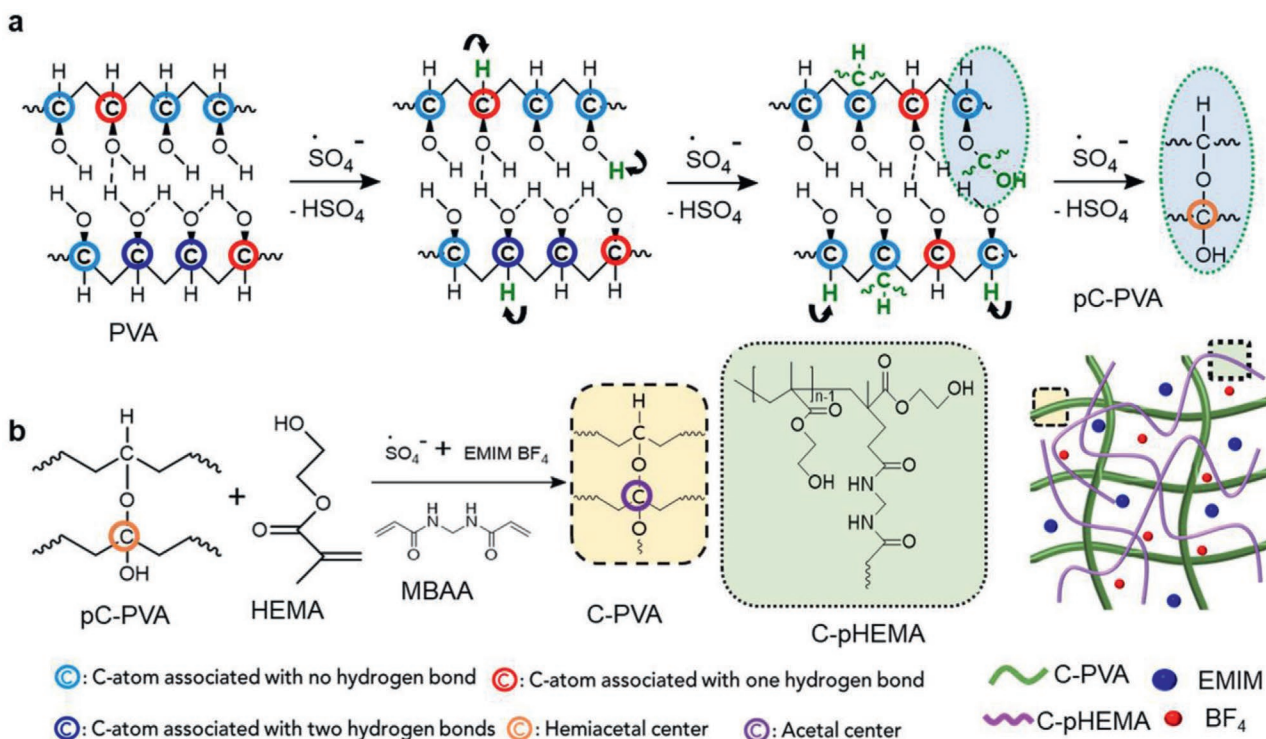
Figure 28. Schematic of DN ionogel electrolytes synthesis (C, cross-linked; pC, partially cross-linked): a,b) reactions for first and second networks.[179] Reproduced with permission.[179] Copyright 2019, Elsevier.

to melt at 100 °C. TGA results showed that DN ionogel was thermally stable up to 300 °C, indicating a stable PE for high-temperature supercapacitor. The ionic conductivity was improved from 0.6 to 1.8 mS cm^{-1} as the IL content was varied from 20 to 60 wt%, signifying the availability of more ion carriers. The ionic conductivity of DN ionogel with 60 wt% of IL also increased from 1.8 (at 30 °C) to 118.6 mS cm^{-1} (at 180 °C) with respect to temperature, and the values were preserved even after 30 days of continuous heating, suggesting the segmental motion of the polymer was promoted by temperature. The high-temperature supercapacitor was constructed using DN ionogel as electrolyte (≈80 μm thickness) and porous reduced graphene oxide (GO) film (≈40 μm thickness) as electrode. At 0.1 A g^{-1}, the specific capacitance of DN ionogel supercapacitor increased from 31 to 88 F g^{-1} as the temperature increased from 30 to 180 °C. The durability and performance of high-temperature supercapacitor were evaluated in the temperature range of 30–180 °C at 1 A g^{-1}. There was no remarkable change in the initial specific capacitance for almost 1000 cycles (**Figure 29**a), and it was also not much varied under the temperature swing test from 180 to 30 °C (Figure 29b). The capacitance was measured at various bending angles to investigate the flexibility of the device, and almost 90% of the capacitance was retained at all angles (Figure 29c). The device exhibited an outstanding cycle stability of >100 000 charge–discharge cycles at 150 °C with the retention of ≈90% capacitance (Figure 29d). The self-discharge characteristics of the 2 h charged device were tested from 2 to 1 V, and the discharge time deteriorated from ≈50 to 21 h as the temperature increased from 30 to 180 °C (Figure 29e). The capacitance was not affected under normal (30 °C) and bending conditions (120 °C) for three continuous cycles (Figure 29f). The photographs for the real-time operation of supercapacitor at 30 and 120 °C under bending condition are shown Figure 29g. A thermometer was powered by the
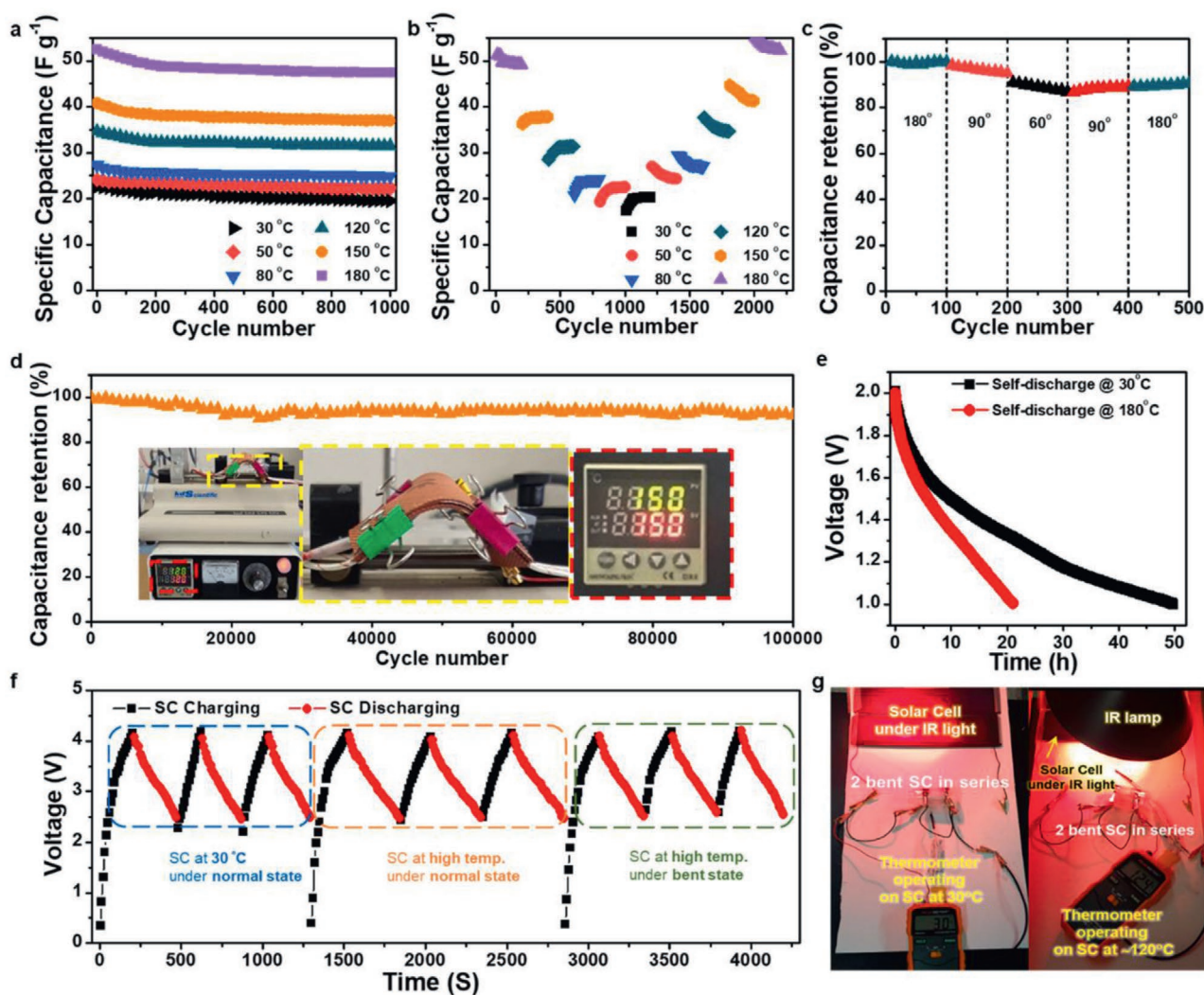
Figure 29. The durability and performance of high-temperature supercapacitor at 1 A g^{-1}: a) temperature-dependent cyclic stability, b) cyclic stability under temperature swing test from 180 to 30 °C, and the temperature was changed for every 200 cycles, c) stability for 500 cycles at various bending angles and 150 °C, d) long-term stability for 100 000 cycles at 150 °C, e) self-discharge characteristics of the 2 h charged device from 2 to 1 V, f) voltage profiles under normal (30 °C) and bending conditions (120 °C) for three continuous cycles, and g) photographs of the device operation at 30 and 120 °C with solar cells under bending condition.[179] Reproduced with permission.[179] Copyright 2019, Elsevier.

**ADVANCED
SCIENCE NEWS**
www.advancedsciencenews.com

**ADVANCED
ENERGY
MATERIALS**
www.advenergymat.de

supercapacitor during discharging at 120 °C. These kinds of flexible devices could be used for the solar energy harvesting and storage in the desert.

The unique mechanical durability, flexibility, and thermal stability of the supercapacitor were accredited to the cross-linking DN, interaction of polymer with IL, and thermally initiated ion transport mechanism.

5.2.2. Polymer Electrolyte

In a similar study, a super-thermostable and flexible polymer-composite electrolyte was engineered for developing a high-temperature supercapacitor.[180] The electrolyte was synthesized using PTFE (13 wt%), thermoplastic polyurethane (TPU, 13 wt%), 1-ethyl-3-methylimidazolium bis(trifluoromethylsulfonyl)imide (EMITFSI) IL (70 wt %), and fumed silica nanoparticles (FSN, 4 wt %). The high-temperature supercapacitor was fabricated by the polymer-composite electrolyte and 3D porous graphene aerogel electrode. The schematic of temperature responsive ionic transport mechanism and the cross-sectional SEM image of the supercapacitor are displayed in **Figure 30**. The hydrogen bonds between the IL and FSN were partially broken at high temperatures; this could decrease the viscosity of electrolyte and enhance the kinetic energy and ionic conductivity (Figure 30a).[181] The combination of mesopores and macropores in the graphene aerogels (Figure 30b) was advantageous for the well-organized ionic transport mechanism.

The electrochemical behavior of the supercapacitor was examined in the range of 25–200 °C (**Figure 31**). The capacitance of the device was calculated from the CV curves (Figure 31a), and the specific capacitance was increased with respect to temperature and scan rate (Figure 31b). The specific capacitance at 200 °C was around 18 times higher than that of room temperature. The charge–discharge curves at 1 A g^{-1} showed that the specific capacitance was increased with respect to the temperature (Figure 31c). The efficiency of the device with FSN-IL was around 1.9 times higher as compared to the same with bare IL (Figure 31d). The activation energy was obtained from the Arrhenius plots (Figure 31e), and it was determined as 19 kJ mol^{-1}. Ragone plots demonstrated that the gravimetric energy and power density of the supercapacitor were increased with respect

to temperature (Figure 31f). The energy density of the supercapacitor at room temperature and 200 °C were 63 and 1134 W h kg^{-1}, respectively, and this efficiency was superior when compared to other high-temperature supercapacitors.[182–186] The significant performance of the device was ascribed to the synergistic effect of IL activation and ionic transport through the interconnected pores at high temperatures.

The calculated ionic conductivities at various temperatures were fitted in the VFT equation (Equation (60)), and a linear relationship was observed

$$\sigma = \sigma_0 \exp\left(-\frac{B}{T - T_0}\right) \tag{60}$$

The diffusion coefficient of the ions and viscosity of the electrolyte were related by the Stokes–Einstein equation as follows
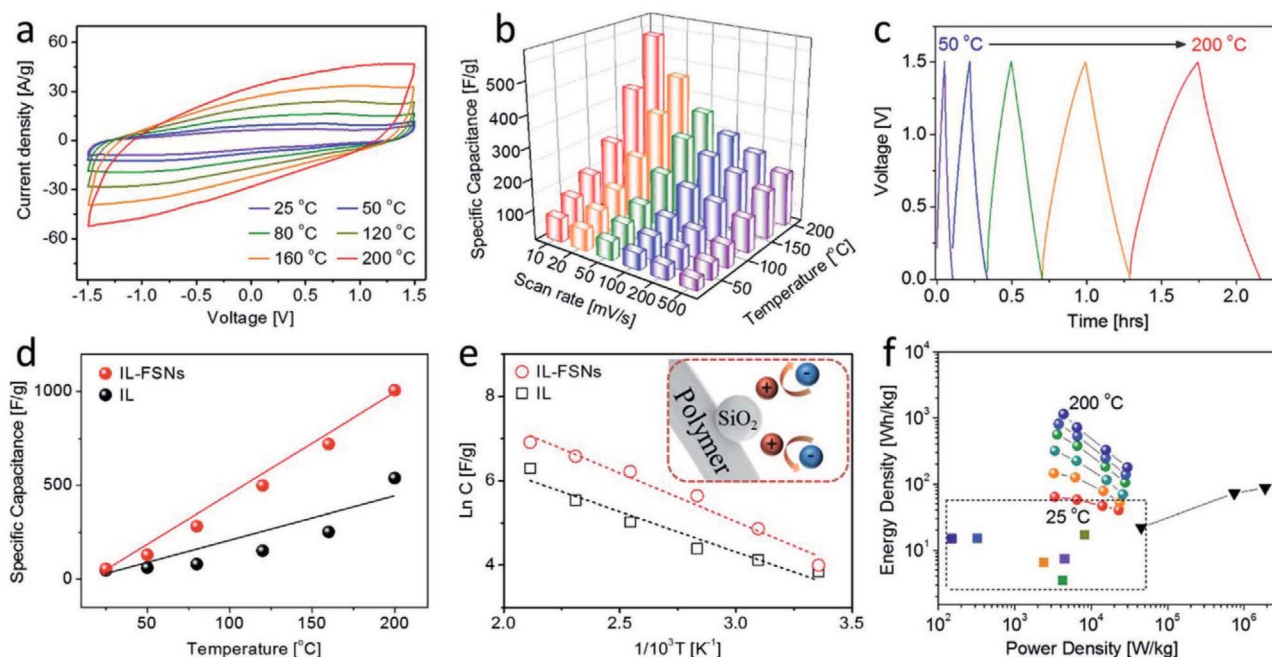
$$D = k_B T / 6\pi r\eta \tag{61}$$

where D, k_B, T, r, and η are the diffusion coefficient, Boltzmann constant, absolute temperature, ionic radius, and viscosity of the electrolyte, respectively. According to this equation, D could increase with respect to T, and therefore the high temperature could enable the diffusion of ions from the electrolyte to the porous electrode surface. The impedance measurements at 45° phase angle demonstrated that the diffusion-controlled capacitance was increased significantly compared to the kinetic-controlled capacitance with respect to temperature. The relaxation time (τ_0) of the device was also calculated to investigate the temperature responsive kinetics in detail (Equation (62))

$$\tau_0 = 1/f_0 \tag{62}$$

The results showed that τ_0 was reduced from 6.3 to 2.5 s as the temperature increased from 25 to 200 °C. This was ascribed to the increase of ionic mobility by the minimization of activation energy barriers and the breakage of hydrogen bonds at high temperature. The thermal stability of the supercapacitor was evaluated through the charge–discharge cycle measurements at 25 °C (at current density 0.5 A g^{-1}) and 200 °C (at current density 5 A g^{-1}). At 200 °C, the cyclic stability of the supercapacitor was outstanding with ≈90% of retention in capacitance after 10 000 cycles. The mechanical flexibility was investigated at various bending angles at 200 °C, and the results showed that the capacitance of the device was not influenced during the
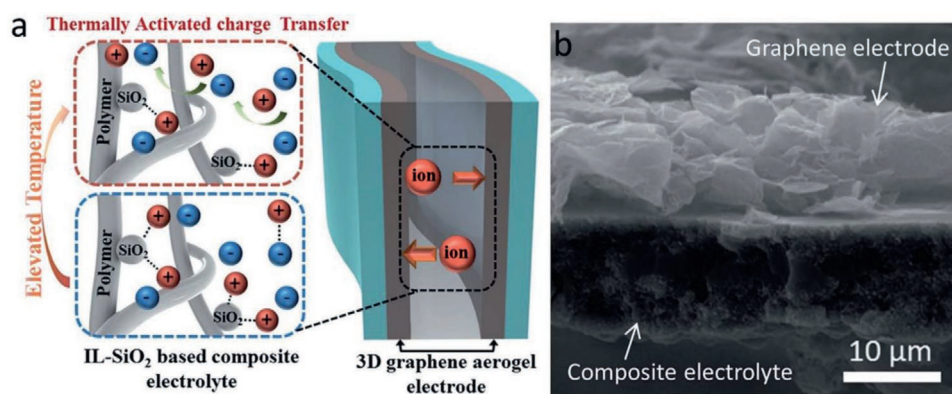
Figure 30. High-temperature supercapacitor with polymer-composite electrolyte and 3D graphene aerogel electrode: a) schematic of ion transport mechanism and b) cross-sectional FESEM image.[180] Reproduced with permission.[180] Copyright 2020, Royal Society of Chemistry.

**ADVANCED
SCIENCE NEWS**

www.advancedsciencenews.com

**ADVANCED
ENERGY
MATERIALS**

www.advenergymat.de

Figure 31. The electrochemical behavior of the supercapacitor in the range of 25–200 °C: a) CV curves at a scan rate of 100 mV s⁻¹, b) temperature-dependent specific capacitance at various scan rates, c) charge–discharge curves at a current density of 1 A g⁻¹, d) specific capacitance of IL and IL-FSNs, e) Arrhenius plots of specific capacitance and kinetics of ion transport, and f) Ragone plots at various current densities (1, 2, 5, and 10 A g⁻¹).[180] Reproduced with permission.[180] Copyright 2020, Royal Society of Chemistry.

bending and recovery stages (≈89% of retention in capacitance after 5000 cycles). The exceptional electrochemical behavior of polymer-composite electrolyte/3D porous graphene aerogel supercapacitor was ascribed to the superior migration rate of ions, kinetic energy, diffusion of ions at the porous electrode, flexibility, and thermal stability.

A porous polybenzimidazole (PBI) and 1-(3-trimethoxysilylpropyl)-3-methylimidazolium chloride (TMSPMI) IL electrolyte was utilized for the fabrication of flexible and high-temperature

supercapacitor.[187] The schematic representation of the supercapacitor is shown in **Figure 32**.

The electrode was synthesized on a nickel foam using carbon black and AC. The polymer composite electrolyte was fabricated with various mass percentages of TMSPMI such as 0%, 5%, 10%, 15%, and 20%.[188] Cross-sectional SEM images of the PBI with various TMSPMI contents are shown in **Figure 33**.

The porosity percentages of PBI-TMSPMI with 0, 5, 10, 15, and 20 wt% were 59.39%, 52.28%, 41.48%, 40.08%, and 38.1%,
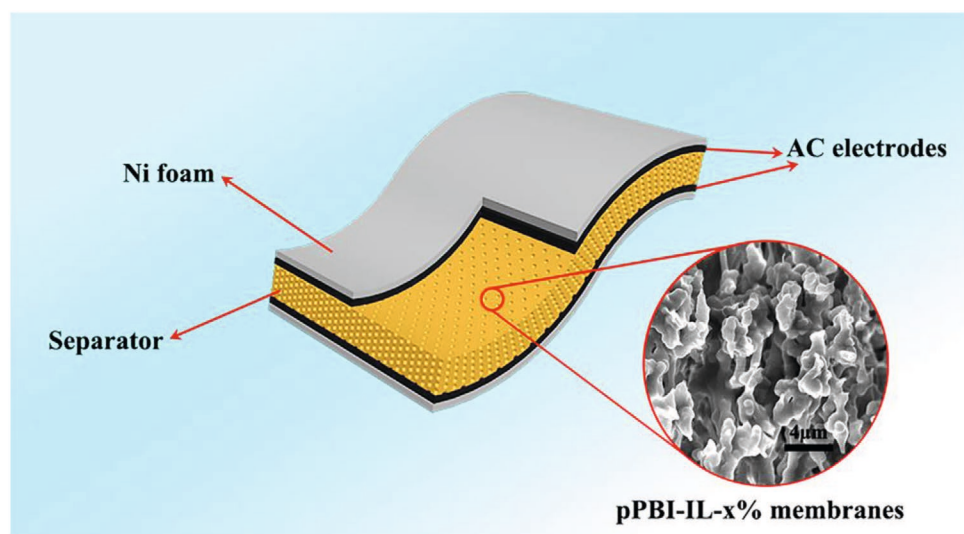
Figure 32. Schematic representation of supercapacitor with PBI-TMSPMI (IL) electrolyte and AC electrode.[187] Reproduced with permission.[187] Copyright 2019, American Chemical Society.

ADVANCED
SCIENCE NEWS
www.advancedsciencenews.com

ADVANCED
ENERGY
MATERIALS
www.advenergymat.de
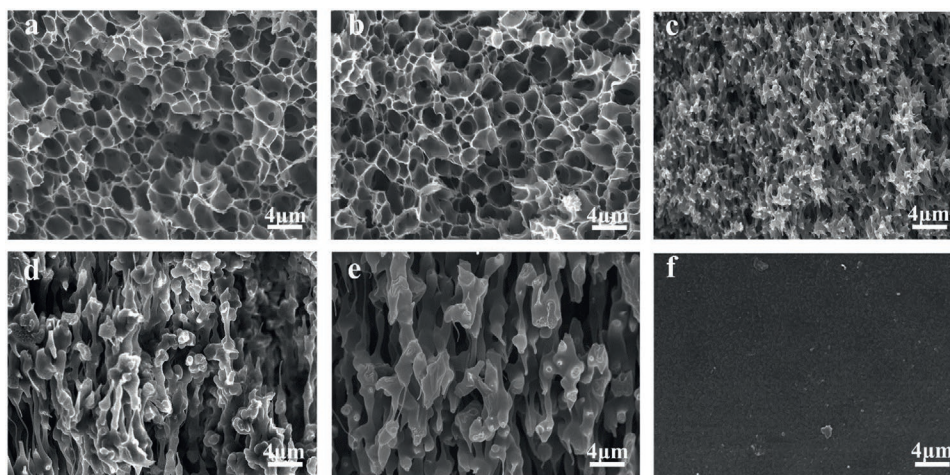
Figure 33. Cross-sectional SEM images of a) bare PBI, b) PBI with 5% TMSPMI, c) PBI with 10% TMSPMI, d) PBI with 15% TMSPMI, e) PBI with 20% TMSPMI, and f) surface SEM of PBI with 15% TMSPMI.[187] Reproduced with permission.[187] Copyright 2019, American Chemical Society.

respectively. The porosity of polymer composite electrolyte decreased with the increase of TMSPMI, suggesting the pores were blocked by the silica nanoparticles and the formation of Si–O–Si network at high content of IL[189,190] (Figure 33a–e). SEM morphology of PBI-TMSPMI 15 wt% showed that the surface of the electrolyte was smooth and uniform (Figure 33f). Stress–strain measurements of polymer composite electrolyte were revealed that the decrease of tensile strength and increase of Young's modulus as the content of TMSPMI was exceeded 5%. This was accredited to the breakage of hydrogen bonds between the monomers in PBI at high TMSPMI content. TGA results also showed that the thermal stability of the polymer film was affected by the high TMSPMI content. However, the proton conductivity of the electrolyte was increased with respect to TMSPMI content up to 15 wt%. The proton conductivity of PBI-TMSPMI 15 wt % at 170 °C was 0.103 S cm^{-1}, which was around two times higher than that of 110 °C. The high ionic conductivity was accredited to the increase of proton carriers, and the porous morphology for ionic transport. The specific capacitance of supercapacitor with PBI-TMSPMI 15 wt% electrolyte was evaluated at various temperatures (such as 30, 60, 90, 120, 150 °C) and at a scan rate of 50 mV s^{-1}. The specific capacitance was increased with respect to temperature up to 120 °C, and the value obtained at 120 °C (85.5 F g^{-1}) was around three times higher than the same at 30 °C. This was ascribed to the increase of ionic transport, and expansion of contact area between the electrolyte and electrode at high temperatures. The flexibility results suggested that the capacitance of the device was not significantly affected by the bending angles (60° and 120°).

5.2.3. Hydrogels

Hydrogels are one of the ideal SEs to fabricate the flexible and thin supercapacitors. Nevertheless, the conventional hydrogel electrolytes consist of excess water molecules, which could hamper the utilization of energy storage at sub-zero and elevated temperatures.[164] Moreover, the ionic conductivity of conventional hydrogel electrolytes is not adequate for the

utilization of energy storage devices in harsh weather conditions. The water molecules are not stable at the high temperature.[164] The strong hydrogen bonds within the water molecules influence the freezing point[168] of hydrogels. Therefore, various additives such as GO, montmorillonite (MMT), PAA, PVA, PAM, and polyaniline (PANI) have been used with hydrogel electrolytes to increase the thermal stability and to upgrade the ionic conductivity. The solvents such as dimethyl sulfoxide (DMSO), ethylene glycol, and sulfuric acid (H$_2$SO$_4$) have also been added with hydrogels to influence the hydrogen bonds and reduce the freezing point.

The interstitial spaces of elastic cross-linked hydrated polymers are filled with a high content of water. The polymer network could adsorb and trap a significant amount of water (around 2000 times of its own weight).[110] The amount of water content in the hydrogel may vary with respect to nature of polymer and solvents. The water content directly influences the physicochemical properties of the hydrogel and the hydrogel electrolyte increases the ionic conductivity. However, the polymer scaffold may be dissolved, as the water content is too high.[110]

A cross-linked PAM hydrogel electrolyte was designed to improve the cyclic stability, flexibility, and to extend the temperature window (in the range of −30 to 100 °C) of the supercapacitor.[167] The device could be utilized for antifreezing and antiheating applications. The hydrogel electrolyte was fabricated through the cross-linking of PAM and methacrylated GO (MGO) in the presence of ethylene glycol–water solvent. A flexible supercapacitor was made by the hydrogel electrolyte and MWCNTs-PANI films. The mechanical and thermal behavior of the PAM–MGO was superior to the pure PAM. The flexibility and compressibility of the hydrogel were enhanced through the interconnected cross-linking network and hydrogen bonds between the PAM and MGO. The ionic conductivity of PAM–MGO was predominant (12.7 S m^{-1}) when compared to the recently reported PAM hydrogel electrolytes.[191–194] The unique mechanical features of the PAM-MGO were not influenced at very low (−30 °C) and high temperatures (100 °C). This was ascribed to the porous morphology of

the hydrogel and the existence of its strong interaction with water molecules. The specific capacitance of the device at –30 and 100 °C were 141.7 and 157.2 F g^{-1}, respectively, and these values were acceptable, compared to the same at room temperature. The original specific capacitance was well maintained as the supercapacitor was compressed to 80%, and there were no significant variations in the CV curves after 100 compression/release cycles. In addition to that, the capacitance of the device at –30 °C was not affected at various bending angles such as 45, 90, and 180°, testifying the exceptional flexibility and stability of the device. After 8000 cycles, 93.3% capacitance was retained at –30 °C and current density of 2 A g^{-1}. Under 100 °C, 76.5% capacitance was retained after 4000 cycles, and the decrease in efficacy was ascribed to unavoidable solvent loss at high temperatures. Two such supercapacitors connected in series could drive a commercial calculator as they are placed at ice water and hot plate. Three supercapacitors connected in series could power an LED lamp. Moreover, the calculator and LED lamp functions of the supercapacitor were also not affected under a load of 500 g.

In a similar study, a novel crystal-type polymer hydrogel (A_xD_y-NaAc$_z$) was engineered through the dissolution–crystallization technique for temperature-responsive supercapacitor in the range of –40 to 80 °C.[168] The polymer hydrogel was synthesized using water, sodium acetate trihydrate (NaAc·3H$_2$O), 15 wt% of acrylamide monomer (A), and 3-dimethyl(methacryloyloxyethyl)ammonium propane sulfonate (D), zwitterion monomer to enhance the ionic conductivity. AC was used as the electrode to fabricate the supercapacitor with A_xD_y-NaAc$_z$ polymer hydrogel electrolyte and ≈1 µL of water was used to wet the electrolyte surface. The precursor models (**Figure 34**a), precursor solution (Figure 34b), hydrogel formation (Figure 34c), crystallization process (Figure 34d,e), SEM image (Figure 34f), compression test (Figure 34g), and exothermic/endothermic mechanism (Figure 34h) during the phase transition are schematically displayed in Figure 34. SEM results showed that needle-like NaAc crystals were aligned in parallel in the hydrogel with a diameter of ≈2–3 µm, confirming the formation of crystal-type polymer hydrogel.

The compressibility of the hydrogel was enhanced from 0.8 to 61.4 MPa at 95% strain as the content of NaAc increased from 0.1 to 1.4 mass%. The molecular simulation studies demonstrated that the noncovalent interactions (hydrogen bond and electrostatic interaction) between NaAc and polymer network could enhance the mechanical strength. The toughness of the crystal-type hydrogel was excellent, and the shape was not even altered by 5 kg weight (Figure 34g). The outstanding mechanical characteristics of the polymer hydrogel were
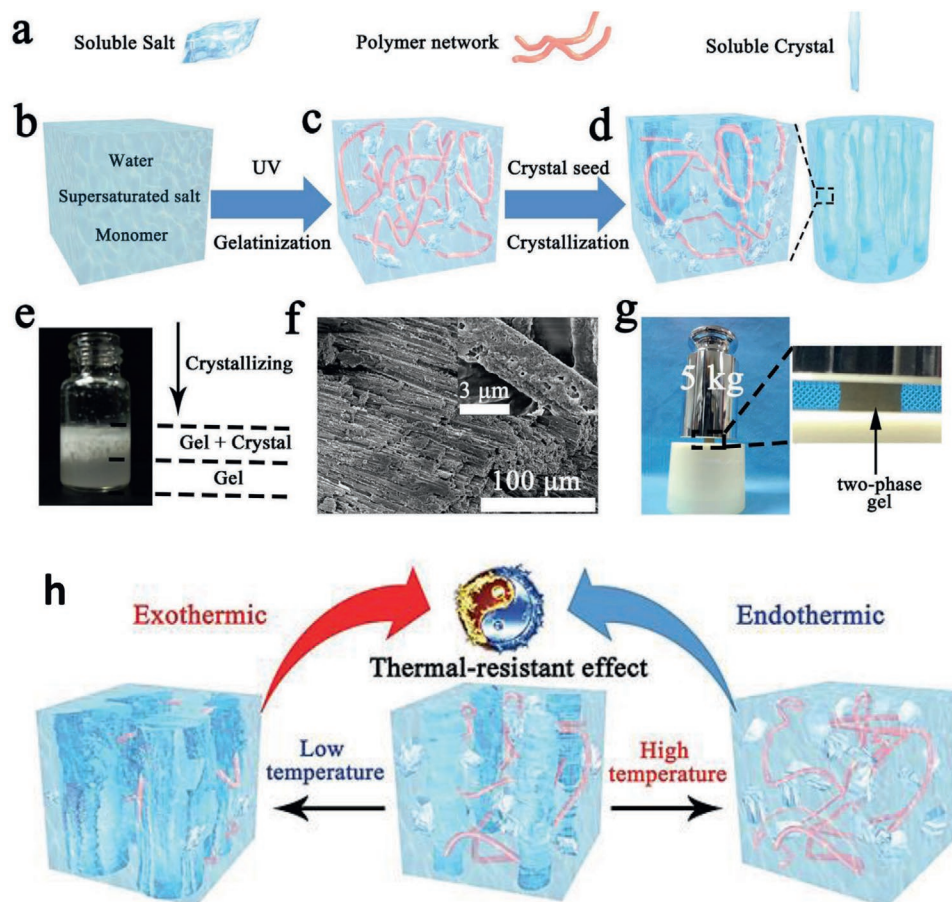
Figure 34. Crystal-type polymer hydrogel: a) precursor models, b–d) schematic of synthesis, e) photograph of crystallization process, f) SEM image, g) photograph of the compression test of 14 mm hydrogel under 5 kg, and h) schematic of thermal resistance mechanism during the phase transition of NaAc.[168] Reproduced with permission.[168] Copyright 2019, Wiley-VCH.

**ADVANCED
SCIENCE NEWS**

www.advancedsciencenews.com

**ADVANCED
ENERGY
MATERIALS**

www.advenergymat.de

accredited to the synergism of durable NaAc crystals and ductile polymer gel network. The ionic conductivity of hydrogel was decreased as the content of NaAc increased, demonstrating the free ions migration in the electrolyte was suppressed at high NaAc concentration. The liquid–solid phase transition (flexible and rigid characteristics) of the hydrogel was governed through the dissolution and crystallization of NaAc with respect to temperature. The dissolution and crystallization process of NaAc at high and low temperature was proceeded through endothermic and exothermic mechanisms, respectively. The unique features of the hydrogel could support its fabrication through the convenient 3D printing technology. The charge–discharge curves of supercapacitor with A_xD_y-$NaAc_z$ electrolyte in the range of –40 to 80 °C are shown in **Figure 35**a. The specific capacitance at –40, 20, and 80 °C were 129.7, 175.9, and 329.7 F g^{-1}, respectively (Figure 35b). The decrease of specific capacitance at low temperatures was ascribed to the poor ionic conductivity and unavailability of ions. At high temperatures, the ionic conductivity was increased through the dissolution and ionization of aligned NaAc crystals, suggesting an increase of specific capacitance (Figure 35c).[195,196] The capacity retention percentage after 10 000 cycles at –20, 20, and 60 °C were 75.3, 86.6, and 92.7%, respectively. The thermal resistance of A_0D_{15}-$NaAc_{1.2}$ electrolyte was tested under liquid nitrogen (–196 °C) and flame test (>200 °C). The electrolyte was able to power an LED lamp under extreme low and high temperatures, demonstrating the thermal stability of the crystal-type polymer hydrogel (Figure 35d). As shown in Figure 35e, the thermal, mechanical, and electrochemical performance of crystal-type polymer hydrogel electrolyte is superior to pure polymer and hydrogel electrolytes.[67,197,198]

In a recent study, a flexible, light-weight, antifreezing, and thermally stable supercapacitor was designed using MMT/PVA hydrogel electrolyte (molar ratio of MMT/PVA was 1:9).[164] The capacitance and cyclic stability of the supercapacitor was excellent in the range of –50 to 90 °C. 1:1 ratio of 2 M H_2SO_4-DMSO/H_2O was used as the solvent to produce the hydrogel. The supercapacitor was fabricated through one layer of MMT/PVA hydrogel electrolyte and two layers of graphene electrodes. The lamellar structure with porous morphology of MMT could enhance the thermal stability, and also promote the ionic conductivity via the establishment of rapid conducting channels for ion transport.[199,200] H_2SO_4-DMSO/H_2O could support the electrochemical performance of supercapacitor with appropriate ionic conductivity at extreme low temperatures (–50 °C). The freezing point of this solvent mixture was –60.4 °C, which was much lower than that of pure water and DMSO. The required mechanical stability and flexibility of the device could be facilitated by the PVA.[201,202] Stress–strain studies revealed that the tensile modulus of MMT/PVA was higher (14.3 MPa with 22.6% breakage elongation) than pure PVA (9.58 MPa with 13.8% breakage elongation), and the enhanced mechanical features was ascribed to the plasticization effect of MMT.[203] TGA results suggested that MMT/PVA was thermally stable in the range of 50–300 °C, indicating the strong the hydrogen bonding interactions between MMT and PVA.[204] In addition to that, the flame resistance feature of MMT/PVA was also better than pure PVA. The flexible and temperature-responsive features of supercapacitor are displayed in **Figure 36**. The charge–discharge curves

of the device were almost similar under various stretching, bending, and twisting conditions (Figure 36a). The charge–discharge characteristics were not influenced by the bending angles (Figure 36b). Almost 91% of specific capacitance was retained after 1000 bending cycles (Figure 36c), demonstrating the excellent flexibility of the device. As shown in Figure 36d, the ionic conductivity of the device was increased with respect to temperature from –50 °C (0.17 × 10^{-4} S cm^{-1}) to 90 °C (0.76 × 10^{-4} S cm^{-1}). The specific capacitance of the device was increased as the temperature increased from –50 to 30 °C (Figure 36e,f). The schematic of antifreezing and thermal stability mechanism of hydrogel electrolyte is shown in Figure 36g. The decrease of specific capacitance after 30 °C was accredited to the segmental relaxation of PVA at high temperature. The glass transition temperature (T_g) and viscous flow temperature (T_f) of MMT/PVA were 71 and 182 °C, respectively, suggesting the supercapacitor could be operated in the range of 90 °C without any collapse. MMT/PVA hydrogel is a thin and low-cost material (USD 0.29 g^{-1}), and it could be utilized as a promising electrolyte for commercialization.

The key findings of recent SEs for the high-temperature stable electrochemical performance of batteries and supercapacitors are summarized in **Tables 1** and **2**. The efficiency of PVDF-based SEs was compared with the commercial membranes. The recent findings showed that most of the thermally stable SEs have been designed using the porous fluoropolymers. Most commonly, Li salts with ceramic fillers and polymers have been used as SEs for the high-temperature applications of batteries. In the case of flexible supercapacitors, polymers with additives such as ILs, SiO_2, TiO_2, and GO have been utilized as SEs for the high-temperature applications. Polymeric hydrogels have been used for the antifreezing applications of supercapacitors. PVDF with high-temperature stable ceramics is the state-of-the-art SE for the batteries. PTFE with metal oxide additives or 2D fillers is the state-of-the-art SE for the supercapacitors.

6. Challenges and Prospects

The utilization of carbon-free energy sources for transportation is one of the global trends in recent times to mitigate the impact of global warming by fossil fuels.[57,205,206] U.S. Energy Information Administration predicted that the sales of gasoline engine vehicles would be reduced in the next few decades.[207] Because of this, the global demand of EVs manufacturing has increased significantly in the last 5 years.[1,208,209] Most of the famous car manufacturing companies in the USA, Japan, and China are planning to increase their EVs production by the year 2050. However, recent accidents in the EVs clearly demonstrate that more attention should be given to the thermal safety aspects. Therefore, studies should focus on the thermal safety features of electrochemical devices to accomplish this goal.

6.1. Electrolytes

The exploitation of SEs is an important option to ease the risk of fires or explosions in the EVs. All the flammable organic carbonate LEs should be replaced by the thermally stable SEs to mitigate the TR at high temperatures. Nevertheless,
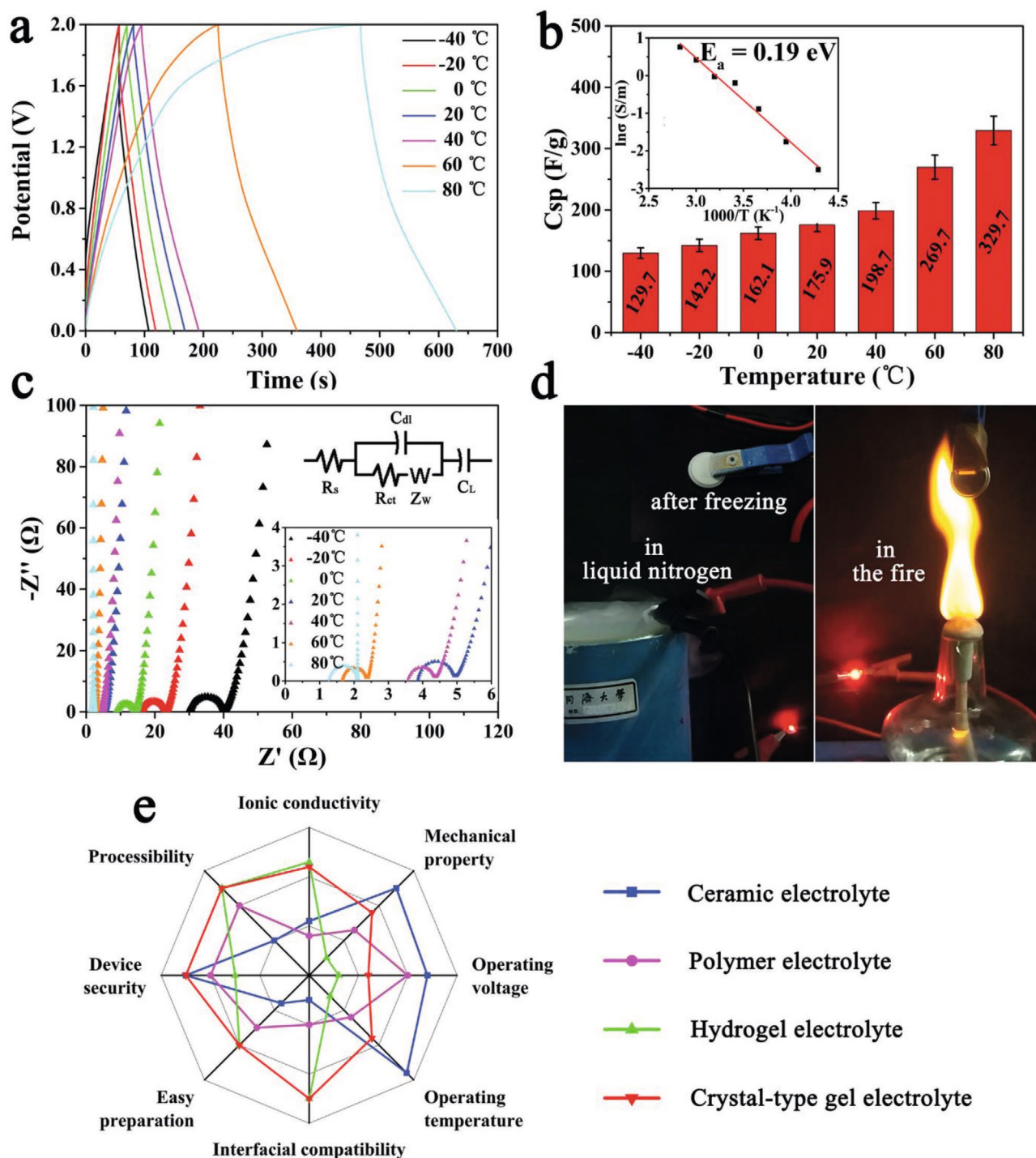
Figure 35. Performance of supercapacitor with crystal-type polymer hydrogel electrolyte (A_0D_{15}-NaAc$_{1.2}$) in the range of –40 to 80 °C: a) charge–discharge curves at 1 A g^{-1}, b) specific capacitance (inset: Arrhenius plot), c) Nyquist plots, d) photographs of placing the electrolyte in liquid nitrogen and flame, and e) radar plots for the performance of various electrolytes.[168] Reproduced with permission.[168] Copyright 2019, Wiley-VCH.

the efficiency of most of the SEs including CPE, ionogel, and hydrogel is not higher, compared to that of LEs. It could be resolved through engineering of appropriate interfaces between the solid phases and electrodes to amplify the ionic conductivity. Advance theories and reliable protocols should be framed to examine the thermal stability of SEs. Progressive

characterization tools should be established for the deep understanding on the fundamentals and mechanisms of internal chemical reactions in an electrochemical device. In most of the cases, a small quantity of IL or carbonate solvent was utilized to wet the SEs surface, and the safety features of this aspect could also be examined thoroughly.

ADVANCED
SCIENCE NEWS
www.advancedsciencenews.com

ADVANCED
ENERGY
MATERIALS
www.advenergymat.de
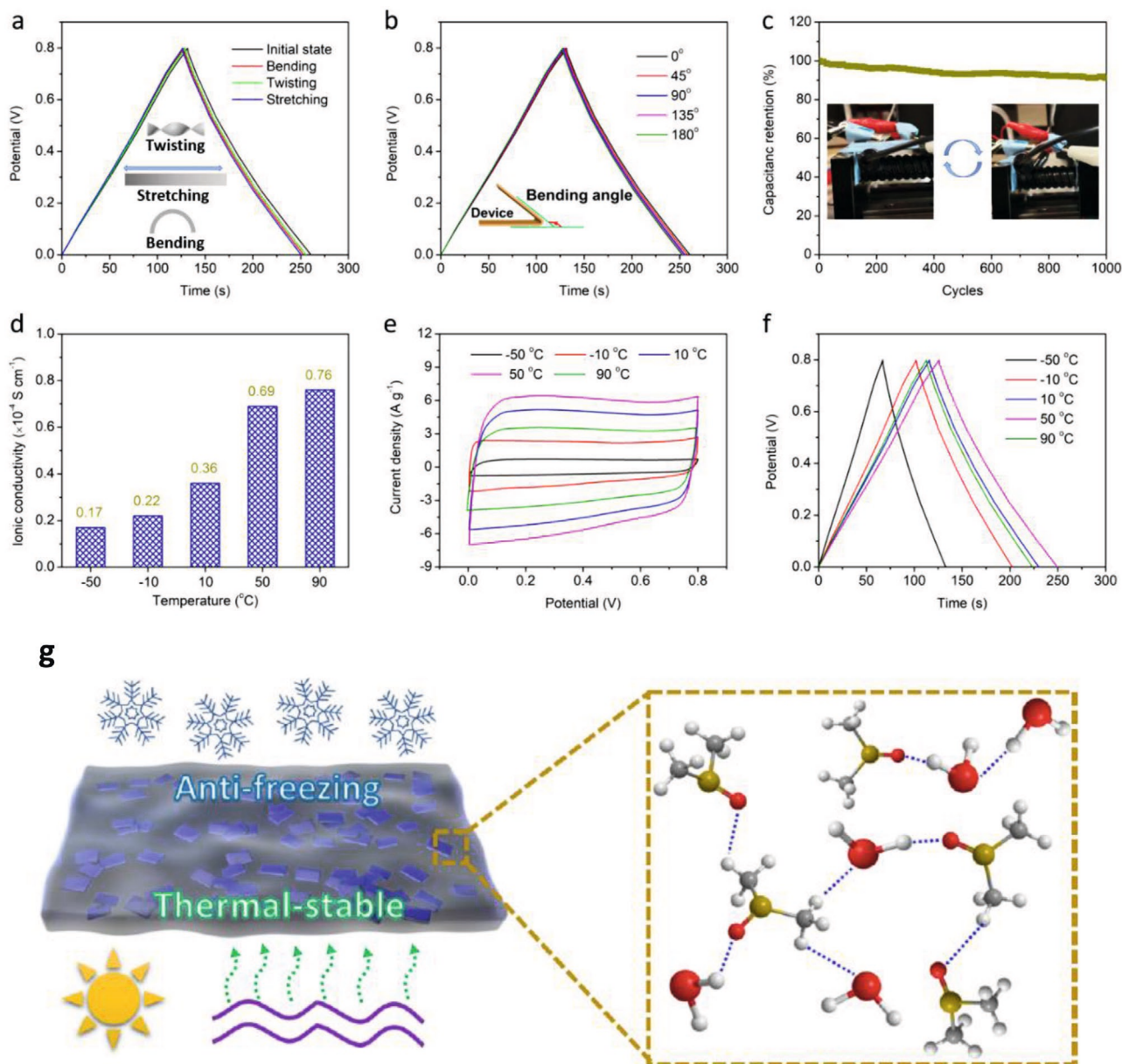
Figure 36. Temperature-responsive supercapacitor with MMT/PVA hydrogel electrolyte and graphene electrode: a) charge–discharge curves at bending, twisting, and stretching positions; b) charge–discharge curves at various bending angles; c) specific capacitance during 1000 bending cycles; d) ionic conductivity; e) CV curves; f) charge–discharge curves at 1 A g^{-1}; and g) schematic of antifreezing and thermal stable hydrogel electrolyte with hydrogen bonding interactions.[164] Reproduced with permission.[164] Copyright 2020, American Chemical Society.

The existing studies demonstrated that the engineering of high-temperature stable SEs is one of the current trends for the energy storage applications. Significant amount of research efforts are needed in the future to design the thermally stable PVDF and PTFE-based SEs with 2D inorganic additives for the batteries and supercapacitors. In the recent years, the hybrid energy storage devices (battery–supercapacitor) have been studied using a common electrolyte.[210–212] However, there are no detailed studies on the high-temperature applications of hybrid energy storage devices with SEs. Polymeric hydrogels would be one of ideal SEs for the application of hybrid energy storage devices for antifreezing and high-temperature

applications. Therefore, comprehensive studies are needed in the future to evaluate the thermal safety features of hybrid energy storage devices with a common SE.

6.2. Interfaces

TR or the abuse conditions of ISC highly rely on the surface chemical reactions between the electrode and electrolyte. Consequently, fundamental investigations on the electrode–electrolyte interfacial (such as anode–SE, cathode–SE, and solid–solid interfaces)/interphasial (such as electronic property,

Table 1. A summary of high-temperature stable electrochemical performance of SEs for batteries.

SE	Operating temperature [°C]	Ionic conductivity	Current density [C]	Cell configuration	Capacity [mAh g^{-1}]	Capacity retention	Ref.
PVDF/Al$_2$O$_3$ membrane	150	0.82 mS cm^{-1}	0.2	Li//LiFePO$_4$	≈154	≈100% after 100 cycles	[161]
Pyrolux membrane with LiBOB	120	5.76 mS cm^{-1}	0.33	Li//graphite	340	Above 90% after 100 cycles	[163]
PVDF/LLZNO/ LiClO$_4$	120	–	1	Li//LiFePO$_4$	150.1	≈100% after 100 cycles at 80 °C	[51]
PEO/2D vermiculite clay sheets/LiTFSI	100	3.1 × 10^{-3} S cm^{-1}	0.5	Li//LiFePO$_4$	152 at 60 °C	–	[165]
PEO/LLZTO/LiTFSI	90	–	0.2	3D Li//LiFePO$_4$	135	≈99% after 200 cycles	[174]
PEGMA/PFE	150	0.5 × 10^{-4} S cm^{-1} at 60 °C	0.5	Li//LiFePO$_4$	145	≈90% after 200 cycles at 100 °C	[166]

composition, and distribution of materials) phenomena should be one of the key areas for the researchers to explore. Atomic-scale characterization techniques are essential to investigate the temperature-responsive ionic conductivity and interfacial chemistry. The ionic conductivity across the interfaces and other interfacial changes should be investigated by advanced in situ techniques such as X-ray photoelectron spectroscopy, in situ TEM or SEM, in situ Raman, and time-of-flight secondary ion mass spectroscopy. XCT should be used to examine the porosity and tortuosity of SE interfaces in a 3D scale. Using of rigid SEs cause large interfacial resistance and this could be resolved through the flexible SEs, and the optimization of interfacial kinetics between the electrode and electrolyte. The interfacial resistance is higher in the solid-state batteries owing to the poor physical contact between the electrode and SE. It

could be further terrible during the cycling process. In a very recent study, an argyrodite-type sulfide SE has been examined by Samsung Electronics to suppress the unfavorable Li dendrite growth in a solid-state Li metal battery.[213] The influence of temperature on the voltage profiles of the prototype pouch cell was tested in the range of –10 to 60 °C, and the discharge capacity of the cell was considerably affected by the large interfacial resistance at low temperatures. Interlayer addition and interface coating are the successful strategies to address the interfacial issues and improve the cyclic stability. The utilization of 3D Li anode is another ideal way to minimize the interfacial resistance. The interfaces should also be optimized through the in situ or ex situ passivation layers. Neutron depth profiling is an advanced tool to examine the Li distribution at the interfaces.

Table 2. A summary of high-temperature stable electrochemical performance of SEs for supercapacitors.

SE	Operating temperature [°C]	Ionic conductivity	Current density [A g^{-1}]	Electrodes	Specific capacitance [F g^{-1}]	Capacity retention (stability)	Ref.
TiO$_2$/clay nanosheets/DBMIT	200	22.1 mS cm^{-1}	10	Carbon nanocage	167	–	[162]
C-PVA/HEMA/MBAA/EMIMBF$_4$	180	118.6 mS cm^{-1}	0.1	Reduced GO	88	≈90% after 100 000 cycles at 150 °C and 2 A g^{-1}	[179]
PTFE/TFU/EMITFSI/FSN	200	–	1	3D graphene aerogel	1007	≈90% after 10 000 cycles at 5 A g^{-1}	[180]
PBI/TMSPMI	120	≈0.065 S cm^{-1}	1	AC	85.5	91% after 10 000 cycles	[187]
PAM/MGO	100	≈10 S m^{-1}	0.5	PANI on MWCNT	157.2	76.5% after 4000 cycles at 2 A g^{-1}	[167]
	–30	≈3.8 S m^{-1}	0.5		141.7	93.3% after 8000 cycles at 2 A g^{-1}	
A$_x$D$_y$-NaAc$_z$	80	2.13 S m^{-1}	1	AC	329.7	92.7% at 60 °C after 10 000 cycles	[168]
	–40	0.08 S m^{-1}			129.7	75.3% at –20 °C after 10 000 cycles	
MMT/PVA	90	0.76 × 10^{-4} S cm^{-1}	1	Graphene	≈140	–	[164]
	–50	0.17 × 10^{-4} S cm^{-1}			≈80	–	

ADVANCED
SCIENCE NEWS

www.advancedsciencenews.com

ADVANCED
ENERGY
MATERIALS

www.advenergymat.de

6.3. Li Salts

One of the recent analysis of Bloomberg New Energy Finance projected that the requirement for Li salts would increase 1500 times by the year 2030, and therefore severe attention should be given in this regard to address our future energy demands at an affordable cost. Moreover, the availability of Li ores is not sufficient, compared to other elements in the earth. In most of the SEs, expensive Li salts have been used as an additive, and this could be replaced by other cost-effective materials without compromising the ionic conductivity.

6.4. Commercial Cells

Very limited studies have been conducted on prismatic cells with SEs, which are commonly used in EVs and hybrid EVs. Hence, various investigations should be carried out further on commercial pouch, cylindrical, and prismatic cells under all the abuse conditions. Similarly, thermal stability investigations on SEs should be extended to the commercial supercapacitors.

6.5. Fabrication

The existing techniques for the synthesis of most SEs are not very feasible for the industrial process. Highly scalable synthesis techniques for SEs should be developed to address the technical challenges for commercialization. 3D printing technologies are one of the easiest approaches to address this challenge; however, more studies are required in the future to design the thermally stable, robust, and flexible SEs.

6.6. Intrinsic Features

Extensive investigations are required on the impact of defects on bulk and grain boundary ionic conductivity. Thermal stability of SEs should be studied at various ramp rates to observe the specific thermal decomposition temperature of materials. The mechanism of interstitial and vacancy mediated ionic conductivity of SEs should be examined with respect to the temperature. SEs with a high concentration of ceramics or inorganic salts would be favorable to extend the thermal stability of batteries.

6.7. Kinetics and Models

The existing studies on the computational modeling to engineer thermally stable SE materials are not much satisfactory. Ab initio molecular dynamics could be used to study the kinetics of interfacial reactions. Precise thermodynamic and kinetic models should be developed to lead the safety features of batteries and supercapacitors at molecular and system level. The precise location of the hot spots could be identified with the help of appropriate kinetic and thermal models. There are no major studies on the thermodynamics of SEs for batteries and supercapacitors. Comprehensive kinetic and thermodynamic

studies are essential to explore the mechanism of electrochemical abuse condition by considering all the potential chemical reactions in the device. The intrinsic characteristics such as temperature distribution and pressure fluctuations of electrochemical devices should be examined through the operando analysis techniques. It would be helpful for the engineers to design the electrochemical devices with more safety features. Various techno-economic models should be developed to explore the TR of hybrid electrical energy storage by considering supercapacitors and batteries.

6.8. Innovative Materials

In addition to the LEs, highly charged lithiated anode materials could also trigger the ISC and fire explosion. This may be nullified via the addition of fire-retardant materials to the anode surface without affecting its performance. Samsung Electronics introduced a silver–carbon composite anode to replace the Li anode and to avoid the destruction of SEs. Toyota already guaranteed to release their prototype EV with a solid-state battery technology during the Tokyo Olympics 2020 and it may be rescheduled due to the global pandemic situation. Toyota is also planning with Panasonic to manufacture solid-state batteries with a sulfur-based SE. They have planned to produce limited quantities of the solid-state battery by the year 2025. Attention should be given on the TR mechanism and abuse conditions of all these devices at high temperatures.

6.9. Strategies

Various TR mitigation strategies should be framed to reduce, eliminate, or warn of the early stage of an abuse condition at high temperatures. TR safety testing guidelines for electrochemical devices should be refined by duplicating all the abuse conditions such as thermal, mechanical, electrical, and electrochemical. All the evolving new chemistries for batteries and supercapacitors must overwhelm all kinds of abuse conditions to ensure the long-term stability, safety, and to avoid the ISC.

6.10. Regulations

To overcome the worst-case scenario, the devices should be equipped with an accurate and early warning sensor to rescue the passengers or occupants before the fire explosion. Moreover, all kinds of new electrochemical devices should not cause any fire or explosion during the TR tests for at least 5–10 min to rescue the passengers and driver from the EVs. Research is progressing on the integration of multiarray sensors into the battery cells to communicate the accurate TR condition. Online safety monitoring tools with voltage, temperature, and gas leakage warnings would also be advantageous for an electrochemical device. Most significantly, the thermally stable and cost-effective materials including electrodes, electrolytes, and separators should be established to ensure the EVs sales with an affordable price for a sustainable society with a similar level of comfort like conventional vehicles. It is also obvious that the

pandemic situations have a massive impact on the crude oil and automotive industry and open up new opportunities for the materials scientists and engineers to develop thermally stable electrochemical devices in the EVs market.

7. Summary

Comprehensive data on the utilization of SEs for the high-temperature stable batteries and supercapacitors have been reviewed in this study. Recent advances of most significant SEs such as CPEs, ionogels, and hydrogels for the batteries and supercapacitors have been comprehensively reviewed. Details on the TR mechanism, ionic transport phenomena, kinetics, and thermal models have also been discussed. CPEs could be used to operate the batteries in the temperature range of 80–200 °C. Hydrogels and ionogels could be employed to operate the supercapacitors at sub-zero (up to −50 °C) and elevated temperatures (till 200 °C), respectively.

The TR mechanism of an electrochemical device is commonly activated through various abuse conditions such as electrochemical, mechanical, thermal, and electrical conditions. Electrochemical abuse condition is considered as most significant compared to other abuse conditions. ISC is the most typical factor for fire explosion and there are three levels of ISC, such as I, II and II, based on the heat generation in the device.

The high-temperature ionic conductivity and voltage safety window of SEs are superior as compared to LEs. The ionic transport mechanism of SEs ensues the Arrhenius and VFT equations at low and high temperatures, respectively. Ionic conductivity of SEs was influenced through the grain boundaries, interfaces, interstices, vacancies, topology, and other physiochemical properties. Ionic conductivity mostly relied on the intrinsic interfaces as compared to the extrinsic interfaces. Ionic conductivity of CPEs could be further enhanced through the utilization of block copolymers and nanofillers. Time-domain NMR and AC conductivity spectroscopy were used to study the ion dynamics of SEs. The interfacial contact between the electrodes and electrolyte could be improved through the multilayer CPEs, and the addition of small amount of IL to wet the surface.

DSC and ARC analysis was used to examine the TR mechanism in batteries and supercapacitors. The main features, such as heat release condition, ISC, vent/overcharge/TR propagation behavior, and nail penetration, were investigated by various TR kinetic models. In most of the studies, the degradation of SEI was modeled by the Arrhenius equation. Models such as 1D thermal–electrochemical model and multiscale and multiphysics model were used to study the kinetics of TR. TR kinetic models were also employed to explore the key parameters of supercapacitors such as conduction heat transfer, thermal boundary conditions, and convection heat transfer coefficient.

The thermal stability of SEs and devices could be investigated in a hot air oven, hot plate, weathering chamber, and TGA at various temperatures. The surface porosity of SEs was more advantageous for the well-organized ionic transport mechanism. Direct casting, PI, and 3D printing were the recent technologies to fabricate the CPEs. Thermal stability, mechanical durability, flexibility, and electrochemical performance of CPEs were enhanced through the hierarchical nanoporous surface morphology, incorporation of 2D nanosheets, and the utilization of 3D scaffolds. Li dendrite growth and shrinkage of CPEs could be suppressed via more ceramics loading, using of high tensile strength polymers, and the 3D metal anode.

Thermal stability, tensile strength, flexibility, and electrochemical performance of aligned ionogels SEs were superior, compared to that of nonaligned ionogels SEs. Thermal stability of DN ionogels SEs was also higher than with the PIN ionogels. The ionic conductivity and specific capacitance of ionogels were increased with respect to the temperature. This was ascribed to the availability of more surface area, interconnected pores, and the thermally instigated ionic transport phenomena. The unique mechanical and thermal characteristics of hydrogels were accredited to the porous morphology, interconnected cross-linking network, electrostatic interactions, and hydrogen bonds.

The temperature tolerance of electrochemical devices is crucial to mitigate the fire explosions at extreme weathers. Even though more research focus has been given to the thermal safety of electrolytes and electrodes, a holistic approach should be further established by the industries to investigate the fire explosion issues in EVs and mobile electronics. In addition to the thermal safety features, the affordable cost, long-term durability, and high energy/power density are also significant to develop an EV market for a sustainable society. It is envisaged that the thermally stable SEs would play an influential role in the electrochemical research for the next few decades. Thermally stable and eco-friendly energy storage technologies would play a key role in the health and wealth of future generations.

Conflict of Interest

The authors declare no conflict of interest.

[1] X. Feng, M. Ouyang, X. Liu, L. Lu, Y. Xia, X. He, *Energy Storage Mater.* **2018**, *10*, 246.

[2] X. Feng, D. Ren, X. He, M. Ouyang, *Joule* **2020**, *4*, 743.

[3] X. Zhu, Z. Wang, Y. Wang, H. Wang, C. Wang, L. Tong, M. Yi, *Energy* **2019**, *169*, 868.

**ADVANCED
SCIENCE NEWS**

www.advancedsciencenews.com

**ADVANCED
ENERGY
MATERIALS**

www.advenergymat.de

[4] K. Liu, Y. Liu, D. Lin, A. Pei, Y. Cui, *Sci. Adv.* **2018**, *4*, eaas9820.

[5] J. Allen, *Energy Rep.* **2020**, *6*, 217.

[6] M. J. Loveridge, G. Remy, N. Kourra, R. Genieser, A. Barai, M. J. Lain, Y. Guo, M. Amor-Segan, M. A. Williams, T. Amietszajew, *Batteries* **2018**, *4*, 3.

[7] P. Simon, Y. Gogotsi, B. Dunn, *Science* **2014**, *343*, 1210.

[8] N. Zhao, W. Khokhar, Z. Bi, C. Shi, X. Guo, L.-Z. Fan, C.-W. Nan, *Joule* **2019**, *3*, 1190.

[9] C. Fang, J. Li, M. Zhang, Y. Zhang, F. Yang, J. Z. Lee, M.-H. Lee, J. Alvarado, M. A. Schroeder, Y. Yang, *Nature* **2019**, *572*, 511.

[10] Y.-Z. Zhang, Y. Wang, T. Cheng, L.-Q. Yao, X. Li, W.-Y. Lai, W. Huang, *Chem. Soc. Rev.* **2019**, *48*, 3229.

[11] L. Zhang, D. Shi, T. Liu, M. Jaroniec, J. Yu, *Mater. Today* **2019**, *25*, 35.

[12] H. Li, *Joule* **2019**, *3*, 911.

[13] F. Wu, J. Maier, Y. Yu, *Chem. Soc. Rev.* **2020**, *49*, 1569.

[14] J. Liu, Z. Bao, Y. Cui, E. J. Dufek, J. B. Goodenough, P. Khalifah, Q. Li, B. Y. Liaw, P. Liu, A. Manthiram, *Nat. Energy* **2019**, *4*, 180.

[15] B. Asbani, C. Douard, T. Brousse, J. Le Bideau, *Energy Storage Mater.* **2019**, *21*, 439.

[16] Q. Zhu, D. Zhao, M. Cheng, J. Zhou, K. A. Owusu, L. Mai, Y. Yu, *Adv. Energy Mater.* **2019**, *9*, 1901081.

[17] D. Chen, K. Jiang, T. Huang, G. Shen, *Adv. Mater.* **2020**, *32*, 1901806.

[18] J. Kindracki, P. Paszkiewicz, Ł. Mężyk, *Aerosp. Sci. Technol.* **2019**, *92*, 847.

[19] A. Noori, M. F. El-Kady, M. S. Rahmanifar, R. B. Kaner, M. F. Mousavi, *Chem. Soc. Rev.* **2019**, *48*, 1272.

[20] M. Liu, Z. Cheng, S. Ganapathy, C. Wang, L. A. Haverkate, M. Tułodziecki, S. Unnikrishnan, M. Wagemaker, *ACS Energy Lett.* **2019**, *4*, 2336.

[21] G. L. Xu, H. Sun, C. Luo, L. Estevez, M. Zhuang, H. Gao, R. Amine, H. Wang, X. Zhang, C. J. Sun, *Adv. Energy Mater.* **2019**, *9*, 1802235.

[22] J. Ming, Z. Cao, Y. Wu, W. Wahyudi, W. Wang, X. Guo, L. Cavallo, J.-Y. Hwang, A. Shamim, L.-J. Li, *ACS Energy Lett.* **2019**, *4*, 2613.

[23] M. Li, C. Wang, Z. Chen, K. Xu, J. Lu, *Chem. Rev.* **2020**, *120*, 6783.

[24] P. P. R. Harks, C. B. Robledo, T. W. Verhallen, P. H. Notten, F. M. Mulder, *Adv. Energy Mater.* **2017**, *7*, 1601635.

[25] K. Park, J. B. Goodenough, *Adv. Energy Mater.* **2017**, *7*, 1700732.

[26] Y. Yang, J. Xiong, S. Lai, R. Zhou, M. Zhao, H. Geng, Y. Zhang, Y. Fang, C. Li, J. Zhao, *ACS Appl. Mater. Interfaces* **2019**, *11*, 6118.

[27] W. Zhao, B. Zheng, H. Liu, F. Ren, J. Zhu, G. Zheng, S. Chen, R. Liu, X. Yang, Y. Yang, *Nano Energy* **2019**, *63*, 103815.

[28] J.-D. Xie, J. Patra, P. C. Rath, W.-J. Liu, C.-Y. Su, S.-W. Lee, C.-J. Tseng, Y. A. Gandomi, J.-K. Chang, *J. Power Sources* **2020**, *450*, 227657.

[29] M. Henriksen, K. Vågsæther, J. Lundberg, S. Forseth, D. Bjerketvedt, *J. Hazard. Mater.* **2019**, *371*, 1.

[30] X. Huang, J. Xue, M. Xiao, S. Wang, Y. Li, S. Zhang, Y. Meng, *Energy Storage Mater.* **2020**, *30*, 87.

[31] R. Chen, A. M. Nolan, J. Lu, J. Wang, X. Yu, Y. Mo, L. Chen, X. Huang, H. L, *Joule* **2020**, *4*, 812.

[32] W. Zhou, Z. Wang, Y. Pu, Y. Li, S. Xin, X. Li, J. Chen, J. B. Goodenough, *Adv. Mater.* **2019**, *31*, 1805574.

[33] A. Du, H. Zhang, Z. Zhang, J. Zhao, Z. Cui, Y. Zhao, S. Dong, L. Wang, X. Zhou, G. Cui, *Adv. Mater.* **2019**, *31*, 1805930.

[34] Z. Jiang, S. Wang, X. Chen, W. Yang, X. Yao, X. Hu, Q. Han, H. Wang, *Adv. Mater.* **2020**, *32*, 1906221.

[35] J.-Y. Liang, X.-X. Zeng, X.-D. Zhang, T.-T. Zuo, M. Yan, Y.-X. Yin, J.-L. Shi, X.-W. Wu, Y.-G. Guo, L.-J. Wan, *J. Am. Chem. Soc.* **2019**, *141*, 9165.

[36] D. Xu, J. Su, J. Jin, C. Sun, Y. Ruan, C. Chen, Z. Wen, *Adv. Energy Mater.* **2019**, *9*, 1900611.

[37] H. Huo, Y. Chen, J. Luo, X. Yang, X. Guo, X. Sun, *Adv. Energy Mater.* **2019**, *9*, 1804004.

[38] B. Zhang, R. Tan, L. Yang, J. Zheng, K. Zhang, S. Mo, Z. Lin, F. Pan, *Energy Storage Mater.* **2018**, *10*, 139.

[39] S. Li, S. Q. Zhang, L. Shen, Q. Liu, J. B. Ma, W. Lv, Y. B. He, Q. H. Yang, *Adv. Sci.* **2020**, *7*, 1903088.

[40] Y. Liao, T. Chen, X. Luo, Z. Fu, X. Li, W. Li, *J. Membr. Sci.* **2016**, *507*, 126.

[41] M. Faraji, H. M. Aydisheh, *Composites, Part B* **2019**, *168*, 432.

[42] R. Fang, H. Xu, B. Xu, X. Li, Y. Li, J. B. Goodenough, *Adv. Funct. Mater.* **2020**, 2001812.

[43] J. Sun, Y. Li, Q. Zhang, C. Hou, Q. Shi, H. Wang, *Chem. Eng. J.* **2019**, *375*, 121922.

[44] W. Huang, S. Zheng, X. Zhang, W. Zhou, W. Xiong, J. Chen, *Energy Storage Mater.* **2020**, *26*, 465.

[45] R. Kerr, D. Mazouzi, M. Eftekharnia, B. Lestriez, N. Dupré, M. Forsyth, D. Guyomard, P. C. Howlett, *ACS Energy Lett.* **2017**, *2*, 1804.

[46] C.-S. Lim, K. Teoh, H. Ng, C.-W. Liew, S. Ramesh, *Adv. Mater. Lett.* **2017**, *8*, 465.

[47] X. Judez, G. G. Eshetu, I. Gracia, P. López-Aranguren, J. A. González-Marcos, M. Armand, L. M. Rodriguez-Martinez, H. Zhang, C. Li, *ChemElectroChem* **2019**, *6*, 326.

[48] Y. Liu, B. Xu, W. Zhang, L. Li, Y. Lin, C. Nan, *Small* **2020**, *16*, 1902813.

[49] X. Chen, B. Put, A. Sagara, K. Gandrud, M. Murata, J. A. Steele, H. Yabe, T. Hantschel, M. Roeffaers, M. Tomiyama, *Sci. Adv.* **2020**, *6*, eaav3400.

[50] W. Xu, X. Pei, C. S. Diercks, H. Lyu, Z. Ji, O. M. Yaghi, *J. Am. Chem. Soc.* **2019**, *141*, 17522.

[51] R. Li, D. Wu, L. Yu, Y. Mei, L. Wang, H. Li, X. Hu, *Adv. Eng. Mater.* **2019**, *21*, 1900055.

[52] S. S. Chi, Y. Liu, W. L. Song, L. Z. Fan, Q. Zhang, *Adv. Funct. Mater.* **2017**, *27*, 1700348.

[53] Q. Zhao, S. Stalin, C.-Z. Zhao, L. A. Archer, *Nat. Rev. Mater.* **2020**, *5*, 229.

[54] Z. Gao, H. Sun, L. Fu, F. Ye, Y. Zhang, W. Luo, Y. Huang, *Adv. Mater.* **2018**, *30*, 1705702.

[55] J. Li, C. Ma, M. Chi, C. Liang, N. J. Dudney, *Adv. Energy Mater.* **2015**, *5*, 1401408.

[56] M. B. Dixit, W. Zaman, N. Hortance, S. Vujic, B. Harkey, F. Shen, W.-Y. Tsai, V. De Andrade, X. C. Chen, N. Balke, *Joule* **2020**, *4*, 207.

[57] T. Famprikis, P. Canepa, J. A. Dawson, M. S. Islam, C. Masquelier, *Nat. Mater.* **2019**, *18*, 1278.

[58] S. Zhang, Z. Li, Y. Guo, L. Cai, P. Manikandan, K. Zhao, Y. Li, V. G. Pol, *Chem. Eng. J.* **2020**, *400*, 125996.

[59] Y. Huang, L. Zhao, L. Li, M. Xie, F. Wu, R. Chen, *Adv. Mater.* **2019**, *31*, 1808393.

[60] G. G. Eshetu, G. A. Elia, M. Armand, M. Forsyth, S. Komaba, T. Rojo, S. Passerini, *Adv. Energy Mater.* **2020**, *10*, 2000093.

[61] C. Bommier, X. Ji, *Small* **2018**, *14*, 1703576.

[62] G. Åvall, J. Mindemark, D. Brandell, P. Johansson, *Adv. Energy Mater.* **2018**, *8*, 1703036.

[63] A. Banerjee, X. Wang, C. Fang, E. A. Wu, Y. S. Meng, *Chem. Rev.* **2020**, *120*, 6878.

[64] G. Yang, Y. Song, Q. Wang, L. Zhang, L. Deng, *Mater. Des.* **2020**, *190*, 108563.

[65] X. Liu, X. Li, H. Li, H. B. Wu, *Chem. - Eur. J.* **2018**, *24*, 18293.

[66] L. Fan, S. Wei, S. Li, Q. Li, Y. Lu, *Adv. Energy Mater.* **2018**, *8*, 1702657.

[67] A. Manthiram, X. Yu, S. Wang, *Nat. Rev. Mater.* **2017**, *2*, 16103.

[68] J. C. Bachman, S. Muy, A. Grimaud, H.-H. Chang, N. Pour, S. F. Lux, O. Paschos, F. Maglia, S. Lupart, P. Lamp, *Chem. Rev.* **2016**, *116*, 140.

[69] G. Ceder, S. P. Ong, Y. Wang, *MRS Bull.* **2018**, *43*, 746.

[70] R. Chen, W. Qu, X. Guo, L. Li, F. Wu, *Mater. Horiz.* **2016**, *3*, 487.

[71] X. Ke, Y. Wang, G. Ren, C. Yuan, *Energy Storage Mater.* **2020**, *26*, 313.

[72] Z. Wu, Z. Xie, A. Yoshida, Z. Wang, X. Hao, A. Abudula, G. Guan, *Renewable Sustainable Energy Rev.* **2019**, *109*, 367.

[73] F. Zheng, M. Kotobuki, S. Song, M. O. Lai, L. Lu, *J. Power Sources* **2018**, *389*, 198.

[74] J. Wolfenstine, J. L. Allen, J. Sakamoto, D. J. Siegel, H. Choe, *Ionics* **2018**, *24*, 1271.

[75] E. Umeshbabu, B. Zheng, Y. Yang, *Electrochem. Energy Rev.* **2019**, *2*, 199.

[76] C.-Z. Zhao, B.-C. Zhao, C. Yan, X.-Q. Zhang, J.-Q. Huang, Y. Mo, X. Xu, H. Li, Q. Zhang, *Energy Storage Mater.* **2020**, *24*, 75.

[77] X. Cao, X. Ren, L. Zou, M. H. Engelhard, W. Huang, H. Wang, B. E. Matthews, H. Lee, C. Niu, B. W. Arey, *Nat. Energy* **2019**, *4*, 796.

[78] D. Zhou, D. Shanmukaraj, A. Tkacheva, M. Armand, G. Wang, *Chem* **2019**, *5*, 2326.

[79] Q. Zhao, X. Liu, S. Stalin, K. Khan, L. A. Archer, *Nat. Energy* **2019**, *4*, 365.

[80] J. Li, J. Qiao, K. Lian, *Energy Storage Mater.* **2020**, *24*, 6.

[81] E. Glynos, C. Pantazidis, G. Sakellariou, *ACS Omega* **2020**, *5*, 2531.

[82] I. Osada, H. de Vries, B. Scrosati, S. Passerini, *Angew. Chem., Int. Ed.* **2016**, *55*, 500.

[83] Z. Xue, D. He, X. Xie, *J. Mater. Chem. A* **2015**, *3*, 19218.

[84] A. Arya, A. Sharma, *Ionics* **2017**, *23*, 497.

[85] L. Long, S. Wang, M. Xiao, Y. Meng, *J. Mater. Chem. A* **2016**, *4*, 10038.

[86] L. Qiao, X. Judez, T. Rojo, M. Armand, H. Zhang, *J. Electrochem. Soc.* **2020**, *167*, 070534.

[87] H. Zhang, C. Li, M. Piszcz, E. Coya, T. Rojo, L. M. Rodriguez-Martinez, M. Armand, Z. Zhou, *Chem. Soc. Rev.* **2017**, *46*, 797.

[88] S. Alipoori, S. Mazinani, S. H. Aboutalebi, F. Sharif, *J. Energy Storage* **2020**, *27*, 101072.

[89] X. Cheng, J. Pan, Y. Zhao, M. Liao, H. Peng, *Adv. Energy Mater.* **2018**, *8*, 1702184.

[90] Q. Zhang, K. Liu, F. Ding, X. Liu, *Nano Res.* **2017**, *10*, 4139.

[91] Q. Wang, H. Zhang, Z. Cui, Q. Zhou, X. Shangguan, S. Tian, X. Zhou, G. Cui, *Energy Storage Mater.* **2019**, *23*, 466.

[92] L. Duchêne, A. Remhof, H. Hagemann, C. Battaglia, *Energy Storage Mater.* **2020**, *25*, 782.

[93] A. Løken, S. Ricote, S. Wachowski, *Crystals* **2018**, *8*, 365.

[94] V. Lacivita, Y. Wang, S.-H. Bo, G. Ceder, *J. Mater. Chem. A* **2019**, *7*, 8144.

[95] R. Chen, D. Bresser, M. Saraf, P. Gerlach, A. Balducci, S. Kunz, D. Schröder, S. Passerini, J. Che, *ChemSusChem* **2020**, *13*, 2205.

[96] M. Hou, F. Liang, K. Chen, Y. Dai, D. Xue, *Nanotechnology* **2020**, *31*, 132003.

[97] A. Melemed, A. Khurram, B. M. Gallant, *Batteries Supercaps* **2020**, *3*, 570.

[98] E. Logan, J. Dahn, *Trends Chem.* **2020**, *2*, 354.

[99] F. Wan, J. Zhu, S. Huang, Z. Niu, *Batteries Supercaps* **2020**, *3*, 323.

[100] E. Jonsson, *Energy Storage Mater.* **2020**, *25*, 827.

[101] M. Rashad, M. Asif, Z. Ali, *Coord. Chem. Rev.* **2020**, *415*, 213312.

[102] Z. Ma, D. R. MacFarlane, M. Kar, *Batteries Supercaps* **2019**, *2*, 115.

[103] S. Zhang, K. Ueno, K. Dokko, M. Watanabe, *Adv. Energy Mater.* **2015**, *5*, 1500117.

[104] J. Lau, R. H. DeBlock, D. M. Butts, D. S. Ashby, C. S. Choi, B. S. Dunn, *Adv. Energy Mater.* **2018**, *8*, 1800933.

[105] Q. Zhang, D. Cao, Y. Ma, A. Natan, P. Aurora, H. Zhu, *Adv. Mater.* **2019**, *31*, 1901131.

[106] N. Chen, H. Zhang, L. Li, R. Chen, S. Guo, *Adv. Energy Mater.* **2018**, *8*, 1702675.

[107] Y. Shi, D. Tan, M. Li, Z. Chen, *Nanotechnology* **2019**, *30*, 302002.

[108] C. Choi, S. Kim, R. Kim, Y. Choi, S. Kim, *Renewable Sustainable Energy Rev.* **2017**, *69*, 263.

[109] B. Singh, S. Ghosh, S. Aich, B. Roy, *J. Power Sources* **2017**, *339*, 103.

[110] Z. Wang, H. Li, Z. Tang, Z. Liu, Z. Ruan, L. Ma, Q. Yang, D. Wang, C. Zhi, *Adv. Funct. Mater.* **2018**, *28*, 1804560.

[111] Y. Yamada, J. Wang, S. Ko, E. Watanabe, A. Yamada, *Nat. Energy* **2019**, *4*, 269.

[112] S. Gunduz, D. J. Deka, U. S. Ozkan, *J. Catal.* **2020**, *387*, 207.

[113] X. Lin, M. Salari, L. M. R. Arava, P. M. Ajayan, M. W. Grinstaff, *Chem. Soc. Rev.* **2016**, *45*, 5848.

[114] X. Lin, G. Zhou, J. Liu, J. Yu, M. B. Effat, J. Wu, F. Ciucci, *Adv. Energy Mater.* **2020**, *10*, 2001235.

[115] X. Liu, D. Ren, H. Hsu, X. Feng, G.-L. Xu, M. Zhuang, H. Gao, L. Lu, X. Han, Z. Chu, *Joule* **2018**, *2*, 2047.

[116] M. Armand, J.-M. Tarascon, *Nature* **2008**, *451*, 652.

[117] D. P. Finegan, J. Darst, W. Walker, Q. Li, C. Yang, R. Jervis, T. M. Heenan, J. Hack, J. C. Thomas, A. Rack, *J. Power Sources* **2019**, *417*, 29.

[118] W. Q. Walker, J. J. Darst, D. P. Finegan, G. A. Bayles, K. L. Johnson, E. C. Darcy, S. L. Rickman, *J. Power Sources* **2019**, *415*, 207.

[119] X. Feng, S. Zheng, X. He, L. Wang, Y. Wang, D. Ren, M. Ouyang, *Front. Energy Res.* **2018**, *6*, 126.

[120] X. Feng, M. Fang, X. He, M. Ouyang, L. Lu, H. Wang, M. Zhang, *J. Power Sources* **2014**, *255*, 294.

[121] L. P. Hou, X. Q. Zhang, B. Q. Li, Q. Zhang, *Angew. Chem.* **2020**, *132*, 15221.

[122] Z. Gadjourova, Y. G. Andreev, D. P. Tunstall, P. G. Bruce, *Nature* **2001**, *412*, 520.

[123] W. A. Henderson, S. Passerini, *Electrochem. Commun.* **2003**, *5*, 575.

[124] S. Xue, Y. Liu, Y. Li, D. Teeters, D. W. Crunkleton, S. Wang, *Electrochim. Acta* **2017**, *235*, 122.

[125] W. Liu, S. W. Lee, D. Lin, F. Shi, S. Wang, A. D. Sendek, Y. Cui, *Nat. Energy* **2017**, *2*, 17035.

[126] W. Zhou, S. Wang, Y. Li, S. Xin, A. Manthiram, J. B. Goodenough, *J. Am. Chem. Soc.* **2016**, *138*, 9385.

[127] K. J. Harry, X. Liao, D. Y. Parkinson, A. M. Minor, N. P. Balsara, *J. Electrochem. Soc.* **2015**, *162*, A2699.

[128] R. Khurana, J. L. Schaefer, L. A. Archer, G. W. Coates, *J. Am. Chem. Soc.* **2014**, *136*, 7395.

[129] G. Gregori, R. Merkle, J. Maier, *Prog. Mater. Sci.* **2017**, *89*, 252.

[130] J. A. Dawson, P. Canepa, T. Famprikis, C. Masquelier, M. S. Islam, *J. Am. Chem. Soc.* **2018**, *140*, 362.

[131] Y. Inaguma, C. Liquan, M. Itoh, T. Nakamura, T. Uchida, H. Ikuta, M. Wakihara, *Solid State Commun.* **1993**, *86*, 689.

[132] C.-C. Chen, L. Fu, J. Maier, *Nature* **2016**, *536*, 159.

[133] C.-C. Chen, J. Maier, *Nat. Energy* **2018**, *3*, 102.

[134] J. Haruyama, K. Sodeyama, L. Han, K. Takada, Y. Tateyama, *Chem. Mater.* **2014**, *26*, 4248.

[135] L. Yue, J. Ma, J. Zhang, J. Zhao, S. Dong, Z. Liu, G. Cui, L. Chen, *Energy Storage Mater.* **2016**, *5*, 139.

[136] X. Ma, X. Zuo, J. Wu, X. Deng, X. Xiao, J. Liu, J. Nan, *J. Mater. Chem. A* **2018**, *6*, 1496.

[137] C. Wang, Y. Yang, X. Liu, H. Zhong, H. Xu, Z. Xu, H. Shao, F. Ding, *ACS Appl. Mater. Interfaces* **2017**, *9*, 13694.

[138] F. Chen, D. Yang, W. Zha, B. Zhu, Y. Zhang, J. Li, Y. Gu, Q. Shen, L. Zhang, D. R. Sadoway, *Electrochim. Acta* **2017**, *258*, 1106.

[139] J. Zhang, N. Zhao, M. Zhang, Y. Li, P. K. Chu, X. Guo, Z. Di, X. Wang, H. Li, *Nano Energy* **2016**, *28*, 447.

[140] W. Hou, X. Guo, X. Shen, K. Amine, H. Yu, J. Lu, *Nano Energy* **2018**, *52*, 279.

[141] Z. Li, H.-M. Huang, J.-K. Zhu, J.-F. Wu, H. Yang, L. Wei, X. Guo, *ACS Appl. Mater. Interfaces* **2018**, *11*, 784.

[142] M. Uitz, V. Epp, P. Bottke, M. Wilkening, *J. Electroceram.* **2017**, *38*, 142.

**ADVANCED
SCIENCE NEWS**

www.advancedsciencenews.com

**ADVANCED
ENERGY
MATERIALS**

www.advenergymat.de

[143] Q. Wang, P. Ping, X. Zhao, G. Chu, J. Sun, C. Chen, *J. Power Sources* **2012**, *208*, 210.

[144] X. Feng, J. Sun, M. Ouyang, X. He, L. Lu, X. Han, M. Fang, H. Peng, *J. Power Sources* **2014**, *272*, 457.

[145] P. T. Coman, E. C. Darcy, C. T. Veje, R. E. White, *Appl. Energy* **2017**, *203*, 189.

[146] P. Ping, Q. Wang, Y. Chung, J. Wen, *Appl. Energy* **2017**, *205*, 1327.

[147] R. Zhao, J. Liu, J. Gu, *Appl. Energy* **2016**, *173*, 29.

[148] X. Feng, C. Weng, M. Ouyang, J. Sun, *Appl. Energy* **2016**, *161*, 168.

[149] P. T. Coman, S. Mátéfi-Tempfli, C. T. Veje, R. E. White, *J. Electrochem. Soc.* **2017**, *164*, A1858.

[150] D. Ren, X. Feng, L. Lu, M. Ouyang, S. Zheng, J. Li, X. He, *J. Power Sources* **2017**, *364*, 328.

[151] P. Huang, P. Ping, K. Li, H. Chen, Q. Wang, J. Wen, J. Sun, *Appl. Energy* **2016**, *183*, 659.

[152] X. Feng, X. He, M. Ouyang, L. Lu, P. Wu, C. Kulp, S. Prasser, *Appl. Energy* **2015**, *154*, 74.

[153] B. Liu, S. Yin, J. Xu, *Appl. Energy* **2016**, *183*, 278.

[154] D. Ren, X. Liu, X. Feng, L. Lu, M. Ouyang, J. Li, X. He, *Appl. Energy* **2018**, *228*, 633.

[155] L. Liu, J. Park, X. Lin, A. M. Sastry, W. Lu, *J. Power Sources* **2014**, *268*, 482.

[156] L. H. Saw, H. M. Poon, W. T. Chong, C.-T. Wang, M. C. Yew, M. K. Yew, T. C. Ng, *Energy Procedia* **2019**, *158*, 2750.

[157] P. Guillemet, Y. Scudeller, T. Brousse, *J. Power Sources* **2006**, *157*, 630.

[158] A. d'Entremont, L. Pilon, *J. Power Sources* **2014**, *246*, 887.

[159] H. Gualous, H. Louahlia, R. Gallay, *IEEE Trans. Power Electron.* **2011**, *26*, 3402.

[160] H. Gualous, H. Louahlia-Gualous, R. Gallay, A. Miraoui, *IEEE Trans. Ind. Appl.* **2009**, *45*, 1035.

[161] A. J. Blake, R. R. Kohlmeyer, J. O. Hardin, E. A. Carmona, B. Maruyama, J. D. Berrigan, H. Huang, M. F. Durstock, *Adv. Energy Mater.* **2017**, *7*, 1602920.

[162] X. Liu, O. O. Taiwo, C. Yin, M. Ouyang, R. Chowdhury, B. Wang, H. Wang, B. Wu, N. P. Brandon, Q. Wang, *Adv. Sci.* **2019**, *6*, 1801337.

[163] R. R. Kohlmeyer, G. A. Horrocks, A. J. Blake, Z. Yu, B. Maruyama, H. Huang, M. F. Durstock, *Nano Energy* **2019**, *64*, 103927.

[164] C. Lu, X. Chen, *Nano Lett.* **2020**, *20*, 1907.

[165] W. Tang, S. Tang, C. Zhang, Q. Ma, Q. Xiang, Y. W. Yang, J. Luo, *Adv. Energy Mater.* **2018**, *8*, 1800866.

[166] Q. Zhou, S. Dong, Z. Lv, G. Xu, L. Huang, Q. Wang, Z. Cui, G. Cui, *Adv. Energy Mater.* **2020**, *10*, 1903441.

[167] X. Jin, G. Sun, G. Zhang, H. Yang, Y. Xiao, J. Gao, Z. Zhang, L. Qu, *Nano Res.* **2019**, *12*, 1199.

[168] J. Wei, G. Wei, G. Shang, J. Zhou, C. Wu, Q. Wang, *Adv. Mater.* **2019**, *31*, 1900248.

[169] J. R. Copeland, X.-R. Shi, D. S. Sholl, C. Sievers, *Langmuir* **2013**, *29*, 581.

[170] J.-J. Woo, Z. Zhang, N. L. D. Rago, W. Lu, K. Amine, *J. Mater. Chem. A* **2013**, *1*, 8538.

[171] X. Huang, *J. Solid State Electrochem.* **2011**, *15*, 649.

[172] M. D. Tikekar, S. Choudhury, Z. Tu, L. A. Archer, *Nat. Energy* **2016**, *1*, 16114.

[173] J. W. Suk, R. D. Piner, J. An, R. S. Ruoff, *Thin Solid Films* **2013**, *527*, 205.

[174] S.-S. Chi, Y. Liu, N. Zhao, X. Guo, C.-W. Nan, L.-Z. Fan, *Energy Storage Mater.* **2019**, *17*, 309.

[175] R. Zhang, X. Chen, X. Shen, X.-Q. Zhang, X.-R. Chen, X.-B. Cheng, C. Yan, C.-Z. Zhao, Q. Zhang, *Joule* **2018**, *2*, 764.

[176] Y. Liu, D. Lin, Y. Jin, K. Liu, X. Tao, Q. Zhang, X. Zhang, Y. Cui, *Sci. Adv.* **2017**, *3*, eaao0713.

[177] A. Sharafi, E. Kazyak, A. L. Davis, S. Yu, T. Thompson, D. J. Siegel, N. P. Dasgupta, J. Sakamoto, *Chem. Mater.* **2017**, *29*, 7961.

[178] L. Nègre, B. Daffos, V. Turq, P.-L. Taberna, P. Simon, *Electrochim. Acta* **2016**, *206*, 490.

[179] H. H. Rana, J. H. Park, E. Ducrot, H. Park, M. Kota, T. H. Han, J. Y. Lee, J. Kim, J.-H. Kim, P. Howlett, *Energy Storage Mater.* **2019**, *19*, 197.

[180] D. W. Kim, S. M. Jung, H. Y. Jung, *J. Mater. Chem. A* **2020**, *8*, 532.

[181] B. Shen, R. Guo, J. Lang, L. Liu, L. Liu, X. Yan, *J. Mater. Chem. A* **2016**, *4*, 8316.

[182] R. S. Borges, A. L. M. Reddy, M.-T. F. Rodrigues, H. Gullapalli, K. Balakrishnan, G. G. Silva, P. M. Ajayan, *Sci. Rep.* **2013**, *3*, 2572.

[183] G. Pandey, S. Hashmi, *J. Mater. Chem. A* **2013**, *1*, 3372.

[184] W. Lu, K. Henry, C. Turchi, J. Pellegrino, *J. Electrochem. Soc.* **2008**, *155*, A361.

[185] P. Pal, A. Ghosh, *J. Power Sources* **2018**, *406*, 128.

[186] T. Y. Kim, H. W. Lee, M. Stoller, D. R. Dreyer, C. W. Bielawski, R. S. Ruoff, K. S. Suh, *ACS Nano* **2011**, *5*, 436.

[187] T. Mao, S. Wang, X. Wang, F. Liu, J. Li, H. Chen, D. Wang, G. Liu, J. Xu, Z. Wang, *ACS Appl. Mater. Interfaces* **2019**, *11*, 17742.

[188] S. Wang, C. Zhao, W. Ma, G. Zhang, Z. Liu, J. Ni, M. Li, N. Zhang, H. Na, *J. Membr. Sci.* **2012**, *411*, 54.

[189] X. Tian, S. Wang, J. Li, F. Liu, X. Wang, H. Chen, H. Ni, Z. Wang, *Int. J. Hydrogen Energy* **2017**, *42*, 21913.

[190] F. Liu, S. Wang, J. Li, X. Tian, X. Wang, H. Chen, Z. Wang, *J. Membr. Sci.* **2017**, *541*, 492.

[191] Q. Rong, W. Lei, J. Huang, M. Liu, *Adv. Energy Mater.* **2018**, *8*, 1801967.

[192] Z. Wang, Q. Pan, *Adv. Funct. Mater.* **2017**, *27*, 1700690.

[193] Y. Huang, M. Zhong, F. Shi, X. Liu, Z. Tang, Y. Wang, Y. Huang, H. Hou, X. Xie, C. Zhi, *Angew. Chem., Int. Ed.* **2017**, *56*, 9141.

[194] H. Li, T. Lv, N. Li, Y. Yao, K. Liu, T. Chen, *Nanoscale* **2017**, *9*, 18474.

[195] X. Liu, O. O. Taiwo, C. Yin, M. Ouyang, R. Chowdhury, B. Wang, H. Wang, B. Wu, N. P. Brandon, Q. Wang, *Adv. Sci.* **2019**, *6*, 1970029.

[196] C. Chen, Y. Zhang, Y. Li, J. Dai, J. Song, Y. Yao, Y. Gong, I. Kierzewski, J. Xie, L. Hu, *Energy Environ. Sci.* **2017**, *10*, 538.

[197] S.-J. Tan, X.-X. Zeng, Q. Ma, X.-W. Wu, Y.-G. Guo, *Electrochem. Energy Rev.* **2018**, *1*, 113.

[198] L. Wang, Y. Ye, N. Chen, Y. Huang, L. Li, F. Wu, R. Chen, *Adv. Funct. Mater.* **2018**, *28*, 1800919.

[199] Y. Ma, L. Li, G. Gao, X. Yang, Y. You, *Electrochim. Acta* **2016**, *187*, 535.

[200] J.-W. Lee, S. Yu, S. M. Hong, C. M. Koo, *J. Mater. Chem. C* **2013**, *1*, 3784.

[201] C. Lu, X. Chen, *Adv. Mater. Technol.* **2019**, *4*, 1900564.

[202] Z. Wang, F. Tao, Q. Pan, *J. Mater. Chem. A* **2016**, *4*, 17732.

[203] C. Lu, X. Chen, *J. Power Sources* **2020**, *448*, 227587.

[204] P. Podsiadlo, A. K. Kaushik, E. M. Arruda, A. M. Waas, B. S. Shim, J. Xu, H. Nandivada, B. G. Pumplin, J. Lahann, A. Ramamoorthy, *Science* **2007**, *318*, 80.

[205] G. Crabtree, *Science* **2019**, *366*, 422.

[206] X. Zeng, M. Li, D. Abd El-Hady, W. Alshitari, A. S. Al-Bogami, J. Lu, K. Amine, *Adv. Energy Mater.* **2019**, *9*, 1900161.

[207] L. Zhang, P. Zhao, M. Xu, X. Wang, *Appl. Energy* **2020**, *261*, 114440.

[208] Z. P. Cano, D. Banham, S. Ye, A. Hintennach, J. Lu, M. Fowler, Z. Chen, *Nat. Energy* **2018**, *3*, 279.

[209] M. Muratori, *Nat. Energy* **2018**, *3*, 193.

[210] Y. Wang, Z. Chang, M. Qian, T. Lin, F. Huang, *Chem. Eng. J.* **2019**, *375*, 122054.

[211] W. Zuo, R. Li, C. Zhou, Y. Li, J. Xia, J. Liu, *Adv. Sci.* **2017**, *4*, 1600539.

[212] F. Markoulidis, J. Bates, C. Lekakou, R. Slade, G. M. Laudone, *Carbon* **2020**, *164*, 422.

[213] Y.-G. Lee, S. Fujiki, C. Jung, N. Suzuki, N. Yashiro, R. Omoda, D.-S. Ko, T. Shiratsuchi, T. Sugimoto, S. Ryu, *Nat. Energy* **2020**, *5*, 299.

ADVANCED
SCIENCE NEWS

www.advancedsciencenews.com

ADVANCED
ENERGY
MATERIALS

www.advenergymat.de

Vignesh Kumaravel is working at IT Sligo as a senior research fellow in the renewable engine project. He obtained his Ph.D. from Madurai Kamaraj University, India, in 2013. His research interests include the synthesis and utilization of various nanoparticles for hydrogen production, CO_2 conversion, self-cleaning, food packaging polymers, high-temperature stable batteries/super-capacitors, and antimicrobial applications.

John Bartlett is the head of research at the Institute of Technology, Sligo, responsible for developing a research culture based on scholarship, multidisciplinarity, and collaboration, including the development of policy, strategy, administrative systems, quality assurance, budgets, capital infrastructure, and project initiatives with internal and external stakeholders/agencies. His research interests include ecotoxicology, environmental impact assessment, waste management technology, renewable energy technology, public access to environmental information, decision-making and justice, and public services innovation.

Suresh C. Pillai obtained his Ph.D. from Trinity College Dublin and completed his postdoctoral research at California Institute of Technology (Caltech, USA). He joined IT Sligo in 2013 as a senior lecturer and currently leads the nanotechnology and bioengineering research group. He completed an executive MBA from Dublin City University. His research interests include the synthesis of nanomaterials for energy and environmental applications.